

UNIVERSITY OF CALGARY  
FACULTY OF GRADUATE STUDIES

The undersigned certify that they have read, and recommend to the Faculty of Graduate Studies for acceptance, a Thesis entitled "Reverse time migration for converted waves and anisotropic media" submitted by Benjamin Douglas Wards in partial fulfillment of the requirements for the degree of DOCTOR OF PHILOSOPHY.

---

Supervisor, Dr. Gary Margrave  
Dept. of

---

Co-supervisor, Dr. Michael Lamoureux  
Dept. of

---

Dr.  
Dept. of

---

Date

UNIVERSITY OF CALGARY

Reverse time migration for converted waves and anisotropic media

by

Benjamin Douglas Wards

A THESIS  
SUBMITTED TO THE FACULTY OF GRADUATE STUDIES  
IN PARTIAL FULFILLMENT OF THE REQUIREMENTS FOR THE  
DEGREE OF DOCTOR OF PHILOSOPHY

DEPARTMENT OF DEPARTMENT Of GEOSCIENCE

CALGARY, ALBERTA  
July, 2017

© Benjamin Douglas Wards 2017

# Abstract

Here we go.

# Table of Contents

|  |      |
|--|------|
| <b>Abstract</b>  | ii   |
| <b>Table of Contents</b>                                     | iii  |
| <b>List of Tables</b>  | vi   |
| <b>List of Figures</b>                                       | vii  |
| <b>List of Symbols and Abbreviations</b>                     | xi   |
| <b>Definitions</b>   | xiii |
| <b>1 Introduction</b>  | 2    |
| 1.1 Mathematical description of waves in the earth . . . . . | 3    |
| 1.2 Numerical solution of the wave equation . . . . .        | 4    |
| 1.3 Improving migration algorithms . . . . .                 | 5    |
| 1.4 Prestack-depth migration . . . . .                       | 8    |
| 1.5 Processing seismic data prior to migration . . . . .     | 8    |
| 1.6 Time migration and depth migration . . . . .             | 9    |
| 1.7 Poststack and prestack migration . . . . .               | 9    |
| 1.8 Velocity building . . . . .                              | 10   |
| 1.9 Kirchhoff and Gaussian beam migrations . . . . .         | 10   |
| 1.10 Two-way versus one-way wave equation . . . . .          | 11   |
| 1.11 Depth-continuation migrations . . . . .                 | 11   |
| 1.12 Reverse-time migration . . . . .                        | 13   |
| 1.13 Significant contributions . . . . .                     | 14   |
| 1.14 Chapter summaries . . . . .                             | 14   |
| <b>2 The elastic wave equation</b>                           | 16   |
| 2.1 Introduction . . . . .                                   | 16   |
| 2.2 The elastic wave equation . . . . .                      | 16   |

|          |  |           |
|----------|--|-----------|
| 2.3      | Anisotropy . . . . .   | 18        |
| 2.4      | The Kelvin-Christoffel equation . . . . .  | 20        |
| 2.5      | The earth as a multi-layered fluid . . . . .   | 21        |
| 2.6      | Pseudo-acoustic wavefield propagation . . . . .  | 22        |
| <b>3</b> | <b>Wavefield propagation in acoustic media</b>   | <b>23</b> |
| 3.1      | Introduction . . . . .   | 23        |
| 3.2      | Finite-difference methods . . . . .  | 25        |
| 3.3      | Two-way time stepping by a phase shift . . . . .   | 27        |
| 3.4      | Initial conditions, boundary conditions, source initiation, and back propagation . . . . . | 28        |
| 3.5      | Aliasing and stability analysis . . . . .  | 30        |
| 3.6      | Pseudospectral methods . . . . .   | 30        |
| 3.7      | PSTS for variable velocity . . . . .   | 33        |
| 3.8      | Split-step time stepping . . . . .   | 37        |
| 3.9      | Huygens's interpretation of the phase shift . . . . .                                      | 38        |
| 3.10     | PSTS with the derivative of the wavefield . . . . .  | 38        |
| 3.11     | Multi-stepping in the wavenumber domain . . . . .  | 40        |
| 3.12     | One-way in time wavefield propagation . . . . .  | 41        |
| 3.13     | Numerical examples . . . . .   | 42        |
| 3.14     | Sampling issues . . . . .  | 44        |
| 3.15     | Forward modeling example . . . . .   | 45        |
| 3.16     | Conclusion . . . . .   | 46        |
| <b>4</b> | <b>Wavefield propagation in anisotropic media</b>  | <b>54</b> |
| 4.1      | Introduction . . . . .   | 55        |
| 4.2      | Pseudo-acoustic wavefield propagation . . . . .  | 56        |
| 4.3      | Dispersion relations for P and S waves in anisotropic media . . . . .                      | 57        |
| 4.4      | Wavenumber representation of dispersion relations . . . . .                                | 58        |
| 4.5      | Wavefield propagation in anisotropic heterogeneous media . . . . .                         | 59        |
| 4.6      | Wavefield propagation in orthorhombic media . . . . .                                      | 60        |
| 4.7      | Numerical examples . . . . .   | 61        |
| 4.8      | Conclusion . . . . .   | 64        |
| <b>5</b> | <b>Reverse time migration: imaging conditions, aliasing, and artifacts</b>                 | <b>65</b> |
| 5.1      | Introduction . . . . .   | 65        |
| 5.2      | Born forward modelling and its inverse . . . . .   | 66        |
| 5.3      | Imaging conditions for RTM . . . . .   | 67        |
| 5.3.1    | Laplacian filtering . . . . .  | 70        |
| 5.3.2    | Directional wavefield decomposition . . . . .  | 70        |

|                     |  |            |
|---------------------|--|------------|
| 5.4                 | Aliasing in the imaging condition . . . . .                      | 70         |
| 5.4.1               | Migration aliasing . . . . .                                     | 77         |
| 5.5                 | Discussion . . . . .   | 78         |
| 5.6                 | Conclusions . . . . .  | 78         |
| <b>6</b>            | <b>Converted waves</b>   | <b>79</b>  |
| 6.1                 | Elastic reverse-time migration . . . . .                         | 79         |
| 6.2                 | Shear wave splitting . . . . .                                   | 80         |
| 6.3                 | Geophone orientation . . . . .                                   | 80         |
| 6.4                 | Wavefield separation at the surface . . . . .                    | 80         |
| 6.5                 | Conversion point determination . . . . .                         | 80         |
| 6.6                 | Reciprocity for converted waves . . . . .                        | 80         |
| 6.7                 | Converted wave imaging . . . . .                                 | 83         |
| <b>7</b>            | <b>Migration results</b>   | <b>84</b>  |
| 7.1                 | Migration of the Marmousi data set . . . . .                     | 84         |
| <b>Bibliography</b> |  | <b>98</b>  |
| <b>A</b>            | <b>Mathematics and background theory</b>                         | <b>104</b> |
| A.1                 | Fourier theory . . . . .   | 104        |
| A.2                 | The Gabor transform and adaptive partitions of unity . . . . .   | 104        |
| A.3                 | Gabor analysis . . . . .   | 106        |
| A.4                 | Thomsen's parameters . . . . .                                   | 106        |
| A.5                 | An evolutionary solution to the acoustic wave equation . . . . . | 107        |

# List of Tables

|     |   |    |
|-----|---|----|
| 3.1 | Relative computation time and time-step size used in algorithms to generate Figure 3.6 and Figure 3.9 . . . . . | 43 |
| 7.1 | Computation time, time step size, and grid-sizes used to calculate the figures in this chapter. . . . .         | 91 |

# List of Figures

|     |  |    |
|-----|--|----|
| 3.1 | The center trace of a wavefield propagated in a constant-velocity model in 2-D. A minimum phase wavelet was injected at the center point of the model. (a) Using finite differences with $\delta t = 0.0001$ . (b) Using the phase-shift time-stepping equation with $\delta t = 0.001$ . The low-order FD method took 10 times as long to compute. . . . .  | 29 |
| 3.2 | The center trace of the response to zero phase wavelet injected at the center of a constant velocity model with two spatial dimensions. The wave equation is solved for various values of the Courant number $r$ . When $r > \sqrt{0.5}$ aliasing occurs in the model. From top to bottom $r = 0.68 \leq 0.71$ , $r = 1.00 \not\leq 0.71$ , and $r = 1.5 \not\leq 0.71$ , respectively. The grid-spacing was taken to be a constant, $10m$ , and the time step was varied for the constant velocity, $v = 2500m/s$ . The maximum frequency in the wavelet was $35Hz$ . . . . . | 31 |
| 3.3 | A set of windowing functions used to propagate the Marmousi dataset. (a),(b),(c),(d) corresponding to the velocities $1556$ , $2902$ , $4247$ , and $5593m/s$ , respectively. . . . .  | 47 |
| 3.4 | The Percent velocity error when using different kinds of interpolation schemes between constant velocity operators. The interpolation error can be decreased by using more reference velocities or by decreasing the size of the time step. . . . .  | 48 |
| 3.5 | Computation time for forward propagating a wavefield for various values of the speedup factor $m$ using equation (3.57). . . . .   | 48 |
| 3.6 | (a) A snapshot of a wavefield propagated with second-order pseudospectral method using equation (3.37). (b) A snapshot of a wavefield propagated with forth-order pseudospectral method using equation (3.23). (c) A snapshot of a wavefield propagated with first-order split-step correction with one correction term in equation (3.40). (d) A snapshot of a wavefield propagated with second-order split-step correction with two correction terms in equation (3.40). . . . .   | 49 |

|      |   |    |
|------|---|----|
| 3.7  | (a) A snapshot of a wavefield propagated with a one-way in time pseudospectral method. Five terms in the power series expansion of equation (3.61) with respect to $v = 0$ were used. The time-step size is 5ms. (b) A snapshot of a wavefield propagated with a one-way in time wave equation approximated with a POU with three windows with a time step of 9ms derived in equation (3.63). (c) A snapshot of a wavefield propagated with a second order pseudospectral method applied to equation (A.19). (d) A three window POU applied to the evolutionary equation with a time step of 9ms using equation (3.53).   | 50 |
| 3.8  | (a) A section of the BP data set showing the high velocity salt dome. (b) A snapshot of a wavefield propagated with equation (3.37) using a POU with two windows. (c) Same as (b) but using a 4 window POU.   | 51 |
| 3.9  | (a) A snapshot generated with a fourth-order pseudospectral method with correction term from equation 3.30. (b) First-order split-step PSTS with three windows. (c) The PSTS equation with no split-step correction using 10 evenly spaced reference velocities. (d) Same as (c) but 20 reference velocities were chosen.   | 52 |
| 3.10 | (a) Velocity profile for a 2-D three layer velocity model. (b) Shot record generated using the PSTS equation. (c) A Shot record generated using second-order time fourth-order in space FD solver.  | 53 |
| 4.1  | Comparison of SV and P forward modelling impulse response for wavefield propagation $V_p = 2965, V_s = 1485, \epsilon = 0.196, \delta = 0.1$ , and the tilt angle $\beta = 30^\circ$ . The propagation of P and SV waves are done separately.   | 62 |
| 4.2  | SV and P wave impulse responses with Thomsen's anisotropic specified as $V_p = 2965, V_s = 1485, \epsilon = 0.196, \delta = -0.2$ , and the tilt angle $\beta = 30^\circ$ .   | 63 |
| 5.1  | (a) Impulse migration response for a single far offset trace resampled prior to crosscorrelation to half the Nyquist sampling rate. (b) The migration impulse response with no resampling.  | 68 |
| 5.2  | Impulse response in a constant velocity medium for an offset trace with the Laplacian filtering applied. The trace was created by convolving a trace containing 5 nonzero elements with a zero phase Ormsby wavelet. (a) Shot illumination condition with input trace integrated twice. (b) Crosscorrelation imaging condition with the input trace integrated twice. (c) Shot illumination condition with input trace integrated once. (d) Crosscorrelation imaging condition with the input trace integrated once. (e) Shot illumination condition with the input trace not integrated. (f) Crosscorrelation imaging condition with the input trace not integrated. | 71 |

|     |  |    |
|-----|--|----|
| 5.3 | The same parameters used in Figure 5.2 except no Laplacian filter was applied to the migrated impulse responses. . . . .   | 72 |
| 5.4 | The same impulse responses with the parameters used in Figure 5.2 except no Laplacian filter was applied to the migrated impulse responses and the velocities from the Hess data was used which is Figure 5.8. . . . .   | 73 |
| 5.5 | The same impulse response parameters used in Figure 5.2 except with the Hess vertical velocity in Figure 5.8 was used in the migration and the trace was taken from the Hess VTI dataset. . . . .  | 74 |
| 5.6 | The migration impulse responses for an offset trace with the Hess velocity field used for the migration velocities and with a trace from the Hess VTI dataset. (a) The input trace was integrated twice. (b) The input trace was integrated twice, and the Laplacian filter was applied to the migration response. (c) The input trace was integrated once. (d) The input trace was integrated once, and the Laplacian filter was applied to the migration response. (e) The input trace was not integrated. (f) The input trace was not integrated, and the Laplacian filter was applied to the migration response. . . . . | 75 |
| 5.7 | The same migration responses as in Figure 5.6 except the source wavelet was not integrated. . . . .  | 76 |
| 5.8 | vpp . . . . .  | 77 |
| 6.1 | A statement of reciprocity. . . . .  | 81 |
| 6.2 | Top: A node gather for the OBC CCGVertias dataset for the vertical geophone. Bottom: A shot gather for the CGGVeritas dataset for the vertical geophone. . . . .   | 82 |
| 7.1 | (a) A snapshot during forward propagation with the Marmousi velocity model using equation (3.37) with a minimum phase wavelet injected at the surface using 2 reference velocities with a time step of $1.5ms$ , and a grid-spacing of $12.5m$ . (b) The same snapshot as (a) but with 4 reference velocities. (c) A snapshot using second-order time and fourth-order space FD solver with a time step of $0.295ms$ and grid spacing of $5m$ . (d) Similar to (c) but with a time step of $0.195ms$ and grid spacing of $5m$ . . . . .  | 85 |
| 7.2 | An image of the Marmousi data set using PSTS RTM with 4 reference velocities. The image is the stack of 240 migrated shot records. The time step was $0.0015ms$ and the grid spacing was $12.5m$ . The grid spacing for the crosscorrelation is $3.13m$ . . . . .  | 86 |

|      |   |    |
|------|---|----|
| 7.3  | An image the Marmousi data set using PSTS RTM with 4 reference velocities. The time step was 0.0015ms and the grid spacing was 8.3m. The imaging condition grid sampling is 4.15m. . . . .  | 87 |
| 7.4  | A RTM of the Marmousi data set using a second-order time and fourth-order space explicit FD solver. The time step was .46ms and the grid spacing was 5m. . . . .  | 88 |
| 7.5  | Similar to Figure 7.4 except the time step was halved and therefore the computational time doubled. . . . .   | 89 |
| 7.6  | A fourth-order in time Lax-Wendroff pseudospectral RTM of the Marmousi dataset. The size of the grid is 12.5m and the size of the time step is 1.5ms. The crosscorrelation grid spacing is 6.25m. . . . .   | 90 |
| 7.7  | PP reflectivity for the HESS velocity model. . . . .  | 91 |
| 7.8  | A migrated image of the Hess VTI data set using a VTI RTM. . . . .  | 92 |
| 7.9  | Vertical P-wave velocity of the FRP ramp model. The ramp has been flooded with the velocity above it. The overburden has a value of $V_p = \epsilon = 0.196$ , $\delta = 0$ , and tilt angle of $\beta = 45^\circ$ . The lower velocity layer is isotropic. . . . .   | 93 |
| 7.10 | A migrated image of the PP data for the FRP ramp model which has TTI overburden. . . . .  | 94 |
| 7.11 | OBC PP and PS imaging of synthetic data set made with ray tracing. The amplitudes are constant on the reflection. (a) An ocean bottom cable geometry (OBC) with an S-wave source. This is kinematically equivalent to a node gather. (b) PS synthetic data, made with constant amplitude. (c) PP image of a migrated shot made with travel times only. (d) PS image of a migrated shot made with travel times only. . . . . | 95 |
| 7.12 | The P-wave velocity of an OBC dataset provide by CGGVeritas. The units of the velocity are in $m/s$ . . . . .   | 96 |
| 7.13 | A migrated image of an ocean bottom cable (OBC) dataset obtained from CGGVeritas. The velocity model is isotropic. The node spacing on the seabed surface is 100m and the shot spacing is 12.5m. The dataset was generated with an elastic wave equation. . . . .   | 97 |

# List of Symbols and Abbreviations

| <b>Symbol</b>  | <b>Description</b>   |
|--|--|
| $\delta, \epsilon, \gamma$   | Thomsen's anisotropy parameters  |
| $\lambda, \mu$   | Lamé's parameters  |
| $c_{ijkl}$   | Stiffness tensor   |
| $C$  | Stiffness matrix in Voigt notation   |
| $\vec{d}$  | Polarization vector  |
| $e_{ij}$   | Strain tensor  |
| $f_{max}$  | The maximum frequency in the dataset   |
| $G(\vec{x}, \vec{x}_0, t, t_0)$  | The free space Green's function for the wave equation                          |
| $\sigma_{ij}$  | Stress tensor  |
| $\rho$   | Density  |
| $\vec{x} = (x, y, z)$  | A point in $\mathbb{R}^3$  |
| $\vec{k} = (k_x, k_y, k_z)$  | The wavenumbers  |
| $\delta t$   | Time step size   |
| $\delta x$   | Grid size  |
| $U(t, \vec{x})$  | The wavefield at time $t$ and position $\vec{x}$                               |
| $\hat{U}(t, \vec{k})$  | The Fourier transform of $U$ at time $t$ and spatial frequency $\vec{k}$       |
| $U^n(\vec{x})$   | The wavefield at time step n   |
| $\Delta = \frac{\partial}{\partial x_i} \frac{\partial}{\partial x_i}$ | Laplacian using Einstein's summation convention                                |
| $\Delta^2 U$   | The Laplacian applied twice to the wavefield $U$                               |
| $\sqrt{-\Delta U}$   | The square root of the Laplacian which can be calculated in the Fourier domain |
| $v(\vec{x})$   | The scalar velocity field  |
| $\delta v(x)$  | The variation of the velocity field from a constant background $v_0$           |
| $\Omega_j$   | Spatial windowing function for the j-th window                                 |
| $O(\delta t)$  | Big O notation   |
| $\omega$   | Temporal frequency   |
| $\mathcal{F}_{\vec{x} \rightarrow \vec{k}}$                            | Fourier transform computed over space  |
| $\mathcal{F}_{\vec{k} \rightarrow \vec{x}}^{-1}$                       | Inverse Fourier transform computed over wavenumber                             |

|                 |   |
|-----------------|---|
| $\nabla f$      | The gradient of the function $f$                                      |
| $\mathbb{R}$    | The field of real numbers   |
| $\mathbb{R}^3$  | The real coordinate space in 3-D, with elements $\vec{x} = (x, y, z)$ |
| $I(\vec{x})$    | The processed seismic imaged often summed over shots                  |
| $R(t, \vec{x})$ | The back-propagated receiver field                                    |
| $S(t, \vec{x})$ | The forward modelled shot field                                       |
| $\omega(t)$     | The source wavelet  |
| $V_{g_j}(U)$    | The forward Gabor Transform applied to wavefield $U$                  |
| CMP             | Common midpoint   |
| GPSPI           | Generalized phase-shift-plus-interpolation                            |
| FD              | Finite difference   |
| FIO             | Fourier integral operator   |
| FFT             | Fast Fourier transform  |
| NMO             | Normal move out   |
| P-wave          | Pressure wave mode, for anisotropic media a quasi-P-wave              |
| S-wave          | Shear wave mode, for anisotropic media a quasi-S-wave                 |
| SV-wave         | The vertical shear wave   |
| SH-wave         | The horizontal shear wave   |
| $S_1$ -wave     | The fast shear wave   |
| $S_2$ -wave     | The slow shear wave   |
| PS              | A wave that has converted from a P-wave to an S-wave                  |
| PDE             | Partial differential equation   |
| PSPI            | Phase-shift-plus-interpolation  |
| PSTS            | Phase-shift time stepping   |
| POU             | Partition of unity  |
| TTI             | Tilted transverse anisotropy  |
| VTI             | Vertical transverse anisotropy  |
| ODE             | Ordinary differential equation  |
| OBC             | Ocean bottom cable  |
| OBN             | Ocean bottom node   |
| RTM             | Reverse-time migration  |
| $\Psi$ DO       | Pseudodifferential operator   |

# Definitions

**Azimuthal anisotropy:** The azimuthal angle varies from the vertical or z-axis. For example Azimuthal velocity anisotropy or *horizontal transverse isotropy* (HTI) occurs when there is a vertical set of fractures in an isotropic host rock. The isotropy plane is the vertical plane and the symmetry axis is the horizontal direction perpendicular to this plane.

The azimuthal angle varies from the vertical or z-axis. Azimuthal velocity anisotropy occurs when velocity varies with the azimuthal angle.

**Grid dispersion:** When numerically solving an ordinary differential equations or a partial differential equation, as a result of the discretization of the space variables and the finite-difference approximation of the derivatives, low frequency wave travel at a different velocity than higher frequency waves. These solutions are called *dispersive schemes*. A small time step size and spatial grid size reduce the effects of the dispersion.

**Infinite order accuracy:** A numerical scheme for solving an equation is said to be of *infinite order accuracy* if it converges to the exact solution faster than any polynomial accurate solution.

**Imaging condition:** In wave equation migration schemes, comparing the downgoing wavefield (incident wavefield) with an imaging condition to the upgoing wavefield (back-propagated scattered wavefield) approximates the reflectivity.

**Multi-pathing:** Kirchhoff migration typically only connects source and receiver with the first arrival calculated with ray tracing or by solving the eikonal equation. Later arrivals may contribute to the image (Audebert et al., 1997). This effect is especially true for complicated velocity models where there are many possible paths connecting receiver, image point, and shot location.

**Polar anisotropy:** The polar angle is the angle projected on the xy-plane. Polar anisotropy or *vertical transverse anisotropy* (VTI) occurs when the velocity field does not depend on the polar angle. This type of anisotropy is common in flat shales.

**Poststack migration:** A poststack migration scheme assumes that all traces have zero-offset. A zero-offset seismic experiment is approximated in flat geology by

applying normal move out correction to a shot gather.

**Prestack depth migration:** Typically receiver gathers or shot gathers are migrated individually with a minimum of assumptions of how flat the layers are in the subsurface and the degree of lateral velocity variations.

**Prestack time migration:** A number of simplifying assumptions; e.g., that there is mild lateral velocity variation; allow prestack time migrations to produce a seismic image with fewer computation resources and with a crude velocity estimate.

**Seismic imaging:** The process of taking seismic data and making it into an image of the subsurface.

**Shot field:** In RTM, the shot field is the forward modelled wavefield in the subsurface propagated with the estimated velocity model.

**Shot gather or seismogram:** A Shot gather is the receiver recordings from a single source seismic experiment.

**Receiver field:** In RTM, the receiver field is the back-propagated recorded wavefield, which approximates the scatter wavefield in the earth propagated in reverse.



# Chapter 1

## Introduction

Exploration geophysics is the study of physical methods; i.e., seismic, gravitational, magnetic, electrical, and electromagnetic methods, to determine the interior properties of the earth. Many of the interior properties of the earth cannot be measured directly, or are too expensive to measure directly. Remote sensing, with the response to sounds waves, electromagnetic waves or by measuring the gravitational field determines the position, location, and quality of hydrocarbon reservoirs, ore bodies, geothermal reservoirs, ground water reservoirs, and other geological structures. Surface methods determine the interior properties of the earth using active sources and geophones on the earth's surface.

Seismic imaging is a method of exploration geophysics. This process uses a source of energy, typically an air gun, a dynamite explosion, or a vibroseis truck, or less commonly an earthquake, a drill bit, or random noise. The vibrations travel in the earth as a wave and reflect, refract, and transmit throughout the subsurface. Seismic experiments record the energy from vibroseis truck or a dynamic explosion. Geophones record the reflected and refracted sound waves, which measure the vibrations of the ground. Velocity estimates are made in the shallower parts of the model using the refracted energy. The refraction energy is filtered out because it does not contribute to the reflectivity estimate.

Geophones traditionally record the vertical motion of the ground. It is now common to record the 3 directions of motion in the ground with 3-C geophones. In the ocean, vibrations are recorded by strings of hydrophones towed by a ship, which measure the vibrations in the water as a pressure fluctuation. In a typical 2-D seismic experiment on land, hundreds of geophones are planted in a line on the earth's surface. The wave source, typically from a vibroseis truck or a dynamite explosion, is released every one to five geophones for a high-fold survey. The spacing is determined by a tradeoff between acquisition costs and the resolution of the final image for a given type of geology. In a 3-D land experiment, a grid of geophones and shots is recorded on the earth's surface. This allows better imaging but requires more numerically intensive processing. It also frequently under-samples the wavefield (Biondi, 2006) and results in an aliased wavefield. Occasionally, for time lapse seismic surveys, geophones buried several meters below the earth's surface to avoid the complexities of the near surface.

In the ocean, in a typical experiment, a ship pulls several strings of hydrophones several kilometers long while multiple ships release a pulse of acoustic energy with an air gun. Ocean bottom cable (OBC) and ocean bottom node (OBN) technology are more recent developments in acquisition geometry and recording. A ship blasts an air gun near the surface of the ocean which is recorded by an array of 3-component geophones and a hydrophone which are fixed to the bottom of the ocean floor. Ocean bottom nodes are fixed indefinitely at the ocean bottom to allow time-lapse knowledge of a producing field.

A shot record or seismogram is the recording of a seismic experiment that occurs through releasing of a source of energy into the earth and recording of the response with a set of geophones or hydrophones. Data recorded from multiple shot-profile experiments are sorted into common-receiver gathers. In this domain some types of coherent and non-coherent noise are more easily attenuated and filtered out. Additionally, migration is preferred in the common receiver domain depending on sampling and offset length. In the case of ocean bottom node geometry, the shot spacing is more finely sampled than the node spacing, and so common receiver gathers are preferred for migration and filtering.

The goal of exploration geophysics in the oil and gas industry is not only to determine the structure of reservoirs but also rock properties like porosity, fluid content, permeability, and fracture characteristics determined by the stress field, and the elastic parameters. Many of these properties cannot be directly measured from seismic techniques but can be inferred through equivalent media theories, hydrocarbon production data and well logging. Most rocks in the earth are fractured to a certain degree. The fracture network can play a critical role in permeability of the reservoir. Orientated fractures in an isotropic host rock make the rock appear to be anisotropic to the seismic wavefield.

## 1.1 Mathematical description of waves in the earth

The physical process governing waves traveling through the earth can be approximated by a mathematical model. The mathematical model is often a system of partial differential equations (PDEs) with suitable initial and boundary conditions. These PDEs can be solved, given a velocity and density model or a set of elastic parameters, to create synthetic seismograms that can be compared to recorded seismograms. This process of generating synthetic seismograms is called *forward modelling*. There have been a number of mathematical models proposed to describe waves traveling in the earth, including the acoustic wave equation, the elastic wave equation, the eikonal equation, and various ray tracing techniques, as well as more complicated models like visco-acoustic and visco-elastic wave equations (Carcione, 2007). Migration can

be thought of as the first step of the inverse problem. The inverse problem is to determine the material parameters of the earth, knowing the response to an impulse. The inverse problem in seismic imaging is ill-posed and requires regularization procedures to ensure convergence and stability. Complicated mathematical models require the estimation of large number of parameters, which are often highly ill posed (Bleistein et al., 2000).

In seismology, the first attempt to solve the inverse problem is called *migration*. Migration is the process of taking reflections recorded on the earth's surface and transforming them into an image of the interior properties of the earth. Migration enables the collapse of diffraction energy and the movement of reflection energy recorded on the seismic section to its true location.

There is a tradeoff between the complexity of the mathematical model and the tractability and resources required to solve it and the corresponding inverse problem (Bleistein et al., 2000).

Migration algorithms require an approximate velocity field in order to map the reflections to the correct location. The velocity model is normally constructed from well log data, statistical methods based on normal move-out, refraction studies, and earlier outputs of migration with a stacking velocity model determined from processing flows. The first migration methods were graphical methods based on a constant velocity migration (Hagedoorn, 1954). The reflection energy would be spread out in a semicircle. For variable velocity media these semicircles are replaced with travel-time curves, which are based on ray-tracing algorithms.

Migration algorithms have historically treated the earth as a multi-layered fluid. This algorithms only have the properties of density and isotropic P-wave velocity. In this case wavefield propagation is modelled with the acoustic wave equation.

More complicated models, based on the elastic wave equation, have 21 independent coefficients in the stiffness tensor which is commonly written done in a symmetric 6 by 6 matrix, plus density at each spatial location. Poro/fractured viscous-elastic medium have more independent coefficients, and therefore, the inverse problem is more difficult. The elastic medium approximation of the earth has been used in global geophysics successfully for a long time. The difference in the time delay of P-waves and S-waves determines how far away an earthquake epicenter is as well as to determine the structures deep within the earth (Shearer, 2009).

## 1.2 Numerical solution of the wave equation

The wave equation can be solved using finite-difference (FD) operators. FD operators have many advantages. FD operators are easy to implement, and their accuracy and stability are well understood. Absorbing boundary conditions are implemented to

eliminate reflections and instabilities at the boundary. At the surface boundary of the model either absorbing boundary conditions are used to simplify the wavefield or a free surface boundary condition is used that reflects all the energy. FD operators also have disadvantages. FD operators are dispersive or inaccurate at large wavenumber, and FD operators must be spatially over-sampled to avoid grid dispersion. The Laplacian in the wave equation can be approximated with any order FD stencil, and generally the higher-order FD operators require less over sampling and are more computationally efficient. The elastic wave equation can be solved with FD operators as well. As a result of stability issues associated with the slowly traveling interface waves, elastic FD solvers typically use a staggered grid. Fourier pseudospectral solvers calculate the Laplacian more accurately. However, Fourier pseudospectral solvers require more padding to prevent wraparound error and it is more complicated to implement free surface boundary conditions.

Efficient numerical solutions of the wave equation are important for migration algorithms. Recent improvements to computer hardware, including parallel computers and GPUs, have made wave equation based modelling and migration feasible.

### 1.3 Improving migration algorithms

The earth attenuates the seismic wavefield. The constant Q-model (Aki and Richards, 2002) is a good approximation for attenuation in the seismic frequency band. In the constant Q-model, attenuation is proportional to the number of cycles the wave undergoes. Amplitudes decay with the number of wave cycles, excluding the effects of geometric spreading and losses from reflections and transmissions. Higher frequencies undergo more cycles per meter, and, therefore, the high frequencies are more attenuated. Amplitude decay and phase distortions are normally corrected by deconvolution techniques (Margrave and Lamoureux, 2002).

There is no source that is perfectly impulsive, and, in addition, the earth attenuates higher frequencies more quickly, and so the seismic wavefield is band limited. As a result, it is necessary to limit our objective to creating an image of the contrast in velocity and density (Bleistein et al., 2000). In other words, the objective is to create an image of the reflectivity or impedance. This process is called migration. Migration can be thought of as an approximation to the inverse problem. Migration can also be understood to be the process of taking reflection events and geometrically relocating them to the correct position, in order to create an image of the earth. A variety of techniques have been developed to perform migration depending on the geology, quality of the seismic data, and the need for an accurate image. The lack of high frequency content limits the resolution of the seismic surveys.

Reverse-time migration (RTM) transforms preprocessed seismic data into an im-

age of the earth using wavefield propagation and an imaging condition. The pre-processing steps isolate the reflected P-wave energy from the seismic dataset and corrects for the attenuation of the earth. Traditionally, seismic migration has been conducted through Kirchhoff migration or by depth continuation methods. Kirchhoff migrations rely on ray tracing methods that are inaccurate in heterogeneous velocity models. Depth continuation migrations allow multi-pathing but have problems imaging steep dips and structures using overturning waves.

Many migration algorithms are based on the acoustic wave equation and so can't handle velocity anisotropy. Vertical velocity anisotropy (VTI) has the same velocity in the horizontal plane but varying velocity from horizontal to vertical. A useful model of anisotropy for seismic processing is called tilted transverse anisotropy (TTI). TTI media a VTI media at a tilt angle relative to vertical. TTI RTM algorithms suffer stability issues which can constrain the combination of TTI anisotropic parameters. Many TTI wavefield propagators contain parasitic S-waves that add noise and create stability issues. This thesis, investigates anisotropic wavefield propagators that are free of S-wave artifacts and have no restriction on the range of anisotropic parameters. S-wave Wavefield propagators for anisotropic media are also derived.

Converted waves are P-waves that transform upon reflection into S-waves. S-waves are much more sensitive to rock properties like anisotropy and attenuation. Converted wave images offer the potential to provide a secondary image when the P-wave data is poor. More commonly converted wave data supplements P-wave data for the purpose of determine rock properties, like the elastic coefficients, fracture orientation and intensity. S-wave splitting can be determined without outputting a final image. S-wave splitting observed in seismic data is thought be caused at the reservoir level by vertically aligned fractures. In addition, the converted wave image is used for joint AVO and AVAZ analysis.

Converted wave imaging is much more difficult than pressure-pressure (PP) imaging. Shear waves are more affected by the weathering layer, which produces severe time jumps and attenuation of the seismic data. Converted waves flip polarity at zero-offset where they have zero amplitude. This polarity flip must be determined prior to migration via the asymptotic conversion point approximation or as a part of migration by looking at the common image gathers. OBC seismic data has fewer near surface complexities than land data and so converted imaging has had more success.

Converted wave migration is most commonly done via Kirchhoff time migration (Cary and Zhang, 2010). Converted wave Kirchhoff time migration is commonly used because the biggest challenges in converted wave imaging are in building an S-wave velocity model, geophones orientation, wavefield separation, correcting and solving for shear wave splitting effects and solving for the near surface statics. Since the PP data is often migrated with prestack depth migration it is necessary to match the converted wave data with a similar migration algorithm or via adhoc stretching

data stretching algorithms. An example of VTI downward continuation migration for converted waves is Pedersen et al. (2010). Later, an implementation of converted wave isotropic reverse time migration for an OBC dataset is presented.

## 1.4 Prestack-depth migration

Prestack depth migration is required for an accurate image in areas of complex geology, i.e., thrust faults, reefs, salt domes, and nonconformities. Generally there are two different types of prestack depth migration algorithms: (1) Those that are based on calculation of travel times via ray theory like Kirchhoff migration, Gaussian beam migration, and similar beam migrations, and (2) wave equation migrations. Wave equation migrations directly solve a wave equation and offer a more faithful account of kinematics and dynamics of the wavefield, whereas Kirchhoff migrations are based on an asymptotic solution of the wave equation via the eikonal equation and are not as accurate.

The different types of prestack depth migration algorithms also have a variety of tradeoffs in terms of ease of velocity model building, computational efficiency, memory requirements and whether they handle multipathing, anisotropy, irregular sampling, aliased data, migration noise, accuracy, overturned reflections and steeply dipping events.

In this chapter prestack depth migration is reviewed. The basics of preprocessing seismic data, including the critical step of velocity model building, are briefly described. Reverse-time migration is a wave equation based prestack depth migration technique that will be the focus of future chapters and will be introduced at the end of this chapter.

## 1.5 Processing seismic data prior to migration

Processing seismic data before migration is essential to creating a useful image of the subsurface. The preprocessing of seismic data involves a number of processes and algorithms and requires a great amount of experimentation, depending on the regional geology, local conditions, and quality of seismic data. Some of the important components involve isolating the reflection events by removing multiples, noise, refraction events, converted waves, and surface waves, resampling and regularizing the data to satisfy the requirements of migration algorithm. In addition, every migration algorithm requires a velocity model that is similar to earth's velocity field. For a comprehensive introduction the book by Yilmaz (2001) is recommended.

Seismic imaging typically treats non-primary reflection energy as noisy. Stacking increases the signal-to-noise ratio of the final image, provided that the reflectors are imaged correctly. However, it is desirable to remove as much non-primary energy as possible before migration and stacking. Surface waves and interface waves or refractions can be modeled and removed, as they have different move out and frequency spectrum than the reflected waves. For towed-streamer and OBC data, the reflections from the ocean surface and water bottom are very strong and so removing the ghost,

water bottom, and free surface multiples are essential to making a good image.

The wavefield is composed of P-waves and S-waves. Because of the near surface velocity gradient, P-wave and S-waves for near offset traces show up on the vertical component and the horizontal components, respectively. However, a residual analysis is necessary to for geophone orientation and removal of P-waves from the horizontal components, especially for long offset data sets.

The seismic wavefield is highly attenuated by the earth. This both decreases the relative amplitude of the high-frequency components of the data and changes of the phase the data. Deconvolution is a powerful processing technique to remove the amplitude decay and phase distortions caused by attenuation.

## 1.6 Time migration and depth migration

Some of the first migration algorithms developed are called time migrations because the output depth coordinate was time. Some examples are Stolt migration (Stolt, 1978), Gazdag migration (Gazdag, 1978), Finite-difference migration, and Kirchhoff time migration (Schneider, 1978). Time migrations do not require an accurate velocity model but in the presences of lateral velocity variations produce an inaccurate result. They typically make approximations that make them computationally efficient. Depth migration algorithms generally honours lateral velocity variations but requires a more accurate velocity model. The velocity model is constructed using costly statistical techniques and multiple iterations of migration. Depth migration is considered a requirement whenever there are strong topographic changes, faulting, salt bodies or complex folds.

## 1.7 Poststack and prestack migration

The common midpoint (CMP) gathers are a good approximation to the common depth point (CDP) gather in simple geological areas. In this case, NMO applied to the CMP gathers are a good approximation of a zero-offset seismic section. Stacking refers to summing together multiple shot records. Either shots have normal move-out applied prior to migration, which is called post-stack migration, or each shot-record is migrated separately and then stacked. When the normal move-out is non-hyperbolic and because of CMP smearing, poststack migration produces a blurred image (Yilmaz, 2001). Poststack has been traditionally used because it is cheaper and works well in areas that have flat layers. However, in areas of complex geology, prestack migration is essential to obtaining an accurate image.

## 1.8 Velocity building

The most time consuming and difficult preprocessing step is to construct a velocity model. Often there is logged wellbore data that seismic velocities can be estimated from. However, well logging is typically incomplete, covering only the area of interests near the reservoirs.

A variety of statistical techniques have been developed to estimate a background velocity model mostly based on semblance and flattening of CMP gathers (which is outside the scope of this thesis). Also, when an anisotropic velocity model is used, the number of spatial varying parameters goes up from one to 5 parameters for TTI medium and 11 Parameters for orthorhombic media plus orientation angles for the symmetry axis.

Tomographic ray based determination of the velocity structure from refraction and reflection arrivals is standard practice (Woodward et al., 2008). Full waveform inversion can be used to build a velocity model; however, it has limited use because of problems with convergence and computational burden. Wavepath tomography uses the common image gathers from wave equation migration to update the velocity model (Fliedner and Bevc, 2008).

## 1.9 Kirchhoff and Gaussian beam migrations

Kirchhoff migration (KM) has traditionally been the workhorse migration algorithm of the seismic processing industry (Gray et al., 2001; Etgen et al., 2009). KM algorithms map reflection events into an image of the subsurface reflectors directly using precomputed tables of travel times calculated with ray tracing or solutions to the eikonal equation. KM is computationally efficient and it is easy to use for velocity model building as it is possible migrate a small portion of the output image. KM can handle irregular geometries where other more accurate migration algorithms require regularization and interpolation of the data to prevent aliasing and satisfy the assumptions of the migration algorithms.

Gaussian beam migration (Hill, 1990, 2001; Gray, 2005) offers many of the advantages of Kirchhoff migration but allows multipathing by the superposition of Gaussian beams. It is more efficient than depth continuation algorithms while being nearly as accurate. Generally it cannot handle multiples or duplex waves that a reverse time migration can.

## 1.10 Two-way versus one-way wave equation

Acoustic wave equations are either one-way or two-way. The two-way wave equations more accurately model the kinematics and dynamics of wave motion of the earth, especially in areas that are complex. Its computational costs are greater than one-way equations but are of comparable magnitude. The one-way wave equations model wave propagation in a single direction, generally either up-going or down going. Waves past 90° to the preferred direction cannot be propagated. However the areas that depth continuation cannot image typically require a very good velocity model that is very hard to build and these areas are typically poorly illuminated because of the source and receiver configurations (Mulder and Plessix, 2004).

## 1.11 Depth-continuation migrations

Seismic migration by phase-shift depth stepping (Gazdag, 1978) is accurate and efficient, provided that there are no lateral velocity variations but only propagates the wavefield in a preferred direction. Phase-shift-plus interpolation (PSPI) was presented by Gazdag and Sguazzero (1984) as an approximate extension to deal with lateral-velocity variations. PSPI spatially interpolates a set of extrapolated wavefields propagated with constant velocities to form a wavefield extrapolated with a variable velocity.

The principle of phase-shift depth stepping is based on approximating the two-way wave equation by a one-way wave equation in a preferred direction, normally taken to be vertical. The resulting one-way wave equation is solved in the Fourier domain. While highly accurate for waves propagating in the preferred direction in a constant-velocity medium, the approximation is inaccurate at steep dips and high lateral velocity contrast (e.g., de Hoop et al., 2000). The concept of one-way wave propagation by phase shifts has been extended in the literature in order to better handle stability and accuracy when the velocity varies in the lateral direction (Stoffa et al., 1990; Wu and Huang, 1992; de Hoop et al., 2000). Margrave and Ferguson (1999) showed that the GPSPI (generalized phase-shift-plus-interpolation) Fourier integral is the limit of PSPI in the extreme case of using a distinct reference velocity for each output location. The Gabor method of windowed Fourier transforms can be used (Ma and Margrave, 2008) to approximate GPSPI by choosing a collection of reference velocities according to an error criterion called lateral position error.

Depth-continuation migrations rely on downward propagation of a wavefield in depth by solving a one-way wave equation. When  $U$  is Fourier transformed over the spatial coordinates  $x$  and  $y$ , and the time variable  $t$ , the one-way wave equation is

$$\frac{\partial U}{\partial z}(t, k_x, k_y, z) = \pm i2\pi k_z U(t, k_x, k_y, z), \quad (1.1)$$

where the  $\pm$  signs denote the downward and upward wavefields, respectively and

$$k_z = \pm \sqrt{\frac{\omega^2}{v^2} - k_x^2}. \quad (1.2)$$

In the case of constant velocity the solution can be calculated at progressive depth steps by the formula,

$$U(\omega, k_x, k_y, z + \delta z) = e^{\pm i 2\pi k_z \delta z} U(\omega, k_x, k_y, z). \quad (1.3)$$

Equation (1.3) is the basis for one-way wave propagation. Equation (1.3) can be used to downward propagate in homogenous layers with the corresponding velocity of the layer.

The downward propagated shot field and the upward propagating receiver field are compared with imaging condition to produce the image of reflectivity or impedance. Claerbout (1971) proposed the deconvolution imaging condition,

$$I(\vec{x}) = \int \frac{U(\vec{x}, \omega)}{D(\vec{x}, \omega)} d\omega, \quad (1.4)$$

and the crosscorrelation imaging condition,

$$I(\vec{x}) = \int U(\vec{x}, \omega) D(\vec{x}, \omega) d\omega, \quad (1.5)$$

where  $D$  is the down-going wavefield and  $U$  is the up-going or backscatter wavefield.

A significant challenge in depth continuation wavefield propagation is dealing with the square root in the equation (1.2). The square root changes the relative easy to solve linear partial differential equations into a pseudodifferential operator equation, which is defined with the help of the Fourier transform. The square root operator has singularities at  $\pm 90^\circ$ . The square root operator changes character at  $\pm 90^\circ$  from hyperbolic propagation to evanescent propagation, which slows down the rate of convergence of any numerical algorithm (Etgen et al., 2009). This forces downward continuation algorithms to be unable to propagate horizontally traveling waves and thus rendering it impossible to image salt flanks at and beyond  $90^\circ$ .

There have been adaptations of depth continuation algorithm to allow imaging past  $90^\circ$ . Tilted-plane wave migration (Rietveld and Berkhouit, 1994; Whitmore, 1995) aligns the preferred direction perpendicular to the plane wave. The final image is a stack of plane waves with a variety of tilts. For more complex media; i.e, imaging beneath salt domes, the preferred directions can be constructed about sets of preferred rays. This process, Riemannian wavefield propagation, was introduced in Shragge (2008) and Sava and Fomel (2005).

## 1.12 Reverse-time migration

Reverse-time migration (RTM) (Baysal et al., 1983; McMechan, 1983; Whitmore, 1983) is a depth migration algorithm capable of overturned reflectors and multiple energy while using very accurate two-way wavefield propagation. While RTM is potentially the most accurate migration algorithm, it faces two limitations. Migration artifacts from the imaging condition blur the final image and computational issues mean that repeated use of RTM is expensive. RTM is based on the two-way wave equation, and so it more computationally intensive than migrations based on one-way wave equations.

RTM has traditionally been lightly used because of the large computation resources it requires. As with forward modeling with the wave equation, as a result of the sampling requirements, processing seismic surveys with RTM will require either low-pass filtering to remove higher frequency data or long run times even with a cluster of computers. The fine sampling requirements occur because finite-difference operators propagate high frequencies with an incorrect dispersion relation (Cohen, 2001). An example of the impressive performance, yet low frequency response, is given in Jones et al. (2007). Pseudospectral methods and high-order FD methods reduce the sample requirements but are still computationally expensive.

The velocity wavefield in the earth is very complex, and even more so in areas with over thrust faults and salt domes. Migration algorithms like Kirchhoff migration and depth continuation migrations are not consistent with velocity or wave propagation in the earth. Kirchhoff migration uses only the first arrival travel time calculated by ray tracing, which does not include the full complexity of the acoustic or elastic wavefield. Depth continuation migrations either crudely interpolate the velocity in the lateral direction or have stability issues with high lateral velocity variations. In addition, turning waves and duplex waves and higher order multiples cannot generally be imaged.

A seismogram is a forward propagated in time, band-limited impulse response, through the velocity field where the impulse is introduced at the location of the shot. The receiver field is the recorded wavefield propagated backwards in time. Specifically, wavefield is back propagated with the recorded wavefield used as a time dependent boundary condition at the surface. The shot field is stepped from zero time to the maximum record time, in principle storing each time step in memory, before the receiver field can be stepped backwards in time.

The zero-lag cross-correlation imaging condition (Chattopadhyay and McMechan, 2008) requires shot and receiver fields to be cross-correlated in the reverse order in which they are computed. Either the shot or the receiver field must be in the reverse to computation order.

There have been a number of alternatives proposed to speed up the runtime for

RTM. The excitation imaging condition (Chang and McMechan, 1986) forward models a shot using asymptotic ray theory and back propagates the receiver field using a finite-difference solution of the wave equation. The resulting scheme suffers because of approximations made in computing the shot field. Higher-order finite-difference schemes for computing the Laplacian have been studied extensively. For example, pseudo-spectral methods allow an infinite-order space approximation but generally use a lower-order approximation for the time step (Cohen, 2001). Parallel computers have been used to speed up the computation and for domain decomposition when the memory required for a single shot exceeds the fast ram of a computer (Furumura et al., 1998). The imaging condition is typically done by zero-lag cross correlation of shot and receiver fields. The imaging condition produces artifacts because a wave in the shot field will correlate with one in the receiver field, even if they are moving in the same direction and therefore cannot be a reflection event. Various alternative versions of the imaging condition have also been studied (Fletcher et al., 2006; Guitton et al., 2007; Chattopadhyay and McMechan, 2008) with shot-illumination cross-correlation imaging condition being a common conclusion.

### 1.13 Significant contributions

### 1.14 Chapter summaries

In chapter 2, prestack depth migration is reviewed. The basic algorithms for migration and their limitations are discussed. The different migration algorithms, for example Kirchhoff migration, Gaussian Beam, depth continuation, and reverse-time migration and the challenges with applying them to seismic data are discussed. This will provide the necessary background for further development of imaging conditions, reverse-time migration, and processing converted wave data in anisotropic media.

In chapter 3, the elastic wave equation and anisotropy are reviewed. In particular, this section shows how the Kelvin-Christoffel equation gives rise to the anisotropic phase velocities for P and S-waves.

In chapter 4, finite-differences methods and Fourier pseudospectral methods are reviewed for wavefield propagation in acoustic media. This chapter then presents an alternative set of methods that operate in the wavenumber domain and that have less dispersion than pseudospectral or finite-difference methods.

In Chapter 5, anisotropic pseudo-acoustic wavefield propagation is reviewed for P-waves and S-waves. The pseudo-acoustic wave equations model the anisotropic properties of the earth without the numerical complexity and complex behavior like mode conversions, wavefield separation, and interface waves of the full elastic equation. These pseudo-acoustic wave equations are also an alternative to reduce system

wave equations that are derived from the elastic wave equation.

In chapter 6, imaging conditions in reverse time migration are reviewed. In RTM, a forward modelling shot field is correlated with back propagated record wavefield. This correlation is supposed to produce the image. However, there is a significant amount of crosstalk that results in a noise solution. A number of solutions to reduce the amount of crosstalk are tested while well careful consideration is made to avoid aliasing and undersampling of the imaging condition operator.

In chapter 7, OBC geometry for recording seismic data sets is reviewed. This section presents an implementation of converted wave reverse-time migration. Converted wave migration requires considerable amounts of computation resources as a result of the slow propagation speeds.

In chapter 8, the migration algorithms developments in previous chapters are tested on a variety of synthetic seismic PP and PS data sets.

In chapter 9, conclusions and directions for future study are presented.

In the appendices, key mathematical facts and definitions necessary for the reading of the thesis are presented here that would otherwise interrupt the flow.

# Chapter 2

## The elastic wave equation

### 2.1 Introduction

In this chapter, the theory of the elastic wave equation is reviewed. When ignoring the effects of anelasticity, the elastic wave equation provides an ideal model of the motion of sound waves traveling through the earth. Traditionally, migration algorithms are based on wave propagation in a multi-layer fluid, the acoustic wave equation. This model handles geometric spreading and travel times accurately. The acoustic wave equation does not model anisotropy, and since it does not support shear waves, it cannot handle S-wave splitting or mode conversions. For an isotropic homogeneous elastic solid, P-wave and S-waves do not convert and can be propagated separately with an acoustic wave equation with the corresponding phase velocities.

For elastic media, the dispersion relation is derived to determine the speed of travel of P-waves and S-waves. The velocities of the P and S body-wave modes can be isolated from the dispersion relation and can be used to form pseudo-acoustic wave equations or reduce system wave equations. However, deriving pseudo-acoustic equations that can be solved and that are stable requires various approximations of the dispersion relations and clever parameterizations. Various dispersion relations for the different simplifications of the stiffness tensor such as VTI, HTI, and orthorhombic media are discussed.

### 2.2 The elastic wave equation

Wave propagation in a linear elastic anisotropic, and heterogeneous media is governed by Newton's second law,

$$\rho \ddot{u}_j = \sigma_{jl,l} + f_j, \quad (2.1)$$

where  $\rho$  is the density,  $u_j$  is the component of the displacement in the  $j^{th}$  direction,  $\sigma_{jl}$  are the components of the Cauchy stress tensor, and  $f_j$  is the body force. The Einstein summation convention is used, which means that repeated indexes are summed over. The term  $\sigma_{jl,k}$  refers to taking the derivative of the stress tensor with respect to the  $k^{th}$  coordinate. The second time derivative is denoted by  $\ddot{u}_j$ .

For an elastic media, the stress-strain relation, constitutive equation, or generalized Hooke's law is,

$$\sigma_{ij} = c_{ijpq}\epsilon_{pq}, \quad (2.2)$$

where the strain is,

$$\epsilon_{pq} = \frac{1}{2}(u_{p,q} + u_{q,p}) \quad (2.3)$$

and the stiffness tensor is  $c_{ijpq}$ . Under a coordinate transform  $x'_j(x_m)$ , the strain or stress transforms by the rule,

$$\sigma'_{mn} = \frac{\partial x'_m}{\partial x_i} \frac{\partial x'_n}{\partial x_j} \sigma_{ij}. \quad (2.4)$$

The stiffness matrix being a fourth rank tensor transforms according to the rule,

$$c'_{mnlk} = \frac{\partial x'_m}{\partial x_i} \frac{\partial x'_n}{\partial x_j} \frac{\partial x'_l}{\partial x_r} \frac{\partial x'_k}{\partial x_s} c_{ijrs}. \quad (2.5)$$

The stiffness tensor inherits a number of symmetries from the symmetries of  $\sigma_{ij}$ ,  $\epsilon_{pq}$ ,

$$c_{ijpq} = c_{jipq} = c_{jiqp} = c_{ijqp}. \quad (2.6)$$

Additionally, as a result of thermodynamic considerations (Aki and Richards, 2002),

$$c_{ijpq} = c_{pqij}. \quad (2.7)$$

In the Voigt notation the symmetric tensors  $\sigma_{ij}$  and  $\epsilon_{ij}$  can be written as a 6 by 1 matrix,

$$\underline{\sigma} = \begin{bmatrix} \sigma_{11} \\ \sigma_{22} \\ \sigma_{33} \\ \sigma_{23} \\ \sigma_{13} \\ \sigma_{12} \end{bmatrix}, \underline{\epsilon} = \begin{bmatrix} \epsilon_{11} \\ \epsilon_{22} \\ \epsilon_{33} \\ 2\epsilon_{23} \\ 2\epsilon_{13} \\ 2\epsilon_{12} \end{bmatrix}. \quad (2.8)$$

The 21 independent components of the fourth-rank tensor  $c_{ijpq}$  can be written down in a symmetric 6-by-6 matrix because of the symmetries of  $c_{ijpq}$  as,

$$C = \begin{bmatrix} c_{1111} & c_{1122} & c_{1133} & c_{1123} & c_{1113} & c_{1123} \\ & c_{2222} & c_{2233} & c_{2223} & c_{2213} & c_{2223} \\ & & c_{3333} & c_{3323} & c_{3313} & c_{3323} \\ & & & c_{2323} & c_{2313} & c_{2323} \\ & & & & c_{1313} & c_{1323} \\ & & & & & c_{2323} \end{bmatrix}, \quad (2.9)$$

where the blank indexes imply that the matrix is symmetrical. This reindexing of the tensors done in the Voigt notation allows the stress strain relation to written as,

$$\underline{\sigma} = C \underline{\epsilon}, \quad (2.10)$$

however the square matrix  $C$  and columns matrices  $\underline{\sigma}$  and  $\underline{\epsilon}$  no longer transform with respect to a change of coordinates by the ordinary rules of change of basis and so are not tensors. A coordinate transformation may be done by a Bond transformation (Auld, 1973). The Voigt notation is more convenient for writing down the components of the stiffness, stress, and strain explicitly.

### 2.3 Anisotropy

Seismic velocity anisotropy is a widespread phenomenon in the earth's crust. There is a large variety of mechanisms that cause the earth to be anisotropic. Minerals that make up the earth are intrinsically anisotropic. When these mineral grains are preferentially aligned, as they frequently are in shale rock, the resulting seismic velocities are anisotropic. In shale rock, the seismic velocities in the directions of the bedding plane tend to be isotropic while the velocity direction perpendicular to the bedding plane is typically slower. Isotropic rocks that have an anisotropic stress placed on them, or which have aligned systems of fractures, are also anisotropic. The interleaving of thin isotropic sedimentary beds also appears anisotropic at seismic wavelengths Backus (1962). Fracturing of a hydrocarbon reservoir enhances its permeability and therefore increases its hydrocarbon potential. Knowledge of the fracture system and its orientation, as well as of the pressure field, helps determine optimal drilling patterns for placing horizontal oil wells for enhance oil production.

Processing limited offset 2-D seismic data with the assumption of isotropy frequency results in miss-location and blurring of subsurface structures (Yan et al., 2004). Processing wide azimuth 3-D data sets often requires taking anisotropy into account from the outset to focus and position subsurface structures.

A full characterization of anisotropy requires the estimation of the elastic stiffness tensor  $c_{ijkl}$ , which has 21 independent quantities. A number of symmetrical anisotropic models can provide a good approximation to the subsurface. This is because seismic data often has narrow offset and/or narrow azimuthal coverage, and the earth is often weakly anisotropic

When the medium velocities are anisotropic, the P, SV, and SH polarizations are no longer parallel, orthogonal, and orthogonal to the propagation directions, respectively. The modes are properly called quasi pressure(qP) waves, quasi shear vertical (qSV) waves, quasi-shear horizontal (qSH) waves. The q will be omitted, as it is clear when the media are anisotropic.

In the case of isotropic media,

$$c_{ijkl} = \lambda\delta_{ij}\delta_{kl} + \mu(\delta_{ik}\delta_{jl} + \delta_{il}\delta_{jk}) \quad (2.11)$$

or in Voigt form,

$$C = \begin{bmatrix} \lambda + \mu & \lambda & \lambda & 0 & 0 & 0 \\ & \lambda + \mu & \lambda & 0 & 0 & 0 \\ & & \lambda + \mu & 0 & 0 & 0 \\ & & & \mu & 0 & 0 \\ & & & & \mu & 0 \\ & & & & & \mu \end{bmatrix} \quad (2.12)$$

where  $\lambda = C_{11} - 2C_{44}$  and  $\mu = C_{44}$  are Lamé's parameters for isotropic linear elasticity,  $\mu$  representing shear modulus or rigidity and  $\lambda$  is a measure of compressibility when  $\mu$  is ignored.

For vertical transverse isotropic (VTI) media the stiffness is,

$$C = \begin{bmatrix} C_{11} & C_{11} - 2C_{66} & C_{13} & 0 & 0 & 0 \\ & C_{11} & C_{13} & 0 & 0 & 0 \\ & & C_{33} & 0 & 0 & 0 \\ & & & C_{55} & 0 & 0 \\ & & & & C_{55} & 0 \\ & & & & & C_{66} \end{bmatrix}, \quad (2.13)$$

when the isotropy plain is the  $xy$ -plain. The representation of  $C$  depends on orientation of the symmetry axis, which is orthogonal to the symmetry plane, with the  $z$  axis. VTI anisotropy is a good approximation of anisotropy for thin bedding of isotropic rock (Backus, 1962), unfractured shales, horizontal fractures, and due to compaction.

In horizontal transverse anisotropy (HTI) media,

$$C = \begin{bmatrix} C_{11} & C_{11} - 2C_{66} & C_{13} & 0 & 0 & 0 \\ & C_{33} & C_{11} - 2C_{66} & 0 & 0 & 0 \\ & & C_{33} & 0 & 0 & 0 \\ & & & C_{44} & 0 & 0 \\ & & & & C_{55} & 0 \\ & & & & & C_{55} \end{bmatrix}. \quad (2.14)$$

HTI media is a good approximation to isotropic media that is vertically fractured with a single dominant orientation. The isotropy plane is the  $y - z$  plane. Although via Bond transformation HTI media and VTI are equivalent, their properties for seismic imaging, velocity building, and normal move out are very different.

For an isotropic media with two dominant sets of fractures or a fracture VTI media, orthorhombic medium is a better model. Orthorhombic media formed from a VTI background media with vertical fractures has three isotropy planes. The  $x - y$  plane orientated with the bedding and the vertical fractures orientated with either  $y - z$  or  $x - z$  plane. In the natural coordinates for orthorhombic media,

$$C = \begin{bmatrix} C_{11} & C_{12} & C_{13} & 0 & 0 & 0 \\ C_{21} & C_{22} & C_{23} & 0 & 0 & 0 \\ C_{31} & C_{32} & C_{33} & 0 & 0 & 0 \\ 0 & 0 & 0 & C_{44} & 0 & 0 \\ 0 & 0 & 0 & 0 & C_{55} & 0 \\ 0 & 0 & 0 & 0 & 0 & C_{66} \end{bmatrix}. \quad (2.15)$$

If the symmetry plane of monoclinic medium is orthogonal to the  $z$ -axis then the stiffness matrix is,

$$C = \begin{bmatrix} C_{11} & C_{12} & C_{13} & 0 & 0 & C_{16} \\ C_{21} & C_{22} & C_{23} & 0 & 0 & C_{26} \\ C_{31} & C_{32} & C_{33} & 0 & 0 & C_{36} \\ 0 & 0 & 0 & C_{44} & C_{45} & 0 \\ 0 & 0 & 0 & C_{55} & 0 & C_{56} \\ 0 & 0 & 0 & 0 & 0 & C_{66} \end{bmatrix}. \quad (2.16)$$

Triclinic media has no planes or axis of symmetry and in a general has 21 independent components (Grechka et al., 2003),

$$C = \begin{bmatrix} C_{11} & C_{12} & C_{13} & C_{14} & C_{15} & C_{16} \\ C_{21} & C_{22} & C_{23} & C_{24} & C_{25} & C_{26} \\ C_{31} & C_{32} & C_{33} & C_{34} & C_{35} & C_{36} \\ 0 & 0 & 0 & C_{44} & C_{45} & C_{46} \\ 0 & 0 & 0 & C_{55} & C_{56} & 0 \\ 0 & 0 & 0 & 0 & 0 & C_{66} \end{bmatrix}. \quad (2.17)$$

due to the large number of independent components it is difficult to design an inversion procedure and/or statistical techniques to determine the components of  $C$  accurately.

## 2.4 The Kelvin-Christoffel equation

The Kelvin-Christoffel equation governs the wave propagation speed and polarization of the body wave modes. Let  $d_k$  be the polarization vector in the direction of particle displacement,  $s_k$  the slowness vector in the direction of the phase velocity, and  $n_k$

be the normalization of the vector  $s_k$ . Substituting the a plane wave trial solution  $u_k = d_k \exp(i(\omega(s_k x_k - t)))$  into the homogeneous elastic wave equation,

$$\rho \ddot{u}_j = c_{jlmn} u_{m,nl} \quad (2.18)$$

gives the Kelvin-Christoffel equation,

$$(c_{ijkl} n_j n_l - v^2 \rho \delta_{ik}) d_k = 0. \quad (2.19)$$

Let  $G_{ik} = c_{ijkl} n_j n_l$ . Then equation (2.19) reduces to solving the eigenvalue problem,

$$(G_{ik} - v^2 \rho \delta_{ik}) d_k = 0, \quad (2.20)$$

where  $v^2 \rho$  this is the eigenvalue. For homogeneous media the eigenvalues correspond to the velocities

$$(\sqrt{(\lambda + 2\mu)/\rho}, \sqrt{\mu/\rho}, \sqrt{\mu/\rho}),$$

where  $\lambda$  and  $\mu$  are the Lamé parameters. The eigenvectors correspond to the direction of polarization. The repeated eigenvalues  $\mu/\rho$  have eigenvectors that are distinct. As a result the P, SV, and SH polarization vectors form a basis.

In a general anisotropic media, the P-wave polarization is not necessarily in the direction of propagation, but still the polarization directions are orthogonal. As a result we call the P and S-waves quasi-P waves and quasi-S waves.

## 2.5 The earth as a multi-layered fluid

There are two body wave modes that propagated in the elastic earth model. In a seismogram with a P-wave source, reflected pressure waves typically have stronger amplitudes than converted shear waves. This effect occurs because shear wave sources are typically expensive and noisy, and are not possible to excite in the ocean except at the water bottom. This effect means knowledge of the shear-waves (S-waves) typically comes from converted wave data. There is no converted wave at normal incidence. S-waves are typically more sensitive to anisotropy and attenuation than P-waves. For a typical seismic experiment the dominant energy on a vertically oriented geophone is from the pressure wave. This is a result of a velocity gradient in the near surface of the earth, causing ray paths to become vertical.

S-waves are more sensitive to orientated fractured rock than the P-waves. In anisotropic media, S-waves polarized in different directions and traveling in the same direction can travel with a different velocity, which is called s-wave splitting. Although the acoustic wave equation has been a useful tool for modeling and as basis for constructing migration algorithms, it does not properly account for waves that travel in the earth. The elastic wave equation can account for many more aspects of the

seismic wavefield. P-waves and S-waves are coupled whenever there is a density change or a change in the stiffness tensor. An acoustic wave equation doesn't account for the conversion between these two modes. The acoustic wave equation cannot account for P-wave imaging in anisotropic media for using an acoustic wave equation.

A shear wave traveling in the earth splits into a slow and fast wave, whenever the medium is not isotropic, in the direction transverse to the travel path. In particular, a vertically traveling shear wave in an HTI medium will undergo splitting. Correcting for the S-wave splitting is essential for imaging S-waves or converted waves in anisotropic reservoirs. Moreover, the estimation of HTI anisotropy can be an important diagnostic tool to determine orientation and degree of fracturing in the earth Crampin (1981).

## 2.6 Pseudo-acoustic wavefield propagation

Acoustic wave equations do not support anisotropic wavefield propagation. In order to develop migration algorithms that account for anisotropy, it is necessary to study the elastic wave equation. Elastic RTM (Chang and McMechan, 1987) in principle can image all reflected energy with arbitrary types of anisotropy and between any mode. However, imaging with the elastic wave equations requires an estimation of all the coefficients of the stiffness tensor, as well as solving a system of linear partial differential equations. The imaging condition is much more complicated and computational-intensive in elastic RTM as wavefield separation into P and S-waves is required at each time step.

For an isotropic elastic media, the acoustic wave equation can account for geometric spreading and have the same ray paths, but the P-waves will be incorrect because of P-wave energy converts into S-wave energy. For isotropic media, the acoustic wave equation is used because it is robust though it clearly does not account for conversion between different body-wave modes.

Elliptic anisotropy is easy to implement but is a crude approximation of anisotropy in the earth (Thomsen, 1986). Alkhalifah (2000) introduced a PDE wave equation that propagates VTI anisotropic media. This is done by creating a linear PDE with the same dispersion relation as that in the P-SV dispersion relation from the Kelvin-Christoffel equation. These anisotropic wave equations require an approximation to turn them into a fourth order partial differential equation that only propagates P-waves.

Various approximations are used for elastic dispersion relation based on the kind of symmetry. The P, SV, SH-modes can be propagated separately. In qP-wave anisotropic imaging this is more computationally efficient propagation than that with the elastic wave equation.

# Chapter 3

## Wavefield propagation in acoustic media

An efficient and accurate numerical solution of the acoustic wave equation and elastic wave equation is an important tool for forward modeling, inversion, and reverse-time migration. Fourier pseudospectral methods and finite-difference (FD) methods are frequently used to solve the acoustic wave equation because they are easy to implement and are flexible. Fourier pseudospectral methods and finite-difference methods however have large dispersion errors which to reduce these errors requires a small timestep and a fine computational grid.

In this chapter, an exact solution to the constant-velocity acoustic wave equation that is dispersion free is derived. This solution is used to develop numerical methods for the variable-velocity acoustic wave equations that have less dispersion than pseudospectral or FD methods, which we call phase-shift time stepping (PSTS). In addition, methods are proposed for making the time-step larger than the Nyquist sampling rate and for reducing the number of Fourier transforms used to compute a time step for the wave equation solver.

In later chapters, the PSTS solution will be used to implement a RTM and to develop anisotropic pseudo-acoustic wavefield propagators for P-waves and S-waves.

### 3.1 Introduction

Forward modelling of the acoustic wave equation is an important tool for seismic exploration. Forward modeling allows the numerical computation of synthetic seismograms, which can be computed for a variety of different velocity models. These synthetic seismograms can be compared with recorded seismic data to check if a velocity model is a good approximation of the subsurface. The impedance and wave speeds of the earth are unknown for a seismic dataset. As a result, it is difficult to use recorded seismic datasets to benchmark migration algorithms. Therefore, synthetic seismograms are used in conjunction with recorded datasets to benchmark migration algorithms. Synthetic seismograms are also used to determine the acquisition parameters for a seismic survey if estimates of the velocities are known.

There are a number of computational methods for solving the acoustic wave equation. Ray-based methods like the high-frequency approximation of the Kirchhoff-Helmholtz integral (Sommerfeld, 1964) are computationally efficient, can handle rough topography, but are high-frequency solutions which do not account for multipathing (Gray et al., 2001) and are not considered further in this thesis. Fourier pseudospectral methods and FD methods are accurate solvers for the acoustic wave equation that account for multipathing. FD and Pseudospectral methods are compared to methods based on an exact solution for constant velocity models that have minimal dispersion and are adaptable to variable velocity models. In this chapter, alternative methods are explored of solving the wave equation that has been inspired by solutions to the one-way in depth acoustic wave equations that are used for depth-continuation migrations. Wave-equation depth migration methods recursively extrapolate the recorded wavefield in depth, along with the shot field. The shot field and the receiver field are at each depth with an imaging condition to produce an image (Gazdag, 1978; Gazdag and Sguazzero, 1984; Stoffa et al., 1990). In contrast, RTM, like forward modeling, recursively propagates the recorded wavefield and the shot field in time using a two-way wave equation, and then an RTM algorithm compares these wavefields with an imaging condition at each time step.

We consider the time stepping of a wavefield using a phase shift in the time-wavenumber domain as an alternative to FD solution of the wave equation. For the acoustic wave equation, we derive a time-stepping method that, like FD methods, which uses two wavefield snapshots, one in the present and another in the past, to calculate a new snapshot one step in the future. Unlike FD methods, for homogeneous media our phase-shift time-stepping method is exact and displays no dispersion or instability if an aliasing condition is met. For heterogeneous media, we develop a windowed Fourier approximation, essentially a phase shift in the Gabor domain (Ma and Margrave, 2008) that is an approximate propagator with minimal numerical artifacts. This Gabor approximation represents a cosine operator through a chosen number of reference velocities. For each reference velocity we describe the construction of the corresponding spatial windows such that the sum of all windows is unity. The Gabor windows can also be thought of as weights for interpolation between two or more constant velocity propagators to produce a variable velocity propagator. We demonstrate the potential of our method by comparing forward-propagated wavefields and in future chapters by performing prestack reverse-time migration of the Marmousi dataset.

Fourier transforming of the wavefield over the spatial coordinates takes the wavefield into the wavenumber domain. The wavenumber domain is used in pseudospectral methods to calculate the Laplacian of the wavefield. Pseudospectral methods use a FD approximation of time derivative of the wavefield to derive a time-stepping method. The FD approximation of time derivative is dispersive while the Laplacian

is computed with infinite-order accuracy. A solution is said to be dispersive if each frequency component is propagated with a varying velocity. The Lax-Wendroff methods are higher-order time approximations for FD or pseudospectral solutions Cohen (2001). Lax-Wendroff methods use certain combinations of Laplacians applied multiple times to the wavefield to reduce the dispersion caused by the FD approximation of the time derivative.

We investigate an alternative time-stepping equation that does not use FD approximations. Our solution is based on the exact solution to the constant-velocity wave equation, and it does not suffer from numerical dispersion for a constant-velocity medium. We show that our method is essentially a phase shift that depends on velocity and wavenumber, and we call our solution phase-shift time-stepping (PSTS). The fundamental limitation on the time-step size in PSTS arises from a temporal aliasing condition, which we derive. The accuracy and stability properties are demonstrated by comparing solutions of the PSTS equation with FD and pseudospectral methods. We extend PSTS to variable velocity by replacing the global Fourier transform with a Gabor transform using localizing windows within which a homogeneous solution is computed. This extension is no longer exact, but it still allows accurate time stepping with minimal dispersion. The most effective adaptation to variable velocity is a weighted interpolation between constant velocity solutions at each time-step.

The techniques used to derive the time-stepping algorithms are similar to those used to derive depth-continuation algorithms (Soubaras and Zhang, 2008). First, we derive an exact solution to the acoustic wave equation for constant velocity. Then, we explore interpolations and windowed Fourier transform approximations of the constant velocity solutions at each time step to form a solution to the variable velocity wave equations.

### 3.2 Finite-difference methods

FD solutions to the acoustic wave equation allow different types of boundary conditions and initial conditions to be implemented and are easily adaptable to more complex wave equations. However, in FD solutions high-frequency waves travel at a different speed than low-frequency waves. As a result, either a high-order FD scheme is used or a much finer grid spacing and time-step size is used. Generally, high-order FD schemes are more computationally efficient than low-order FD schemes that use a smaller time step.

The acoustic wave equation is,

$$\frac{\partial^2 U}{\partial t^2} = v^2 \left( \frac{\partial^2 U}{\partial x^2} + \frac{\partial^2 U}{\partial y^2} + \frac{\partial^2 U}{\partial z^2} \right), \quad (3.1)$$

where  $U(t, \vec{x})$  is the amplitude of the wave at the point  $(t, \vec{x} = (x, y, z))$ ,  $x, y$  are the

lateral coordinate,  $z$  is the depth coordinate,  $t$  is the time coordinate, and  $v$  is the speed of propagation. Assume  $\vec{x} \in \mathbb{R}^3$  with  $z > 0$  and  $t \geq 0$ . The second-order time derivative of the wavefield can be approximated by the second-ordered centred FD approximation,

$$\frac{\partial^2 U}{\partial t^2}(t) \approx \frac{1}{\delta t^2}(U(t + \delta t) - 2U(t) + U(t - \delta t)). \quad (3.2)$$

Higher-order FD approximations of  $\partial^2 U / \partial t^2$  are unconditionally unstable Cohen (2001). The wavefield at time step  $n$  is,

$$U^n(\vec{x}) = U(n\delta t, \vec{x}). \quad (3.3)$$

A second-order in time solution of equation (3.1) is,

$$U^{n+1} = 2U^n - U^{n-1} + \delta t^2 v^2 \Delta U^n. \quad (3.4)$$

The Laplacian can be approximated by any order of convergence FD stencil. The wavefield at the discrete spatial position  $(m, j, k)$  is,

$$U^n(m, j, k) = U(nt, m\delta x, j\delta x, k\delta x). \quad (3.5)$$

The second-order centered FD approximation of any term in the Laplacian is, for example,

$$\frac{\partial^2 U^n}{\partial x^2}(m, j, k) \approx \frac{1}{\delta x^2}(U^n(m + 1, j, k) - 2U^n(m, j, k) + U^n(m - 1, j, k)). \quad (3.6)$$

The fourth-order approximation is,

$$\begin{aligned} \frac{\partial^2 U^n}{\partial x^2}(m, j, k) \approx & \frac{1}{\delta x^2}(U^n(m + 2, j, k) - 4U^n(m + 1, j, k) + 6U^n(m, j, k) \\ & - 4U^n(m - 1, j, k) + U^n(m - 2, j, k)). \end{aligned} \quad (3.7)$$

The initial conditions for the wave equation are usually taken to be two consecutive snapshots in time and are denoted by  $U^0$  and  $U^1$ .

The FD approximations are said to be dispersive because they propagate the high frequency components with a slow or fast velocity. To obtain an accurate solution the grid spacing must be reduced so that the wavefield is oversampled relative to the stability condition. For second-order in time and space methods, 10 samples per wave length is required to produce an accurate and stable solution.

FD methods require boundary conditions at the edge the computation domain. At the surface, absorbing or free surface boundary conditions are used, depending on the desired complexity of the model. At the sides and bottom of the computational domain a one-way boundary conditions or absorbing boundary condition are used to eliminate unwanted boundary reflections. FD methods are very flexible relative to pseudospectral methods in allowing for design of the boundary conditions.

### 3.3 Two-way time stepping by a phase shift

The constant-velocity wave equation has an analytical solution, which is derived in the wavenumber domain. This solution is efficiently calculated with the fast Fourier transform.

Applying the Fourier transform over the spatial dimensions  $\vec{x} = (x, y, z)$  to both sides of equation (3.1) reduces it to a collection of ordinary differential equations,

$$\frac{\partial^2 \hat{U}}{\partial t^2} = -(2\pi)^2 v^2 (k_x^2 + k_y^2 + k_z^2) \hat{U}. \quad (3.8)$$

When  $\vec{k} \neq 0$ , equation (3.8) has the general solution,

$$\hat{U}(t, \vec{k}) = A(\vec{k}) \cos(2\pi v |\vec{k}| t) + B(\vec{k}) \sin(2\pi v |\vec{k}| t), \quad (3.9)$$

where  $A(\vec{k})$  and  $B(\vec{k})$  are dependent on the initial conditions. The wavenumber dependent frequency,  $\omega(\vec{k})$ , is determined from the dispersion relation,

$$\omega(\vec{k}) = 2\pi v \sqrt{k_x^2 + k_y^2 + k_z^2}. \quad (3.10)$$

Alternatively, the general solution is,

$$\hat{U}(t, \vec{k}) = A_1(\vec{k}) e^{2\pi v |\vec{k}| t} + B_1(\vec{k}) e^{-2\pi v |\vec{k}| t}. \quad (3.11)$$

In the space domain, taking an inverse Fourier transform gives,

$$U(t, \vec{x}) = \int_{\mathbb{R}^3} \left[ A_1(\vec{k}) e^{i(\omega t + 2\pi \vec{k} \cdot \vec{x})} + B_1(\vec{k}) e^{i(-\omega t + 2\pi \vec{k} \cdot \vec{x})} \right] d\vec{k}, \quad (3.12)$$

which is a sum of plane waves,

$$e^{i(\pm \omega t + 2\pi \vec{k} \cdot \vec{x})}, \quad (3.13)$$

with weights  $A_1$  and  $B_1$ .

Subject to the initial conditions,

$$\begin{cases} U(0, \vec{x}) = f(\vec{x}) \\ U(-\delta t, \vec{x}) = g(\vec{x}) \end{cases}, \quad (3.14)$$

the functions  $A$  and  $B$  are determined,

$$\begin{cases} A(\vec{k}) = \hat{f}(\vec{k}) = \hat{U}(0, \vec{k}) \\ B(\vec{k}) \sin(\omega \delta t) = \hat{f}(\vec{k}) \cos(2\pi v |\vec{k}| \delta t) - \hat{g}(\vec{k}) \end{cases}. \quad (3.15)$$

The resulting solution at time  $t = \delta t$  of the constant velocity wave equation is,

$$U(\delta t, \vec{x}) = -U(-\delta t, \vec{x}) + 2\mathcal{F}_{\vec{k} \rightarrow \vec{x}}^{-1}[\cos(2\pi v|\vec{k}|\delta t)\mathcal{F}_{\vec{x} \rightarrow \vec{k}}[U(0, \vec{x})]]. \quad (3.16)$$

The calculation at time step  $n$  corresponding to time  $t = n\delta t$  is expressed as,

$$\begin{aligned} U^0(\vec{x}) &= U(-\delta t, \vec{x}), \\ U^1(\vec{x}) &= U(0, \vec{x}), \\ U^{n+1}(\vec{x}) &= -U^{n-1}(\vec{x}) + 2\mathcal{F}_{\vec{k} \rightarrow \vec{x}}^{-1}[\cos(2\pi v|\vec{k}|\delta t)\mathcal{F}_{\vec{x} \rightarrow \vec{k}}[U^n(\vec{x})]]. \end{aligned} \quad (3.17)$$

For numerical calculations, the FFT is used to compute equation (3.17) because the function  $\cos(2\pi v|\vec{k}|\delta t)\hat{U}^n(\vec{k})$  does not depend only on  $\vec{x}$ . Equation (3.16) takes the Fourier transform of the wavefield and multiplies it with the sum of two phase shifts since,

$$2\cos(2\pi v|\vec{k}|\delta t) = \exp(-2\pi iv|\vec{k}|\delta t) + \exp(2\pi iv|\vec{k}|\delta t). \quad (3.18)$$

As a result, we may think of wavefield propagation as being done in the wavenumber domain by the sum of two phase shifts of opposite sign. Each phase shift depends on the velocity and size of the time step. Equation (3.16) is the fundamental equation for phase-shift time stepping (PSTS), and we will soon adapt it to variable velocity wavefield propagation.

Equation (3.17) can be iterated in the wavenumber domain without shuttling back and forth between the space domain and the wavenumber domain,

$$\hat{U}^{n+1}(\vec{k}) = -\hat{U}^{n-1}(\vec{k}) + 2\cos(2\pi v|\vec{k}|\delta t)\hat{U}^n(\vec{k}). \quad (3.19)$$

However, these time savings are not possible because boundary conditions and source initiation require shuttling back to the space domain.

To demonstrate the effectiveness of recursively using equation (3.16) for wavefield propagation, a minimum phase wavelet is stepped forward in time. The minimum phase wavelet is injected at the center point of a constant velocity two-dimensional model. The response is an expanding circle that decays in amplitude with propagation time. Figure 3.1 is the propagation of a minimum phase wavelet using the phase-shift time-stepper and a second-order FD method. In spite of a much smaller time step, the FD solution shows unacceptable distortion due to numerical grid dispersion.

### 3.4 Initial conditions, boundary conditions, source initiation, and back propagation

When using Fourier pseudospectral methods or the PSTS equation to solve the wave equation, wraparound occurs due to the FFTs. Sponge boundary conditions add

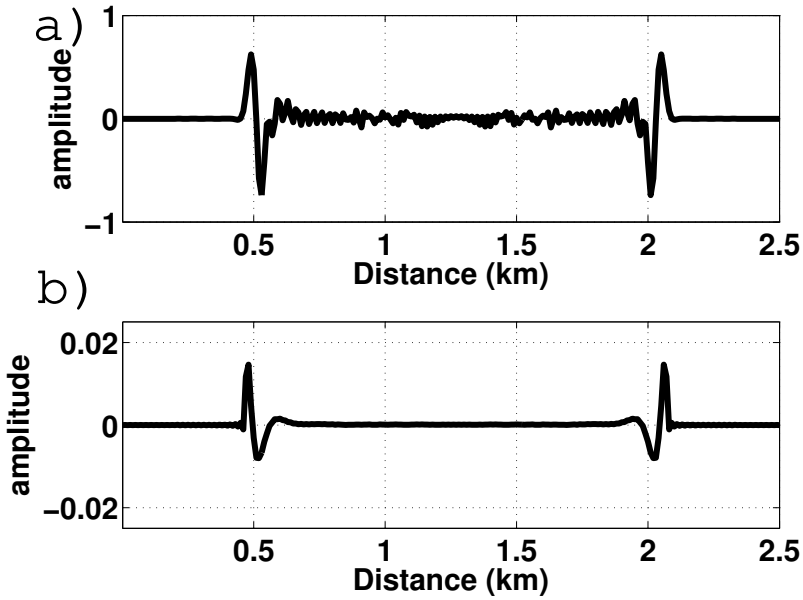


Figure 3.1: The center trace of a wavefield propagated in a constant-velocity model in 2-D. A minimum phase wavelet was injected at the center point of the model. (a) Using finite differences with  $\delta t = 0.0001$ . (b) Using the phase-shift time-stepping equation with  $\delta t = 0.001$ . The low-order FD method took 10 times as long to compute.

either a complex term to the velocity to dampen the waves, or a taper is applied at each time step at the edge of the model. The size of the padding and degree of taper or absorption are normally determined experimentally (Boyd, 1989). The dampening or absorption must be applied gradually to prevent a reflection from the boundary sponge. There is a wide selection of boundary conditions used for FD solutions. Nonreflecting one-way wave operators do a good job at perpendicular incidence but do a poor job for obliquely traveling waves (Cerjan et al., 1985; Clayton and Engquist, 1977). At the surface of the model either a nonreflecting boundary condition can be used to model a free surface or a layer with zero velocity can be added at the top of the model.

To model a source, the wavefield is initiated at the point  $\vec{x}_0$  with source wavelet,

$$W(n) = w(n\delta t). \quad (3.20)$$

The source wavelet  $w(t)$  is typically taken to be a bandlimited minimum phase or

zero phase wavelet. The equation for source initiation is,

$$\begin{aligned} U^0(\vec{x}) &= 0, \\ U^1(\vec{x}) &= W(1)\delta(\vec{x}_0), \\ U^{n+1}(\vec{x}) &= -U^{n-1}(\vec{x}) + 2\mathcal{F}_{\vec{k} \rightarrow \vec{x}}^{-1}[\cos(2\pi v|\vec{k}|)\delta t]\mathcal{F}_{\vec{x} \rightarrow \vec{k}}[U^n(\vec{x})] + W(n+1)\delta(\vec{x} - \vec{x}_0), \end{aligned} \quad (3.21)$$

where  $\delta(\vec{x})$  is the Dirac delta function.

### 3.5 Aliasing and stability analysis

Equation (3.16) is an exact solution of the constant-velocity wave equation. The size of time step for equation (3.16) is limited by aliasing considerations. Equation (3.16) takes snapshots of the wavefield at two distinct times with spatial sampling rate  $\delta x$  and generates a new wavefield snapshot at a future time. The maximum wavenumber is,

$$(k_x, k_y, k_z) = \left( \pm \frac{\pi}{\delta x}, \pm \frac{\pi}{\delta x}, \pm \frac{\pi}{\delta x} \right), \quad (3.22)$$

which are called the Nyquist wavenumbers. By the dispersion relation, the maximum wavenumber generates a frequency  $\omega = \pi v \sqrt{3}/\delta x$ . Since the wavefield is sampled in time at rate  $\delta t$ , the Nyquist frequency is  $\omega = \pi/\delta t$ . Thus  $r = \delta t v / \delta x$  must satisfy the inequality  $r < 1/\sqrt{3}$  to avoid aliasing in three spatial dimensions.

A similar inequality must be satisfied by FD solvers depending on the order of convergence. Additionally, for low-order FD solvers, there must be 10 samples per wave length to propagate with a low amount of dispersion rather than the 2 samples per wave length needed for solving equation (3.16). Figure 3.2 shows how aliasing starts at  $r = 1/\sqrt{2}$  in the case of two spatial dimensions.

### 3.6 Pseudospectral methods

Pseudospectral methods (Boyd, 1989) with Fourier bases are widely used for modeling and migration. Pseudospectral methods are compared for accuracy and stability in the case of a constant velocity medium with equation (3.17). Fourier pseudospectral methods calculate the Laplacian of the wavefield in the wavenumber domain. The second-time derivative is approximated by the second-order centered FD operator to derive a time-marching algorithm,

$$U^{n+1} = 2U^n - U^{n-1} - \delta t^2 v^2 \mathcal{F}_{\vec{k} \rightarrow \vec{x}}^{-1}[(2\pi|\vec{k}|)^2 \mathcal{F}_{\vec{x} \rightarrow \vec{k}}[U^n]], \quad (3.23)$$

where the superscript  $n$  refer to the approximation at time step  $n$ . To deduce a higher-order algorithm, a higher-order FD approximation can be considered for the

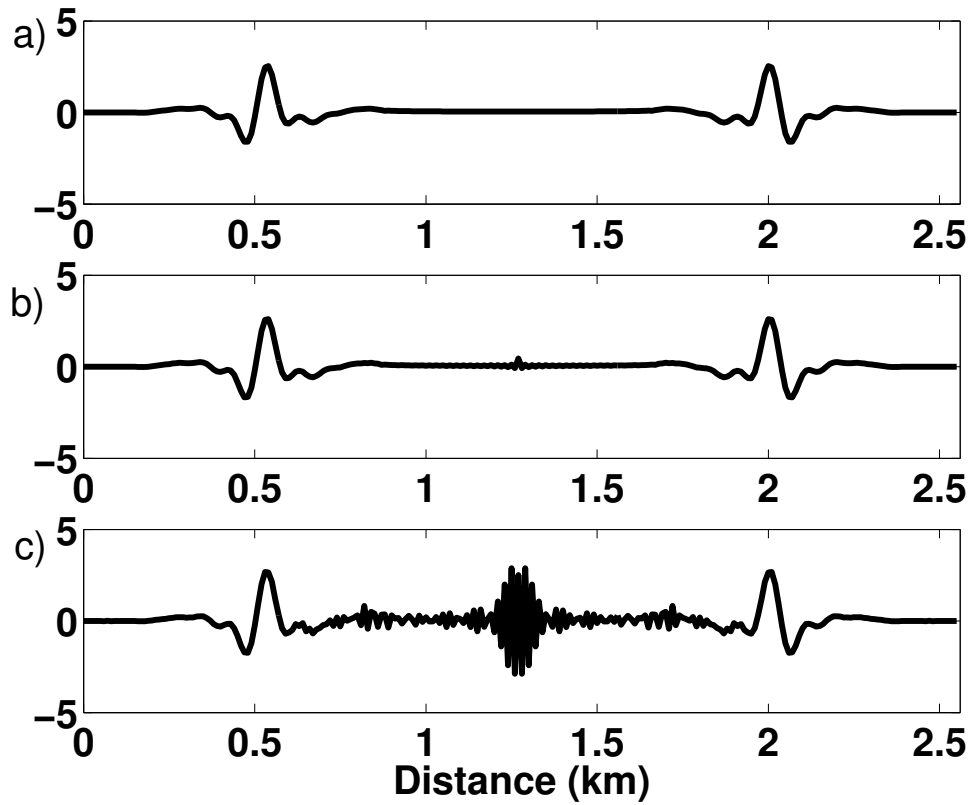


Figure 3.2: The center trace of the response to zero phase wavelet injected at the center of a constant velocity model with two spatial dimensions. The wave equation is solved for various values of the Courant number  $r$ . When  $r > \sqrt{0.5}$  aliasing occurs in the model. From top to bottom  $r = 0.68 \leq 0.71$ ,  $r = 1.00 \not\leq 0.71$ , and  $r = 1.5 \not\leq 0.71$ , respectively. The grid-spacing was taken to be a constant, 10m, and the time step was varied for the constant velocity,  $v = 2500m/s$ . The maximum frequency in the wavelet was 35Hz.

second-time derivative of  $U$ . However, higher-order in time schemes are unconditionally unstable (Cohen, 2001). The modified equation approach or the Lax-Wendroff method (Cohen, 2001) can be used to obtain a higher-order algorithm that is stable. The Taylor series expansion of the second time derivative is,

$$\frac{\partial^2 U^n}{\partial t^2} = \frac{U^{n+1} - 2U^n + U^{n-1}}{\delta t^2} - \frac{\delta t^2}{12} \frac{\partial^4 U^n}{\partial t^4} + O(\delta t^6), \quad (3.24)$$

which is derived by adding together the Taylor series expansion of  $U(t + \delta t)$  and  $U(t - \delta t)$  about  $t$ . The wave equation can be used to approximate the higher-order time derivatives, e.g.,

$$\begin{aligned} \frac{\partial^4 U}{\partial t^4} &= \frac{\partial^2}{\partial t^2} (v^2(\vec{x}) \Delta U) \\ &= (v^2(\vec{x}) \Delta (v^2(\vec{x}) \Delta U)) \\ &\simeq v^4(\vec{x}) \Delta (\Delta U). \end{aligned} \quad (3.25)$$

Substituting equation (3.24) into the acoustic wave equation gives the fourth-order in time approximation,

$$U^{n+1} = \delta t^2 v^2(\vec{x}) \Delta U^n - U^{n-1} + 2U^n + \frac{v^4(\vec{x}) \delta t^4}{12} \Delta^2 U^n + O(\delta t^6), \quad (3.26)$$

where  $\Delta U$  refers to the Laplacian of the function  $U$  and  $\Delta^q U$  is the Laplacian applied  $q$  times. If a higher-order expansion in equation (3.26) is used then formally (Etgen and Dellinger, 1989; Dablain, 1986; Chen, 2007),

$$U^{n+1} = -U^{n-1} + 2 \sum_{q=0}^{\infty} \frac{(\delta t v(\vec{x}))^{2q}}{(2q)!} \Delta^q U^n. \quad (3.27)$$

Calculating the Laplaican in the wavenumber domain and bringing the summation through the integral gives,

$$\begin{aligned} U^{n+1} &= -U^{n-1} + 2 \sum_{q=0}^{\infty} \frac{(\delta t v(\vec{x}))^{2q}}{(2q)!} \mathcal{F}_{\vec{k} \rightarrow \vec{x}}^{-1} \left[ (-1)^q (2\pi |\vec{k}|)^{2q} \hat{U}^n \right] \\ &= -U^{n-1} + 2 \mathcal{F}_{\vec{k} \rightarrow \vec{x}}^{-1} \left[ \sum_{q=0}^{\infty} \frac{(-1)^q (2\pi |\vec{k}| \delta t v(\vec{x}))^{2q}}{(2q)!} \hat{U}^n \right] \\ &= -U^{n-1} + 2 \mathcal{F}_{\vec{k} \rightarrow \vec{x}}^{-1} \left[ \cos(2\pi v(\vec{x}) |\vec{k}| \delta t) \hat{U}^n \right]. \end{aligned} \quad (3.28)$$

The inverse Fourier transform is now operating on a function that depends on  $\vec{x}$  and  $\vec{k}$  so it is now a Fourier-like integral and cannot be simply approximated with a FFT.

In the case when the velocity depends on the spatial coordinates,  $v(\vec{x})$ , the modified approach needs to be adjusted to insure convergence (Cohen, 2001). Substituting the variable velocity wave equation into the fourth-order in time derivative gives,

$$\frac{\partial^4 U}{\partial t^4} = v^4 \Delta^2 U + v^2 \Delta(v^2) \Delta U + v^2 \nabla(v^2) \cdot \nabla(\Delta U), \quad (3.29)$$

where  $\Delta v$  is the Laplacian applied to the velocity  $v$  and  $\nabla$  is the gradient operator. For variable velocity, because of the chain rule, equation (3.26) becomes,

$$\begin{aligned} U^{n+1} = & \delta t^2 v^2 \Delta U^n - U^{n-1} + 2U^n \\ & + \frac{\delta t^4}{12} (v^4 \Delta^2 U^n + v^2 \Delta(v^2) \Delta U^n + v^2 \nabla(v^2) \cdot \nabla(\Delta U^n)). \end{aligned} \quad (3.30)$$

A fourth-order in time solution of the variable velocity wave equation is then,

$$\begin{aligned} U^{n+1} = & -U^{n-1} + 2U^n - \left( \delta t^2 v^2 + \frac{\delta t^4 v^2 \Delta(v^2)}{12} \right) \mathcal{F}_{\vec{k} \rightarrow \vec{x}}^{-1} \left[ (2\pi|\vec{k}|)^2 \mathcal{F}_{\vec{x} \rightarrow \vec{k}}[U^n] \right] \\ & + \frac{\delta t^4}{12} (v^4) \mathcal{F}_{\vec{k} \rightarrow \vec{x}}^{-1} \left[ (2\pi|\vec{k}|)^4 \mathcal{F}_{\vec{x} \rightarrow \vec{k}}[U^n] \right] \\ & + \frac{\delta t^4}{12} (v^2) \nabla(v^2) \cdot \mathcal{F}_{\vec{k} \rightarrow \vec{x}}^{-1} \left[ 2\pi \vec{k} (2\pi|\vec{k}|)^2 \mathcal{F}_{\vec{x} \rightarrow \vec{k}}[U^n] \right]. \end{aligned} \quad (3.31)$$

When the velocity varies slowly or when we propagate the wavefields with smoothed background velocity the term involving  $\Delta v^2$  and  $\nabla v^2$  can be ignored. The solution is infinite order in space (Boyd, 1989). An infinite order solution converges faster than any finite-order approximation. In numerical simulations, the correction term for variable velocity in equation (3.31) shows no advantage over equation (3.28).

### 3.7 PSTS for variable velocity

We first provide an alternative derivation for a solution to the variable velocity wave equation. We then derive efficient computational schemes for its solution. The variable velocity acoustic wave equation is,

$$\frac{\partial^2 U}{\partial t^2} = v^2(\vec{x}) \left( \frac{\partial^2 U}{\partial x^2} + \frac{\partial^2 U}{\partial y^2} + \frac{\partial^2 U}{\partial z^2} \right). \quad (3.32)$$

Equation (3.28) is an approximate solution to the variable velocity acoustic that is more accurate than FD methods or pseudospectral methods. Wave equations have a causality property which means that the wavefield  $U(t, \vec{x})$  only depends on the wavefield locally. As a result, the right hand side of equation (3.32),

$$v^2(\vec{x}) (U_{xx} + U_{yy} + U_{zz}),$$

can, for small enough  $\delta t$ , be approximated locally near  $\vec{x}_0$  by the solution to the frozen term

$$v^2(\vec{x}_0) (U_{xx} + U_{yy} + U_{zz}).$$

This means that by replacing the constant velocity appearing in the dispersion relation in equation (3.16) by the variable velocity (i.e. unfreezing the velocity), we have an approximate solution,

$$U^{n+1}(\vec{x}) = -U^{n-1}(\vec{x}) + 2\mathcal{F}_{\vec{k} \rightarrow \vec{x}}^{-1} \left[ \cos \left( 2\pi v(\vec{x}) |\vec{k}| \delta t \right) \mathcal{F}_{\vec{x} \rightarrow \vec{k}} [U^n(\vec{x})] \right]. \quad (3.33)$$

Or explicitly,

$$\begin{aligned} U^{n+1}(\vec{x}) = & -U^{n-1}(\vec{x}) \\ & + 2 \int_{\mathbb{R}^3} \int_{\mathbb{R}^3} U^n(\vec{y}) \cos \left( 2\pi v(\vec{x}) |\vec{k}| \delta t \right) e^{2\pi i (\vec{y} - \vec{x}) \cdot \vec{k}} d\vec{y} d\vec{k}. \end{aligned} \quad (3.34)$$

This is the freezing-unfreezing argument that appears in the literature in the context of hyperbolic and elliptic partial differential equations e.g., (p. 230-231, Stein, 1993). Such solutions are often called locally homogeneous approximations (e.g., Ma and Margrave, 2008) and they approximate the solution to the variable velocity wave equation by the solution locally from the constant velocity wave equation. In fact, the local homogenous approximation is used for both FD and pseudospectral solvers.

Equation (3.33), for variable velocity, is too numerically complex to be used directly for wavefield propagation because the integrations cannot be accomplished with fast Fourier transforms (FFT's). We use a Gabor windowing scheme to approximate it, and so the resulting operator is a Gabor multiplier. The Gabor transform is a windowed Fourier transform. Equation (3.33) is a Fourier integral operator (Stein, 1993). Numerical computation of these operators is an active area of research (Candès et al., 2007). Please refer to Appendix A for various definitions of terms that occur in this section.

A partition of unity (POU, see again Appendix A) can be used to approximate equation (3.33). Suppose that a set of reference velocities have been chosen so that,

$$v_1 < \dots < v_j < \dots < v_N, \quad (3.35)$$

where  $v_1$  and  $v_N$  are the minimum velocity and maximum velocity of  $v(\vec{x})$ , respectively. Suppose  $\sum_j \Omega_j(\vec{x}) v_j^2 = v^2(\vec{x})$  and  $\sum_j \Omega_j(\vec{x}) = 1$  with  $0 \leq \Omega_j(\vec{x}) \leq 1$ . The auxiliary condition that  $\Omega_j(\vec{x}) = 0$  if  $v(\vec{x}) > v_{j+1}$  or  $v(\vec{x}) < v_{j-1}$  so that the operator is interpolated between the closest reference velocities. The  $\Omega_j$ 's window and interpolate the wavefield propagated with constant velocities. The windows also form a partition of unity that is they sum to unity. The set of windows that satisfy the

above conditions and provide a high-order solution of the wave equation is (Etgen and Brandsberg-Dahl, 2009),

$$\Omega_j(\vec{x}) = \begin{cases} \frac{v^2(\vec{x}) - v_{j-1}^2}{v_j^2 - v_{j-1}^2} & \text{if } v_{j-1} < v(\vec{x}) < v_j \\ \frac{v_{j+1}^2 - v^2(\vec{x})}{v_{j+1}^2 - v_j^2} & \text{if } v_j < v(\vec{x}) < v_{j+1} \\ 0 & \text{otherwise} \end{cases}. \quad (3.36)$$

To approximate equation (3.33) for quick numerical evaluation, we propagate the wavefield with a collection of constant velocities and then recombine the result with the partition of unity. Figure 3.3 is an image of the  $\Omega_j$  windows corresponding to four reference velocities of the Marmousi dataset (Versteeg, 1994).

In our method these regions can be spatially very complex when the velocity varies rapidly. The wavefield in each region is then propagated with the corresponding reference velocity. Figure 3.3 is an example of a velocity partition, or set of windows, which are used to migrate the Marmousi data set. The velocity partition is used to window the wavefield into regions at each time step. The combination of windowing and Fourier transformation results in the Gabor approximation to equation (3.33) given by,

$$U^{n+1}(\vec{x}) = -U^{n-1}(\vec{x}) + \sum_{j=1}^N \Omega_j(\vec{x}) 2\mathcal{F}_{\vec{k} \rightarrow \vec{x}}^{-1} \left[ \cos \left( 2\pi v_j |\vec{k}| \delta t \right) \mathcal{F}_{\vec{x} \rightarrow \vec{k}} [U^n(\vec{x})] \right], \quad (3.37)$$

where  $v_j$  is the reference velocity used for propagation in the  $j$ th window  $\Omega_j(\vec{x})$  and the integrations are now all FFT's.

It is possible to write equation (3.37) more explicitly as a Gabor multiplier. If  $\gamma_j = \Omega_j$ ,  $g_j = 1$ , and the Gabor multiplier  $M_j(\vec{k}) = 2 \cos(2\pi v_j |\vec{k}| \delta t)$ , then

$$\begin{aligned} U^{n+1}(\vec{x}) &= -U^{n-1}(\vec{x}) + \sum_{j=1}^N \gamma_j \mathcal{F}_{\vec{k} \rightarrow \vec{x}}^{-1} \left[ M_j(\vec{k}) \mathcal{F}_{\vec{x} \rightarrow \vec{k}} [g_j U^n(\vec{x})] \right], \\ &= -U^{n-1}(\vec{x}) + \sum_{j=1}^N V_{\gamma_j}^{-1} \left[ M_j V_{g_j} [U^n(\vec{x})] \right], \end{aligned} \quad (3.38)$$

where  $V_{g_j}[U^n(\vec{x})](\vec{k})$  is the forward Gabor transform (as defined in Appendix A) applied to the function  $U^n(\vec{x})$  and  $V_{\gamma_j}^{-1}$  is the inverse Gabor transform.

Equation (3.33) can be computed efficiently because at each time step two three-dimensional FFTs are computed. This means the computational burden is proportional to  $n_x n_y n_z \log(n_x n_y n_z)$  where  $n_x, n_y, n_z$  are the number of points used to discretize the  $x, y, z$  variable, respectively. For variable velocity, equation 3.37 is used with a computational burden proportional to  $n_v n_x n_y n_z \log(n_x n_y n_z)$  where  $n_v$  is the

number of reference velocities. For equation (3.33) the FFT cannot be used so that the computational burden at each time step is proportional to  $n_z^2 n_y^2 n_x^2$ . For PSTS the grid-spacing and time-step length can be made larger as compared to low-order FD methods. Higher-order pseudospectral methods require a slightly smaller time-step size than PSTS because the time derivative is approximated. More importantly, as compared to low-order FD methods, the more accurate calculation of a single iteration allows a larger time-step and grid-size.

The second-order in time pseudospectral method is derived formally from equation (3.28) by replacing the cosine function by its second-order power series expansion. Thus equation (3.28) generalizes the Fourier pseudospectral method, and therefore, FD schemes as well and, for homogeneous media, is superior.

Equation (3.28) can be used as an acoustic wave equation solver. However, it is computationally expensive to compute the integral. Instead, it is desirable to find a sum of functions of  $\vec{x}$  and  $\vec{k}$  separately that approximate  $\cos(2\pi v(\vec{x})|k|\delta t)$ . Soubaras and Zhang (2008) used an equiripple polynomial to approximate  $\cos(2\pi v|k|\delta t)$  instead of a Taylor series approximation, which are used to derive the higher-order pseudospectral method. Etgen and Brandsberg-Dahl (2009) approximate equation (3.28) by interpolating between two cosine propagators,

$$\begin{aligned} U^{n+1}(\vec{x}) = -U^{n-1}(\vec{x}) &+ 2 \frac{v_H^2 - v^2(\vec{x})}{v_H^2 - v_L^2} \mathcal{F}_{\vec{k} \rightarrow \vec{x}}^{-1} \left[ \cos(2\pi v_L|k|\delta t) \hat{U}^n(\vec{x}) \right] \\ &+ 2 \frac{v^2(\vec{x}) - v_L^2}{v_H^2 - v_L^2} \mathcal{F}_{\vec{k} \rightarrow \vec{x}}^{-1} \left[ \cos(2\pi v_H|k|\delta t) \hat{U}^n(\vec{x}) \right], \end{aligned} \quad (3.39)$$

where  $v_L$  is the minimum velocity and  $v_H$  is the maximum velocity. When the cosines are expanded with a Taylor series expansion, the method is at least as accurate as a second-order in time pseudospectral method. Tal-Ezer (1986) expands the cosine with orthogonal systems of Chebyshev polynomials, and Bessel functions and proves it is the polynomial basis that approximate the cosine function with the least number of terms.

The computational burden of the PSTS equation depends linearly on the number of reference velocities used to approximate the cosine operator. Constructing accurate approximations with a minimal number of reference velocities allows numerically efficient phase-shift time-stepping algorithms. Methods for choosing reference velocities are found in, for example, Bagaini et al. (1995) or Ma and Margrave (2008). A simple method is to take the reference velocities equally spaced between the lowest and greatest velocity.

Expanding the cosines in equation (3.33) with the power series expansion about  $v = 0$  shows that equation (3.33) is at least as accurate as a second-order pseudospectral method. This is the reverse step that was done to derive equation (3.28).

Figure 3.4 shows the percent error when calculating the variable velocity cosine operator. Interpolation occurs between two or more reference velocities. Reducing the time step has the greatest effect in reducing operator interpolation error. The blue line shows the error from interpolation in the square of the velocity which has a much smaller error than using linear interpolation in the velocity, as is shown by the green line. The red line shows the error from cutting the time step in half which is considerably lower than the error shown with the full time step by the blue line.

### 3.8 Split-step time stepping

A Taylor series can be used to approximate the variable velocity cosine operator about the reference velocity  $v_0$ . For some velocity functions this neighborhood can be extended to the entire domain of computation if a small error in the velocity is acceptable. The series expansion about the point  $v_0$  with the variation  $\delta v = v(\vec{x}) - v_0$  for the function  $\cos(2\pi v(\vec{x})|\vec{k}|\Delta t)$  is,

$$\begin{aligned}\cos(2\pi v(\vec{x})|\vec{k}|\Delta t) &= \cos(2\pi v(\vec{x}_0)|\vec{k}|\delta t) \\ &- \sin(2\pi v(\vec{x}_0)|\vec{k}|\delta t)\delta v(\vec{x})2\pi|\vec{k}|\Delta t \\ &- \frac{1}{2}\cos(2\pi v(\vec{x}_0)|\vec{k}|\delta t)\left[\delta v(\vec{x})2\pi|\vec{k}|\Delta t\right]^2 \\ &+ H.O.T.\end{aligned}\quad (3.40)$$

where H.O.T. denotes higher order terms. Substituting the Taylor series expansion (3.40) into equation (3.33) gives the second order split step correction,

$$\begin{aligned}U^n(\vec{x}) &\simeq -U^{n-1}(\vec{x}) + 2\mathcal{F}_{\vec{k} \rightarrow \vec{x}}^{-1} \left[ \cos(2\pi v(\vec{x}_0)|\vec{k}|\delta t)\widehat{U}^n \right] \\ &- 2\pi\delta v(\vec{x})\Delta t\mathcal{F}_{\vec{k} \rightarrow \vec{x}}^{-1} \left[ |\vec{k}| \sin \left( 2\pi v(\vec{x}_0)|\vec{k}|\delta t \right) \widehat{U}^n \right] \\ &- \frac{1}{2}(2\pi\delta v(\vec{x})\Delta t)^2\mathcal{F}_{\vec{k} \rightarrow \vec{x}}^{-1} \left[ |\vec{k}|^2 \cos(2\pi v(\vec{x}_0)|\vec{k}|\delta t)\widehat{U}^n \right].\end{aligned}\quad (3.41)$$

Higher-order algorithms can similarly be derived by taking a higher-order approximation in the Taylor series expansion in equation (3.40).

For large velocity variations  $\delta v$ , the split-step correction can become inaccurate and unstable. To eliminate this problem a windowed Fourier transform can be used with a number of reference velocities about which a smaller split-step correction is taken. For a set of velocities  $v_n$ , each  $\Omega_n$  window has a value of one if  $v(\vec{x})$  is close in value to  $v_n$ .

Within each window the wavefield is propagated with equation (3.41). At each time-step and the combination of windowing and Fourier transformation results in

the Gabor approximation to equation (3.16) given by,

$$U^n(\vec{x}) = -U^{n-1}(\vec{x}) + 2 \sum_{n=1}^N \Omega_n(\vec{x}) \mathcal{F}_{\vec{k} \rightarrow \vec{x}}^{-1} \left[ \cos \left( 2\pi v_n |\vec{k}| \delta t \right) \hat{U}^n \right], \quad (3.42)$$

where  $\Omega_n(\vec{x})$  is the windowing functions, and  $v_n$  is the reference velocity used for propagation in the  $n$ th window. Define the multiplier,

$$M_m^{v_n} = \begin{cases} (-1)^{m/2} (2\pi |\vec{k}| \delta t)^m \cos(2\pi v_n |\vec{k}| \delta t) & m \text{ even} \\ (-1)^{(m+1)/2} (2\pi |\vec{k}| \delta t)^m \sin(2\pi v_n |\vec{k}| \delta t) & m \text{ odd} \end{cases}. \quad (3.43)$$

So that the wavefield propagator for  $N$  windows of order  $M$  is,

$$U^n(\vec{x}) = -U^{n-1}(\vec{x}) + 2 \sum_{n=0}^N \Omega_n \sum_{m=0}^M \frac{(\delta v_n(\vec{x}))^m}{m!} \mathcal{F}_{\vec{k} \rightarrow \vec{x}}^{-1} \left[ M_m^{v_n} \hat{U}^n \right]. \quad (3.44)$$

### 3.9 Huygens's interpretation of the phase shift

### 3.10 PSTS with the derivative of the wavefield

The PSTS equation calculates the wavefield at  $U(t+\delta t, \vec{x})$  using the wavefields  $U(t, \vec{x})$  and  $U(t-\delta t, \vec{x})$ . It is also possible to use the derivative of the wavefield  $\partial U(t, \vec{x})/\partial t$  instead of the past wavefield  $U(t-\delta t, \vec{x})$ . This equation propagates the derivative of the wavefield and the wavefield forward in time. In doing so it does not suffer from a limitation on the time-step but requires twice as much computation and memory as the PSTS equation to compute one time-step. The time-step is limited by the need to window in the space domain which allows propagation with the local velocity and by the need to calculate the imaging condition at each spatial position of the waves. Prestack RTM requires frequent snapshots of the wavefield for the crosscorrelation imaging condition. Source and receiver fields need to be back-propagated, and therefore, the Nyquist frequency limits the time-step.

A solution to the constant velocity acoustic wave equation with initial conditions  $U(0, x, z) = f_0(x, z)$  and  $\partial U(0, x, z)/\partial t = f_1(x, z)$  is

$$\begin{aligned} U(t, \vec{x}) &= \int_{\mathbb{R}^2} \cos(\omega(k_x, k_z)t) \hat{f}_0(k_x, k_z) e^{2\pi i \vec{x} \cdot \vec{k}} dx dz \\ &\quad + \int_{\mathbb{R}^2} \sin(\omega(k_x, k_z)t) \frac{\hat{f}_1(k_x, k_z)}{\omega(k_x, k_z)} e^{2\pi i \vec{x} \cdot \vec{k}} dx dz, \end{aligned} \quad (3.45)$$

where  $\hat{f}_0, \hat{f}_1$  are the Fourier transform over the spatial coordinates  $(x, z)$  of  $f_0, f_1$ , respectively. The time derivative of the wavefield can be calculated at any time,

taking the derivative of both sides of equation 3.45,

$$\begin{aligned}\frac{\partial U}{\partial t}(t, x, z) &= - \int_{\mathbb{R}^2} 2\omega(k_x, k_z) \sin(\omega(k_x, k_z)t) \hat{f}_0(k_x, k_z) e^{2\pi i \vec{x} \cdot \vec{k}} dx dz \\ &\quad + \int_{\mathbb{R}^2} \cos(\omega(\vec{k})t) \hat{f}_1(\vec{k}) e^{2\pi i \vec{x} \cdot \vec{k}} dx dz.\end{aligned}\quad (3.46)$$

Unlike equation (3.33) which is governed by the stability condition,

$$\frac{v_{max} \Delta x}{\Delta t} < \frac{1}{\sqrt{2}}, \quad (3.47)$$

equations (3.45) and (3.46) are stable for any size time step. Thus a much great time step size can be taken. However, depending on the need for intermediate snap shots for crosscorrelation and the additional cost because of the additional storage fields and FFTs

Collecting the equations above, a time step is accomplished by,

$$\left. \begin{aligned}U(\Delta t + t, \vec{x}) &= \mathcal{F}_{\vec{k} \rightarrow \vec{x}}^{-1} \left[ \cos(\omega(\vec{k})\Delta t) \hat{U}(t, \vec{k}) \right] \\ &\quad + \mathcal{F}_{\vec{k} \rightarrow \vec{x}}^{-1} \left[ \frac{\sin(\omega(\vec{k})\Delta t)}{\omega(\vec{k})} \frac{\partial \hat{U}}{\partial t}(t, \vec{k}) \right] \\ \frac{\partial U}{\partial t}(\Delta t + t, \vec{x}) &= -\mathcal{F}_{\vec{k} \rightarrow \vec{x}}^{-1} \left[ \omega(\vec{k}) \sin(\omega(\vec{k})\Delta t) \hat{U}(t, \vec{k}) \right] \\ &\quad + \mathcal{F}_{\vec{k} \rightarrow \vec{x}}^{-1} \left[ \cos(\omega(\vec{k})\Delta t) \frac{\partial \hat{U}}{\partial t}(t, \vec{k}) \right]\end{aligned}\right\}. \quad (3.48)$$

Let  $V(t) = \frac{\partial U}{\partial t}(t)$  and define the operator,

$$\mathcal{K} = \begin{bmatrix} \mathcal{F}_{\vec{k} \rightarrow \vec{x}}^{-1} \cos(\omega(\vec{k})\Delta t) \mathcal{F}_{\vec{x} \rightarrow \vec{k}} & \mathcal{F}_{\vec{k} \rightarrow \vec{x}}^{-1} \frac{\sin(\omega(\vec{k})\Delta t)}{\omega(\vec{k})} \mathcal{F}_{\vec{x} \rightarrow \vec{k}} \\ -\mathcal{F}_{\vec{k} \rightarrow \vec{x}}^{-1} \omega(\vec{k}) \sin(\omega(\vec{k})\Delta t) \mathcal{F}_{\vec{x} \rightarrow \vec{k}} & \mathcal{F}_{\vec{k} \rightarrow \vec{x}}^{-1} \cos(\omega(\vec{k})\Delta t) \mathcal{F}_{\vec{x} \rightarrow \vec{k}} \end{bmatrix}. \quad (3.49)$$

Then equation (3.48) can be viewed more succinctly in matrix form as,

$$\begin{bmatrix} U(t) \\ V(t) \end{bmatrix} = \mathcal{K} \begin{bmatrix} U(0, \vec{x}) \\ V(0, \vec{x}) \end{bmatrix}, \quad (3.50)$$

or completely in the spatial wavenumber domain by letting the matrix,

$$K(\Delta t, \vec{k}) = \begin{bmatrix} \cos(\omega(\vec{k})\Delta t) & \frac{\sin(\omega(\vec{k})\Delta t)}{\omega(\vec{k})} \\ -\omega(\vec{k}) \sin(\omega(\vec{k})\Delta t) & \cos(\omega(\vec{k})\Delta t) \end{bmatrix}. \quad (3.51)$$

Then,

$$\begin{bmatrix} \hat{U}(t + \Delta t, \vec{k}) \\ \hat{V}(t + \Delta t, \vec{k}) \end{bmatrix} = K \begin{bmatrix} \hat{U}(0, \vec{k}) \\ \hat{V}(0, \vec{k}) \end{bmatrix}, \quad (3.52)$$

where the matrix  $K$  satisfies the functional relation  $K(\Delta t + \Delta s) = K(\Delta t)K(\Delta s)$ .

If the operator  $\mathcal{K}_n$  corresponds to  $\mathcal{K}$  in equation (3.49) with  $\omega = v_n|\vec{k}|$ . Then a time stepping solution for the wave equation is,

$$\begin{bmatrix} U(t + \Delta t, \vec{x}) \\ V(t + \Delta t, \vec{x}) \end{bmatrix} = \sum_{n=1}^N \mathcal{K}_n \begin{bmatrix} \Omega_n(\vec{x})U(t, \vec{x}) \\ \Omega_n(\vec{x})V(t, \vec{x}) \end{bmatrix}. \quad (3.53)$$

By replacing  $\Delta t$  with  $-\Delta t$  the operator  $\mathcal{K}(-\Delta t)$  in equation (3.53) can propagate backwards.

### 3.11 Multi-stepping in the wavenumber domain

Downward continuation wavefield propagation can take large depth steps because there is no stability or aliasing limit on the depth step size. However, aliasing in the imaging condition limits the depth-step size. Ng (2007) uses a time-shift imaging condition to generate intermediate downward propagated and upward propagated wavefield data between depth steps. The time-shift imaging condition uses a crude but cheap wavefield propagator to generate an image in between depth steps. The final pass of migration is done with a fine depth-step size, but a crude depth-step size can be used for velocity building.

For a constant velocity wavefield, it is possible to propagate a wavefield with equation (3.16) completely in the wavenumber domain without the need at each time step to change back into the space domain with a Fourier transform. This makes wavefield propagation exceptionally fast, through it only works in a highly idealized model. The time-step size is limited by the aliasing condition. For variable velocity, the wavefield must be transform back to the space domain for localization and interpolation. We demonstrate a method that takes multiple time steps in the wavenumber domain. These steps are taken in order to limit the number of Fourier transforms shuttling between space and wavenumber domains. However, increasing the time-step size in the wavenumber domain results in a blurring of the velocity field.

Rewriting equation (3.17) as a system in the wave number domain gives,

$$\begin{bmatrix} \widehat{U}(t + \Delta t) \\ \widehat{U}(t) \end{bmatrix} = \begin{bmatrix} 0 & 1 \\ -1 & 2 \cos(2\pi v|\vec{k}| \Delta t) \end{bmatrix} \begin{bmatrix} \widehat{U}(t) \\ \widehat{U}(t - \Delta t) \end{bmatrix}. \quad (3.54)$$

Taking  $m$  time steps in the wavenumber domain gives the wavefield at time  $t + m\Delta t$ ,

$$\begin{bmatrix} \widehat{U}(t + m\Delta t) \\ \widehat{U}(t + (m-1)\Delta t) \end{bmatrix} = \begin{bmatrix} 0 & 1 \\ -1 & 2 \cos(2\pi v|\vec{k}| \Delta t) \end{bmatrix}^m \begin{bmatrix} \widehat{U}(t) \\ \widehat{U}(t - \Delta t) \end{bmatrix}, \quad (3.55)$$

For a set of windowing functions  $\Omega_n$  and velocities  $v_n$  that approximate the velocity field  $v^2(\vec{x}) = \Omega_n$ . Let

$$H_n = \begin{bmatrix} 0 & 1 \\ -1 & C_n \end{bmatrix} \quad (3.56)$$

where  $C_n = 2\cos(2\pi|\vec{k}|v_n\Delta t)$ . One multi-time step is accomplished for a variable velocity medium by the approximation,

$$\begin{bmatrix} U(t + m\Delta t, \vec{x}) \\ U(t + (m-1)\Delta t, \vec{x}) \end{bmatrix} = \mathcal{F}_{\vec{k} \rightarrow \vec{x}}^{-1} \sum_{n=1}^N (H_n)^m \begin{bmatrix} \mathcal{F}_{\vec{x} \rightarrow \vec{k}}[\Omega_n(\vec{x})U(t, \vec{x})] \\ \mathcal{F}_{\vec{x} \rightarrow \vec{k}}[\Omega_n(\vec{x})U(t - \Delta t, \vec{x})] \end{bmatrix}, \quad (3.57)$$

where the inverse Fourier transform is applied to each component of the vector on which it operates on. The  $m$ -th power of the  $H_n$  matrix can be precomputed. For  $m = 3$ ,

$$(H_n)^3 = \begin{bmatrix} -C_n^2 & C_n^2 - 1 \\ C_n^2 - 1 & C_n^3 \end{bmatrix}. \quad (3.58)$$

Equation (3.57) takes  $2(N+1)$  2-D FFTs to compute the wavefield at time  $m\Delta t + t$  and  $(m-1)\Delta t + t$  or if the wavefield at times  $t, t + \Delta t, \dots, (m+1)\Delta t + t$  needs to be calculated, then it takes  $2N + m$  FFTs. For the Marmousi data set we used  $m = 6$  for the number of times we propagate in the wavenumber domain and  $N = 16$  for the number of windows used to construct the velocity partition. In contrast, one time step using equation (3.42) takes  $N + 1$  FFTs. Figure 3.5 shows that using  $m = 6$  cuts the calculation time in half. However, there is a significant degradation in quality of propagation when  $m$  is greater than 6.

Alternatively, those Gabor windows for which either the receiver field is being injected or the shot is being injected can be propagated by windowing and a Fourier transforming at each time step while the other windows are propagated with equation (3.57). To prevent aliasing and to insure the velocity field is accurately approximated the number of steps  $m$  is chosen to satisfy

$$mdt < \frac{1}{2f_{max}}, \quad (3.59)$$

where  $f_{max}$  is the maximum frequency in the seismic data.

### 3.12 One-way in time wavefield propagation

The one-way in depth wave equation was derived for depth continuation. The one-way in time wave equation (Zhang and Zhang, 2009),

$$\begin{aligned} \frac{\partial U}{\partial t} &= v\sqrt{-\Delta}U \\ &= v\mathcal{F}_{\vec{k} \rightarrow \vec{x}}^{-1} \left[ 2\pi i |\vec{k}| \widehat{U} \right] \end{aligned} \quad (3.60)$$

subject to the initial condition  $U(0) = U^0$  is a Fourier integral operator (see Appendix XX). It has an approximate solution,

$$U^{n+1} = \mathcal{F}_{\vec{k} \rightarrow \vec{x}}^{-1} [\exp(2\pi i v(\vec{x}) \delta t |\vec{k}|) \mathcal{F}_{\vec{x} \rightarrow \vec{k}} [U^n]]. \quad (3.61)$$

Expanding the exponential with a Taylor series expansion at zero or any reference velocity provides a numerical implementation. Alternatively, a discontinuous partition of unity can be used to approximate equation (3.61) similar to what was done to derive equation (3.37). In this case, it is more appropriate to choose the partition to satisfy  $\sum_j \Omega_j(\vec{x}) v_j = v(\vec{x})$  and so,

$$\Omega_j(\vec{x}) = \begin{cases} \frac{v(\vec{x}) - v_{j-1}}{v_j - v_{j-1}} & \text{if } v_{j-1} < v(x) < v_j \\ \frac{v_{j+1} - v(\vec{x})}{v_{j+1} - v_j} & \text{if } v_j < v(x) < v_{j+1} \\ 0 & \text{otherwise} \end{cases}. \quad (3.62)$$

To approximate equation (3.61), we propagate the wavefield with a collection of constant velocities and recombine the result with the POU,

$$U^{n+1}(\vec{x}) = \sum_{j=1}^J \Omega_j(\vec{x}) \mathcal{F}_{\vec{k} \rightarrow \vec{x}}^{-1} [\exp(2\pi v_j \delta t |\vec{k}|) \mathcal{F}_{\vec{x} \rightarrow \vec{k}} [U^n(\vec{x})]]. \quad (3.63)$$

Expanding the exponential functions in equation (3.63) and (3.61) with a second-order Taylor series shows that equation (3.63) is as accurate as second-order pseudospectral method. However, it does show significantly less dispersion.

### 3.13 Numerical examples

We compare a number of methods for wavefield propagation by looking at some snapshots of a forward propagated zero phase wavelet. The wavelet is injected at the center of a salt dome model which is a portion of the BP dataset in Figure 3.8(a). The wavelet is bandlimited from 5Hz to 50Hz. All of the comparisons were made on the same model with a grid-spacing of 12.5m. The BP data set contains a rugose salt dome embedded in background sediments whose velocity smoothly increases with depth. Figure 3.6(a), and (b) are snapshots propagated using second-order, and fourth-order pseudospectral method using equation (3.23), respectively. The lower-order method is computationally efficient but contains some dispersion while there is little dispersion in the higher order implementation. Figure 3.6(c) is the first order split-step correction derived in equation (3.40). The snapshot is not dispersive, but there are large kinematic errors due to the low order of the approximation. Figure

3.6(d) is the second order split-step correction. The kinematics are much better than in Figure 3.6(c).

Figure 3.7(a) is the snapshot propagated with a one-way time algorithm using a Law-Wendroff pseudospectral implementation of equation (3.61). The amplitudes are incorrect. Figure 3.7(b) is the snapshot propagated with a one-way time algorithm using equation (3.63) and has much better amplitudes. Figure 3.7(c) is the snapshot using a Law-Wendroff pseudospectral implementation of equation (A.19). The amplitudes are incorrect. Figure 3.7(d) is a snapshot of the wavefield using equation (3.53). The amplitudes are much better because there is less numerical dispersion, and a much larger time step was used.

Figure 3.8(b) is a snapshot of the wavefield propagated with equation (3.37) using 2 reference velocities. It has velocities errors when compared to the snapshot in Figure 3.8 computed using 4 reference velocities. Both have little dispersion. Table 3.1 contains the computational times and time-step sizes used to calculate the snapshots in the figures. The one-way in time algorithm is the fastest because it can be computed with a large time step.

| Algorithm                        | Relative Time | Time (ms)<br>Step | Grid-size<br>Spacing | Number<br>of FTT |
|----------------------------------|---------------|-------------------|----------------------|------------------|
| PSTS 10 vels                     | 5             | 1.5               | 12.5                 | 11               |
| PSTS 20 vels                     | 10            | 1.5               | 12.5                 | 21               |
| pseudo 2nd order                 | 0.8           | 1.2               | 12.5                 | 3                |
| pseudo 4th order                 | 1.0           | 1.5               | 12.5                 | 3                |
| $+\Delta(c^2)\Delta(U)$          | 1.0           | 1.5               | 12.5                 | 3                |
| splitstep 1st order              | 0.9           | 1.5               | 12.5                 | 3                |
| splitstep 2nd order              | 1.3           | 1.5               | 12.5                 | 4                |
| splitstep 1st order<br>3 windows | 4.5           | 1.5               | 12.5                 | 7                |

Table 3.1: Relative computation time and time-step size used in algorithms to generate Figure 3.6 and Figure 3.9

Due to their slow convergence, power series expansions of the one-way in time solution and the evolutionary wave equation solution used to derive Lax-Wendroff pseudospectral methods are inaccurate. A partition of unity and propagating with a constant velocity provide less dispersive solutions. The one-way equation had large amplitude errors. Using a partition of unity will provide a solution that has little dispersion but enough reference velocities must be chosen to minimize velocity errors. A power series expansion of the cosine equation is more accurate because of better

convergence properties.

### 3.14 Sampling issues

Ideally it would be desirable to time step at the Nyquist sampling rate of the seismic data,

$$\Delta t_{nyq} = \frac{1}{2f_{max}}, \quad (3.64)$$

where  $f_{max}$  is the maximum signal frequency. Reverse time migration methods however often require finer sampling. For the PSTS equation, the smallest wavelength must be sampled at least twice,

$$\Delta x < \frac{V_{min}}{2f_{max}}, \quad (3.65)$$

where  $V_{min}$  is the minimum velocity of the model and  $\delta x$  is the grid-spacing in the  $x$  and  $z$  directions. The time step must satisfy (Wards et al., 2007),

$$\delta t < \frac{\delta x}{\sqrt{2}V_{max}}. \quad (3.66)$$

For processing the seismic survey with  $[V_{min}, V_{max}] = [1500m/s, 5500m/s]$  and  $f_{max} = 50Hz$ , the sampling requirements are  $\delta x < 15m$ ,  $\delta t < 0.0015s$ , and  $t_{nyq} = 0.01s$ .

To minimize computation time, a multi-radix FFT is used. The computation domain is padded to the next integer with a large number of prime factors. A pad is necessary to prevent wraparound of the FFT and to enforce a free surface boundary condition.

We compare pseudospectral methods to split-step PSTS methods by looking at some snapshots at a particular time of a forward propagated wavelet through a portion of the BP data set in Figure 3.8(a). The wavelet is injected at the center of the model. The BP data set Billette and Brandsberg-Dahl (2005) contains a number of salt domes and is commonly used to test velocity picking algorithms, wide angle depth continuation algorithms, and reverse time migration algorithms. The BP data set contains a rigorous salt dome embedded in a background sediment whose velocity smoothly increasing with depth. Figure 3.6(a) is the snapshot using second-order pseudospectral method using equation (3.23). The method is computationally efficient but contains unacceptable dispersion. Figure 3.6(b) is the snapshot using fourth-order pseudospectral method using equation (3.23). There is no observable dispersion. Figure 3.6(c) is the first order split-step correction. Although the model does not contain much dispersion there are large kinematic errors due to the low order of the approximation. Figure 3.6(d) is the second order split-step correction. The

kinematics are much better than in Figure 3.6(c) but there is more dispersion than the fourth-order pseudospectral method. Figure 3.9(a) is the first-order split-step correction using three reference velocities. The kinematics are much improved over using one reference velocity. Figure 3.9(b) is the fourth order pseudospectral method with the correction term in equation (3.30). The correction term had little noticeable effect. Figure 3.9(d) is the PSTS approximation using 10 reference velocities. There are noticeable kinematic errors through there is little dispersion. Figure 3.9(d) use 20 reference velocities but does not significantly improve the poor image of Figure 3.9(c). Table 1 contains the relative computation times of all the methods. All of the computations where computed with the same grid-size. For a few methods, a smaller time step was used to ensure stability.

For a further application, a forward modeled shot using the second-order and fourth-order split-step PSTS equation and the fourth-order in time pseudospectral method are compared. An automatic gain control was applied to both shot records. Both fourth-order methods are of comparable quality. The second-order split-step PSTS method suffers from grid dispersion. This can be reduced by making the time step smaller. However it is numerically more efficient to use a higher-order method.

We presented a new method to approximate equation (3.33) which solves the acoustic wave equation. It is similar to higher-order in time pseudospectral methods based on the modified equation approach or the Lax-Wendroff method. This approximation scheme can be used for acoustic modeling or reverse-time migration. We also presented a windowing scheme where a lower-order approximation can be used around multiple reference velocities. However, due to the large number of fast Fourier transforms (FFTs) needed to execute the windowing scheme, it is much more computationally efficient to use a higher-order method.

### 3.15 Forward modeling example

For the modeling of reflections, the discontinuities in the velocity field are very important. Equation (3.37) is used as a modeling algorithm to test the ability of the PSTS equation to generate reflections. Figure 3.10 compares a FD approximation to the PSTS equation for forward modeling in a three layer medium using three reference velocities. The PSTS result is non-dispersive and compares well to the FD result. This suggests that there is potential either for modeling with PSTS and that certain multiple generating horizons can be included in RTM when using the PSTS equation.

### 3.16 Conclusion

We proposed a Fourier domain phase-shift equation for time-stepping a wavefield and called the resulting algorithm PSTS (phase-shift time-stepping). Our method multiplies the spatial Fourier transform of the wavefield by a cosine whose argument depends on velocity and wavenumber. The variable velocity PSTS equation is a Fourier integral operator whose direct computation is very slow. We presented a computationally feasible approximation to this operator using a spatial Gabor transform with windows that adapt to the velocity structure. The number of windows chosen, one for each *reference velocity*, directly controls the computational speed and must be minimized.

We demonstrated the potential to use PSTS for wave propagation. We showed that the PSTS equation is numerically efficient and has low dispersion. It compares well with a more conventional finite-difference result or pseudospectral methods. PSTS can use a larger time step and a coarser grid-size than a typical FD method and a similar time step as pseudospectral methods. We found the most effective time stepping solution is to interpolate the wavefield from two constant velocity time steppers with the maximum and minimum velocity.

We also derived alternative methods for wavefield propagation that use fewer Fourier transforms to calculate a time step or take a larger time step than Nyquist, but these methods suffer from low accuracy because they do not properly sample the velocity field.

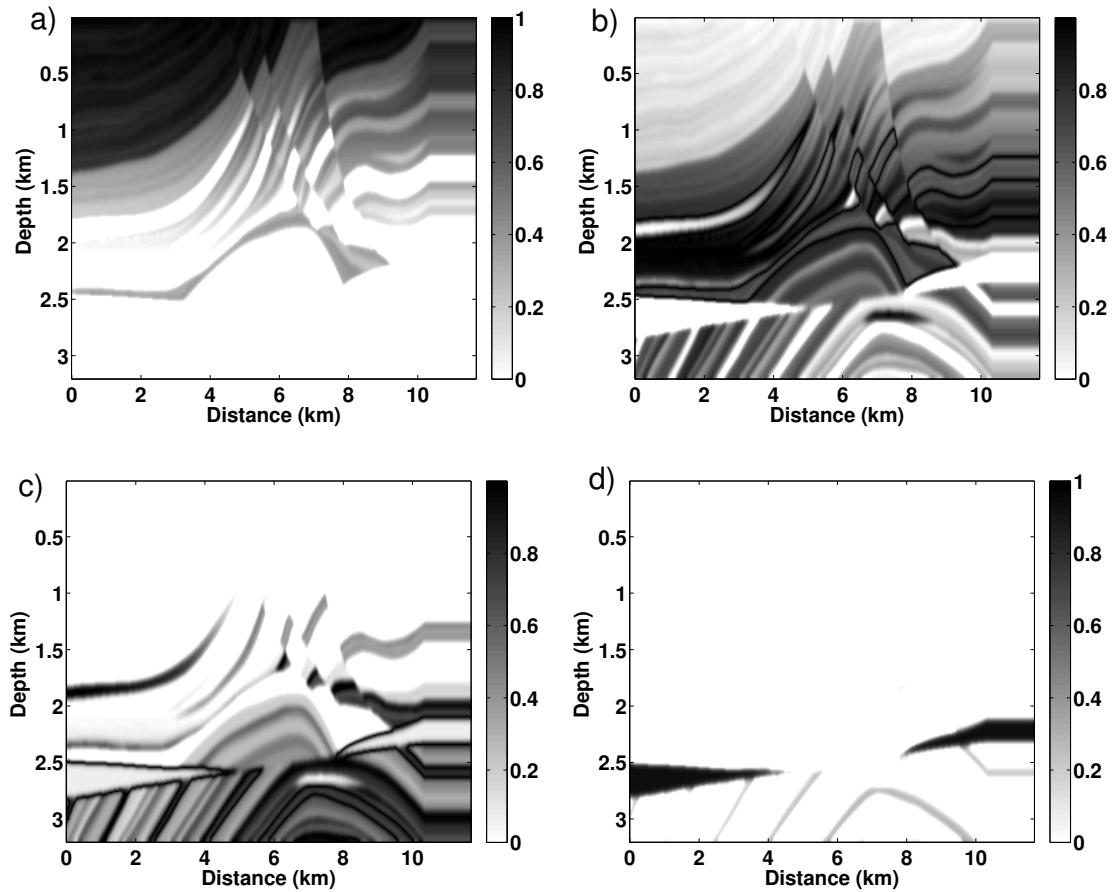


Figure 3.3: A set of windowing functions used to propagate the Marmousi dataset. (a),(b),(c),(d) corresponding to the velocities 1556, 2902, 4247, and 5593m/s, respectively.

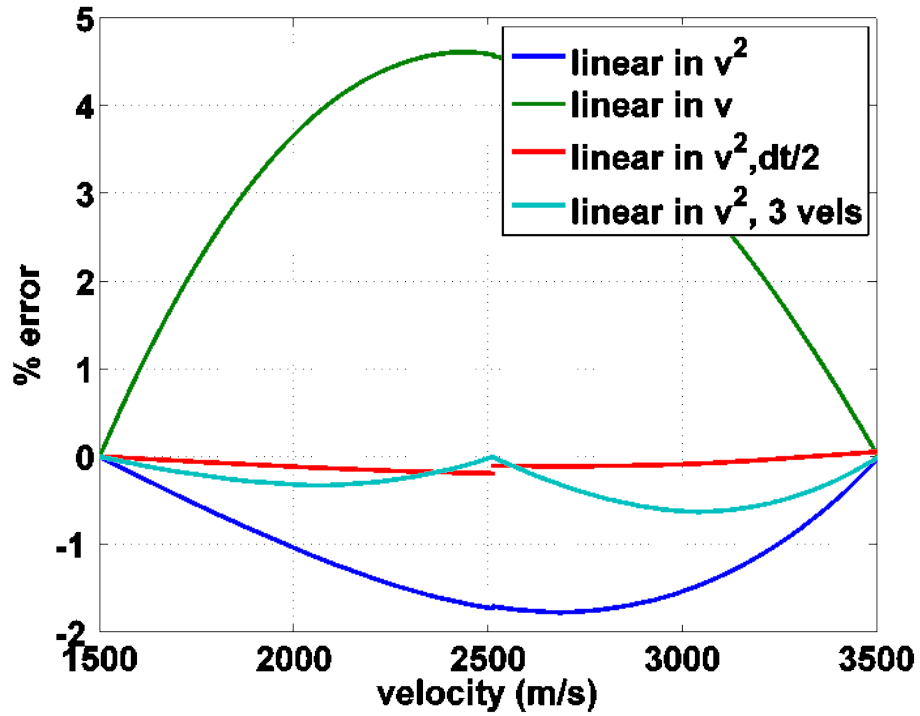


Figure 3.4: The Percent velocity error when using different kinds of interpolation schemes between constant velocity operators. The interpolation error can be decreased by using more reference velocities or by decreasing the size of the time step.

| $m$ | time (s) no intermediate calculations | accurate and stable |
|-----|---------------------------------------|---------------------|
| 0   | 128                                   | yes                 |
| 4   | 112                                   | yes                 |
| 6   | 88                                    | yes                 |
| 12  | 72                                    | yes                 |
| 20  | 63                                    | no                  |

Figure 3.5: Computation time for forward propagating a wavefield for various values of the speedup factor  $m$  using equation (3.57).

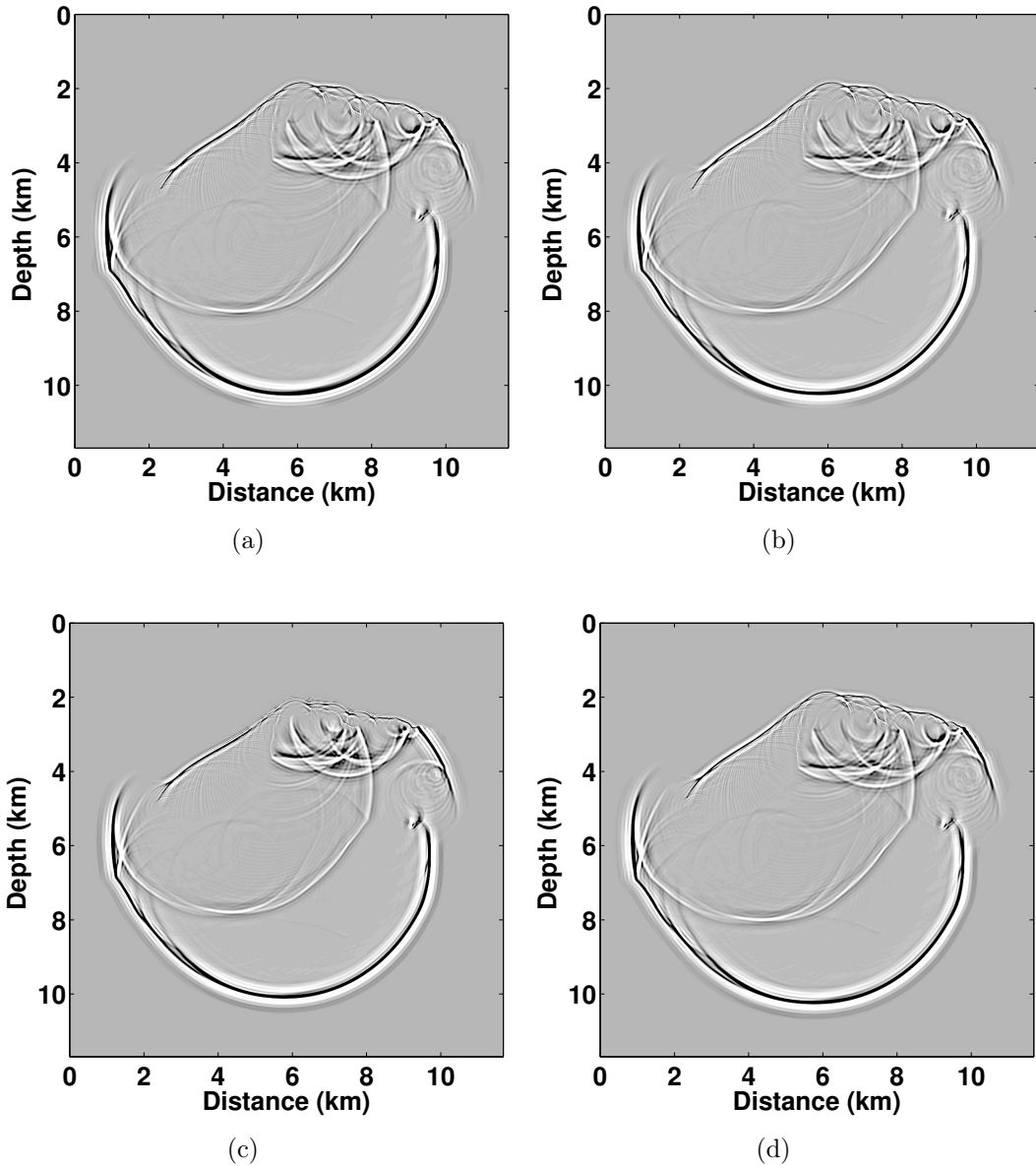


Figure 3.6: (a) A snapshot of a wavefield propagated with second-order pseudospectral method using equation (3.37). (b) A snapshot of a wavefield propagated with forth-order pseudospectral method using equation (3.23). (c) A snapshot of a wavefield propagated with first-order split-step correction with one correction term in equation (3.40). (d) A snapshot of a wavefield propagated with second-order split-step correction with two correction terms in equation (3.40).

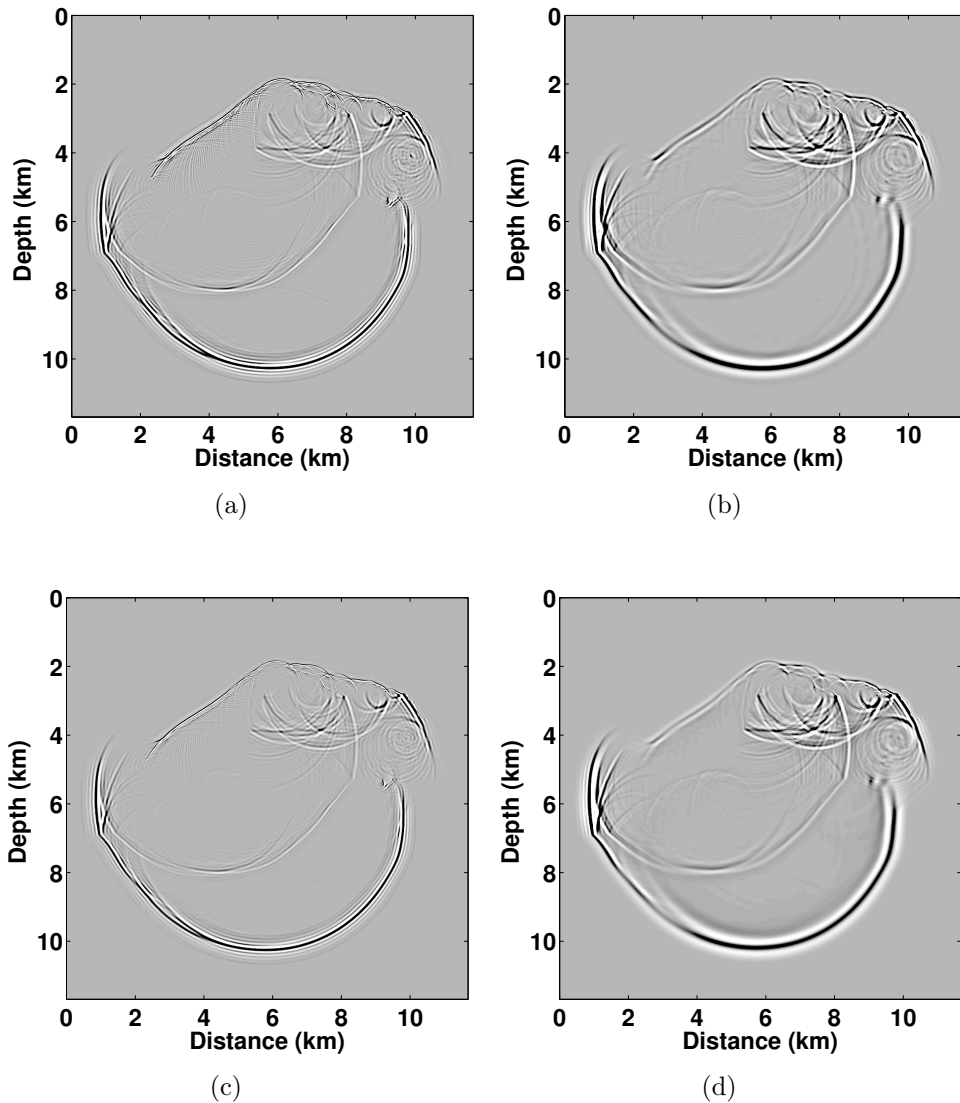
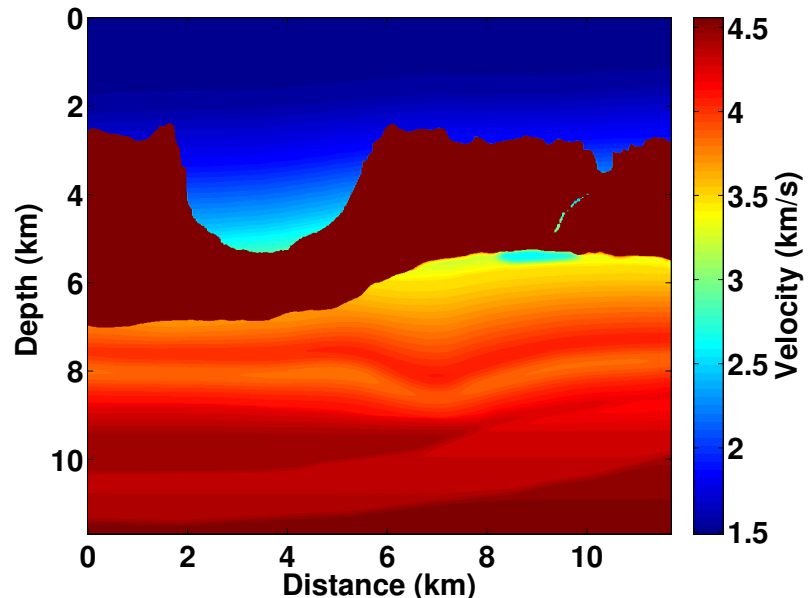
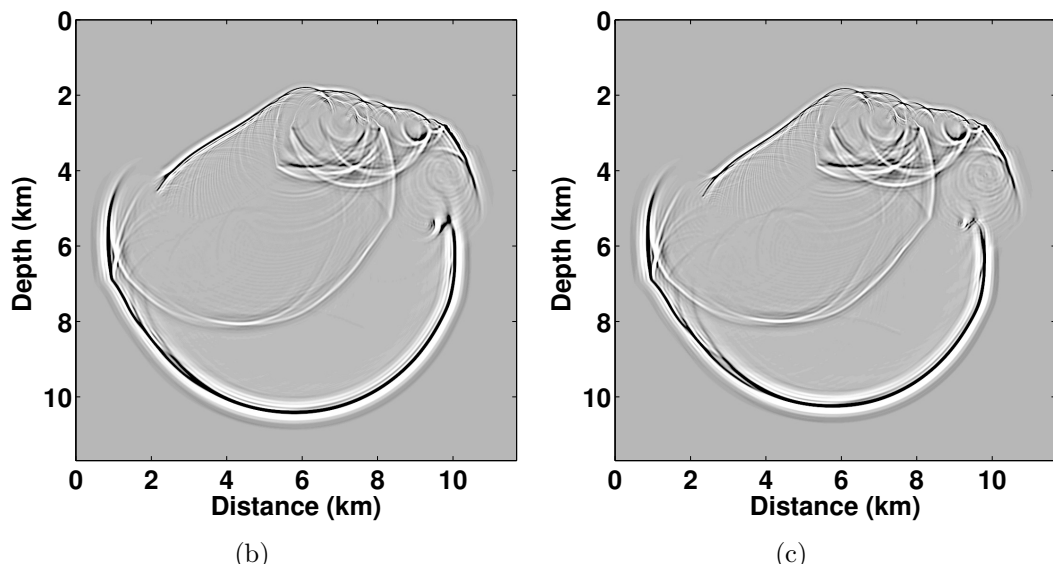


Figure 3.7: (a) A snapshot of a wavefield propagated with a one-way in time pseudospectral method. Five terms in the power series expansion of equation (3.61) with respect to  $v = 0$  were used. The time-step size is 5ms. (b) A snapshot of a wavefield propagated with a one-way in time wave equation approximated with a POU with three windows with a time step of 9ms derived in equation (3.63). (c) A snapshot of a wavefield propagated with a second order pseudospectral method applied to equation (A.19). (d) A three window POU applied to the evolutionary equation with a time step of 9ms using equation (3.53).



(a)



(b)

(c)

Figure 3.8: (a) A section of the BP data set showing the high velocity salt dome. (b) A snapshot of a wavefield propagated with equation (3.37) using a POU with two windows. (c) Same as (b) but using a 4 window POU.

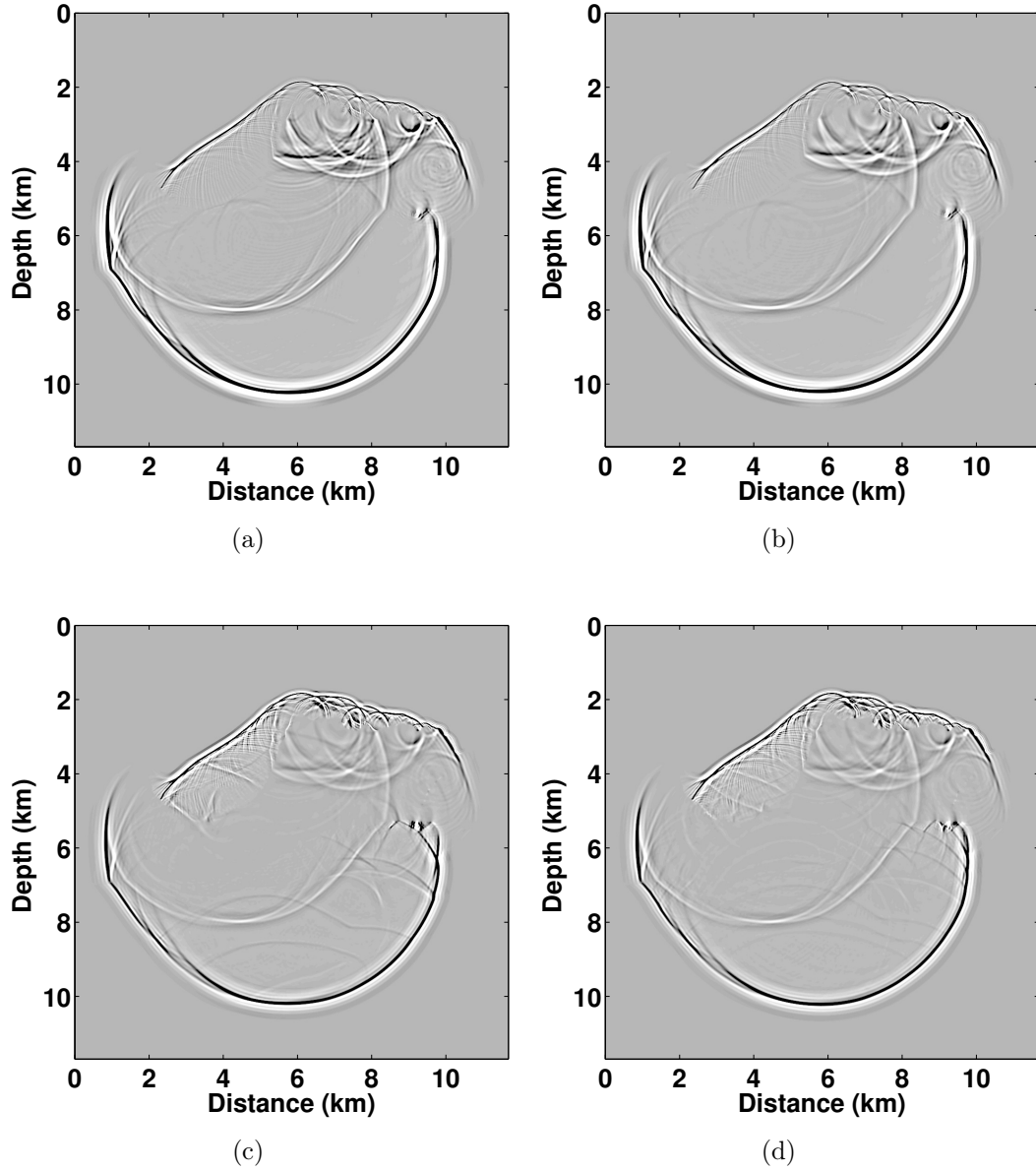


Figure 3.9: (a) A snapshot generated with a fourth-order pseudospectral method with correction term from equation 3.30. (b) First-order split-step PSTS with three windows. (c) The PSTS equation with no split-step correction using 10 evenly spaced reference velocities. (d) Same as (c) but 20 reference velocities were chosen.

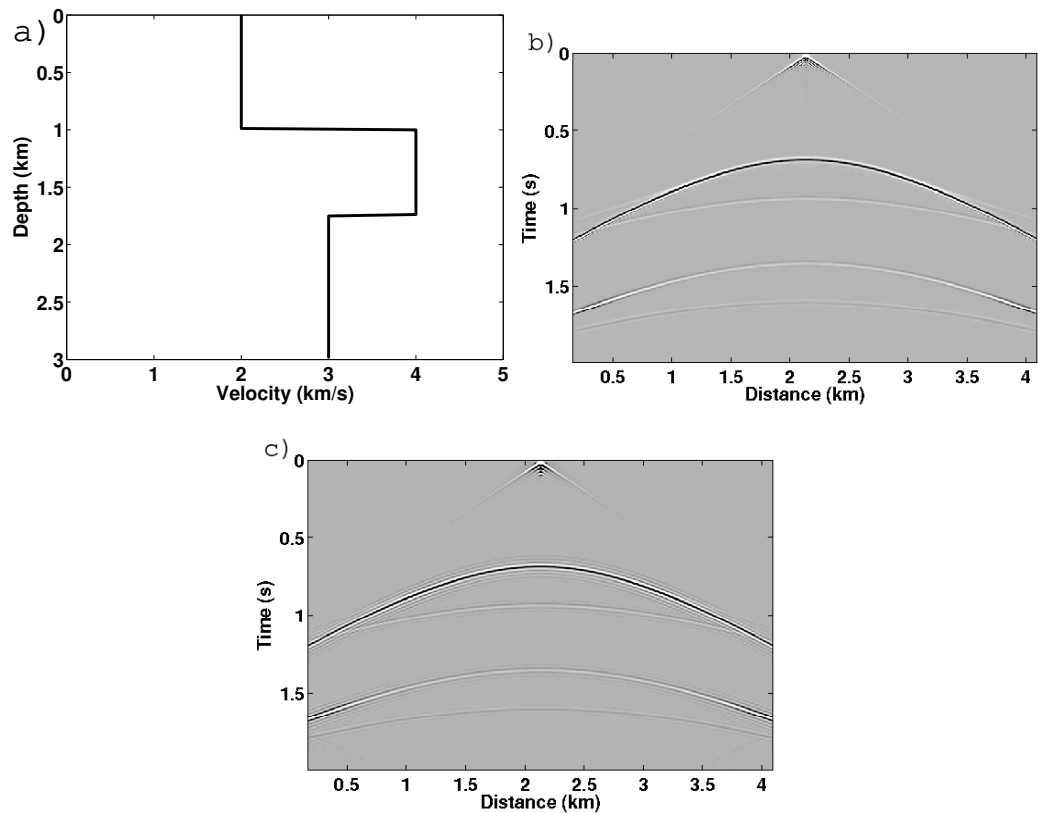


Figure 3.10: (a) Velocity profile for a 2-D three layer velocity model. (b) Shot record generated using the PSTS equation. (c) A Shot record generated using second-order time fourth-order in space FD solver.

# Chapter 4

## Wavefield propagation in anisotropic media

Almost all rocks in the earth's crust are anisotropic. To image structures in their true location and to bring them into focus with seismic methods requires migration and the processing flows to account for anisotropy. In this chapter, wavefield propagation in anisotropic media is developed. The speed of propagation in anisotropic media is sensitive to the direction of propagation. An efficient and accurate anisotropic wavefield propagator is an important part of forward modelling and TTI RTM. A full characterization of anisotropic wavefield propagation requires solving the elastic wave equation. This is costly because it requires solving a second-order system of linear PDEs.

An efficient and accurate acoustic wave equation solver is an important tool for modeling and migration. However, it does not model all the behavior of sound waves traveling in the earth like mode conversion between P and S-waves and anisotropy. The elastic wave equation models both mode conversions and anisotropy through it does not model attenuation. The elastic wave equation solvers are computationally expensive as the displacement has three components and the slow interface waves must have fine time and spatial sampling otherwise they are unstable. As well, elastic migration and modelling requires all 21-components of the elastic stiffness tensor which are difficult to estimate. Pseudo-acoustic wave equations are acoustic-like scalar wave equations that have the kinematic behavior of the elastic wave equation, like wave speed anisotropy, but are not as computationally expensive to solve. P-wave propagation can also be done without knowing all of the S-wave velocities.

In this chapter, pseudo-acoustic wave equations for modeling P and S are derived as well as numerical schemes for solving them. Pseudo-acoustic wavefield propagation for anisotropic media is challenging. Extensive work has been done to improve stability, accuracy and efficiency of computation of pseudo-acoustic propagators. The dispersion relation of the elastic wave equation determines the speed of propagation of the body wave modes. The dispersion relation is a third order polynomial in  $\omega^2$ . By factoring out the SH-wave mode out of the dispersion relation the P and SV dispersion relation is reduced to a 2nd-order polynomial in  $\omega^2$ . By various approximations, the P-SV dispersion relation can be used to derive 4th-order linear wave

equations. If the second-order polynomial is further factored then two second order pseudo-differential equations that propagates anisotropic acoustic-like P and S-waves are derived. These equations can be solved with finite difference, pseudospectral, or phase-shift time-stepping methods which we show in this chapter.

## 4.1 Introduction

For narrow-offset seismic data in flat topography with VTI anisotropy, recorded P-waves travel close to vertical. As a result, isotropic migrations provide a good image. However, even in flat topography, anisotropic migration is essential for the imaging of faults and reefs since energy is traveling diagonally. The elastic wave equation allows modeling anisotropic P-waves and S-waves and conversion between these modes. However, the full elastic wave equation is computationally expensive for modelling and migration. As an alternative to elastic modeling and migration it is often preferred to propagate each body-wave mode separately with a pseudo-acoustic wave equation or a reduce system wave equation (Fletcher et al., 2009), which typically assumes a simple form of anisotropy like TTI or VTI. Pseudo-acoustic wave equations can properly account for anisotropic travel times and geometric spreading of seismic data generated by the elastic wave equation.

Converted wave RTM uses P-wave and S-wave propagators. S-waves waves have slower speeds and therefore require finer sampling of the time and spatial coordinates for finite-difference and pseudospectral solvers. In addition, S-waves are more sensitive to the anisotropy parameters making lower-symmetry wavefield propagators necessary. S-waves exhibit shear-wave splitting that P-waves do not. A layer stripping correction eliminates shear wave splitting by decomposition of the wavefield into slow and fast shear waves and bulk shifts in every anisotropic layer Cary and Zhang (2010).

In a homogenous isotropic elastic media, the acoustic wave equation propagates P-waves and S-waves exactly. In an isotropic homogeneous elastic media, the divergence of the vector wavefield,  $\nabla \cdot U$ , filters out the S-wave energy leaving the P-wave energy. The remaining P-wave energy satisfies an acoustic wave equation with the P-wave velocity. The curl of the wavefield,  $\nabla \times U$ , filters out the P-wave energy leaving behind the energy of the S-waves and satisfies an acoustic wave equation with the S-wave velocity. In piecewise-homogeneous isotropic media, the propagation of waves is exact within each layer however mode conversions are neglected at the interfaces which changes amplitudes of the P-P transmissions. In heterogeneous isotropic media this wave equation although not strictly valid can be used to approximately propagate a single body wave mode.

The procedure first isolates the phase velocity from the dispersion relation for each

body wave mode. In weak anisotropy media, the dispersion relation can be simplified. A pseudo acoustic wave equation that is pseudo-differential operator equation is derived that has the same dispersion relation. In the case of an isotropic velocity model, the pseudo-differential equation reduces to the acoustic wave equation. These procedures produce very good kinematics for the arrival time of the waves. We derive a number of pseudo-acoustic approximations and derive efficient numerical methods to solve these equations.

The analysis of S-wave splitting (Crampin, 1985) provides an important diagnostic tool to estimate the anisotropic parameters and therefore to infer fracture characteristics (Bakulin et al., 2000). For vertically fractured rocks, S-wave splitting depends on the orientation of the fractures and their size and density.

## 4.2 Pseudo-acoustic wavefield propagation

Many researchers have published results detailing two-way modelling and migration using pseudo-acoustic wavefield propagators. Alkhalifah (2000) derived a pseudo-acoustic wave equation from the coupled dispersion relation for pressure (P) and vertical shear (SV) waves. However, it generates SV-wave artifacts in the solution process. Grechka et al. (2004) explained that the shear wave artifacts arise from setting the vertical shear-wave velocity to zero. However, the horizontal shear-wave velocity is non-zero as a result of the anisotropy. The shear-wave artifacts give rise to instabilities. There have been many suggestions to stabilize and reduce the shear-wave artifacts. For example, if the vertical shear wave velocity is not set to zero but instead is a given a finite value, then instabilities arising from a variable tilt angle are eliminated. However, this increases the size of the shear-wave artifacts. To reduce the S-wave artifacts the shear-wave velocity can be solved to reduce reflections and transmissions of P-wave energy into SV-energy (Tsvankin, 2001). To eliminate S-waves artifacts at the source requires injecting the wavelet into an isotropic layer. Fletcher et al. (2009) suggests a number of different ways to use an approximate fourth-order dispersion relation to derive coupled partial differential equations (PDEs). When the combination of Thomsen parameters (Thomsen, 1986)  $\epsilon - \delta$  is either positive or negative a different PDE is necessary.

To avoid shear-wave artifacts and to avoid solving a coupled system of PDEs Etgen and Brandsberg-Dahl (2009) suggested the pseudo-analytic method that, instead of solving a coupled system of PDEs, solves a second-order PDE but with spatial derivatives defined by pseudo-differential operators. The method of Etgen and Brandsberg-Dahl (2009) interpolates between exact solutions. Song and Fomel (2010) splits the pseudo-analytical propagator into two parts using a Fourier FD approximation.\*\*\*

We discuss pseudo-acoustic wavefield propagation in anisotropic media (Wards

et al., 2008; Etgen and Brandsberg-Dahl, 2009). We then show how to use a dispersion relation in a rotated coordinate system. In later chapters we will use the anisotropic wavefield propagators to migrate a number of synthetic seismic datasets using a TTI and VTI reverse-time migration.

### 4.3 Dispersion relations for P and S waves in anisotropic media

The dispersion relation derived from the Kelvin-Christoffel equation is solved to determine the speed of propagation of the body wave modes. For anisotropic media the dispersion relation is dependent on the 21-independent parameters of the stiffness tensor. We consider simplifications of the dispersion relationship for various kinds of symmetrical anisotropic media like HTI, VTI, TTI, and orthorhombic media. Pseudo-acoustic waves are derived with the dispersion relation equation with the same phase velocities.

The elastic wave equation models wave traveling in the earth. This assumes that the earth is a lossless linear elastic solid with inertia terms ignored. In many record seismic data sets it is reasonable to assume that the elastic stiffness matrix has tilted transverse anisotropy (TTI) symmetry. TTI symmetry reduces the number of independent quantities to 7 plus the density parameter  $\rho$ . The seven parameters consist of 2 orientation angles and 5 independent elastic constants  $V_p$ ,  $V_s$ ,  $\epsilon$ ,  $\delta$ ,  $\gamma$ .

The dispersion relation for the acoustic wave equation with velocity  $c$  is

$$\omega^2 = (2\pi c)^2(k_x^2 + k_y^2 + k_z^2). \quad (4.1)$$

A simple anisotropic dispersion relation is the elliptic dispersion relation,

$$\omega_{elliptic}^2 = (2\pi)^2(c_v^2 k_z^2 + c_T^2(k_x^2 + k_y^2)), \quad (4.2)$$

where  $c_v$  is the velocity in the vertical direction and  $c_T$  is the velocity in the horizontal plane. The velocity in all directions is obtained by substituting the appropriate wavenumber vector into equation (4.2). Although the elliptic dispersion relation is anisotropic it is not usually a good approximation in the earth. A corresponding PDE that has the elliptic dispersion relation,

$$\frac{\partial^2 U}{\partial t^2} = \mathcal{F}_{\vec{k} \rightarrow \vec{x}}^{-1}(\omega_{elliptic}^2 \mathcal{F}_{\vec{x} \rightarrow \vec{k}}(U)). \quad (4.3)$$

In the space domain the equation is,

$$\frac{\partial^2 U}{\partial t^2} = c_v^2 \frac{\partial^2 U}{\partial z^2} + c_T^2 \left( \frac{\partial^2 U}{\partial x^2} + \frac{\partial^2 U}{\partial z^2} \right). \quad (4.4)$$

Pseudo-acoustic wave equations are simplifications of the elastic-wave equation that only propagate a single mode without coupling effects. Instead, each mode propagates with the same phase velocity as the corresponding mode determined by the dispersion relation derived from the elastic-wave equation.

In the case of vertical transverse anisotropy (VTI) the eigenvalues or velocities in Thomsen (1986) anisotropic parameters  $\epsilon$ ,  $\delta$ ,  $\gamma$ ,  $V_{P_0}$ , the vertical P-wave velocity, and velocity  $V_{S_0}$ , the vertical S-wave velocity  $V_{S_0}$  are,

$$V_P(\theta)^2 = V_{P_0}^2 \left[ 1 + \epsilon \sin^2 \theta - \frac{f}{2} + \frac{f}{2} \sqrt{1 + \frac{4 \sin^2 \theta}{f} (2\delta \cos^2 \theta - \epsilon \cos 2\theta) + \frac{4\epsilon^2 \sin^4 \theta}{f^2}} \right] \quad (4.5)$$

$$V_{SV}(\theta)^2 = V_{P_0}^2 \left[ 1 + \epsilon \sin^2 \theta - \frac{f}{2} - \frac{f}{2} \sqrt{1 + \frac{4 \sin^2 \theta}{f} (2\delta \cos^2 \theta - \epsilon \cos 2\theta) + \frac{4\epsilon^2 \sin^4 \theta}{f^2}} \right] \quad (4.6)$$

$$V_{SH}(\theta)^2 = V_{S_0}^2 [1 + 2\gamma \sin^2 \theta] \quad (4.7)$$

where  $f = 1 - V_{S_0}/V_{P_0}$  and  $V_{S_0}$  is the vertical S-wave velocity and  $V_{P_0}$  is the vertical P-wave velocity.

Equations (4.5), (4.6), and (4.7) can be linearized about the small parameters  $\epsilon$ ,  $\delta$ , and  $\gamma$  to give,

$$V_P(\theta)^2 = V_{P_0}^2 [1 + (2\delta - 2\epsilon) \sin^2 \theta \cos^2 \theta + 2\epsilon \sin^2 \theta], \quad (4.8)$$

$$V_{SV}(\theta)^2 = V_{S_0}^2 \left[ 1 + \frac{V_{P_0}^2}{V_{S_0}^2} (2\epsilon - 2\delta) \sin^2 \theta \cos^2 \theta \right], \quad (4.9)$$

$$V_{SH}(\theta)^2 = V_{S_0}^2 [1 + 2\gamma \sin^2 \theta]. \quad (4.10)$$

This linearization is designed for NMO correction of seismic data and so is less accurate for velocities near horizontal propagation. For other possible approximations of the dispersion relation see Fowler (2003).

#### 4.4 Wavenumber representation of dispersion relations

The dependence of the wavefield on the direction of propagation is achieved through expressing the dispersion relation in terms of wavenumbers,  $\vec{k}$ . In terms of the dip  $\theta$

$$\begin{aligned} k_x &= |\vec{k}| \sin \theta \\ k_z &= |\vec{k}| \cos \theta, \end{aligned} \quad (4.11)$$

in 2D. In 3D the wavenumbers in terms of the azimuth  $\phi$  and dip  $\theta$  are,

$$\begin{aligned} k_x &= |\vec{k}| \sin \theta \cos \phi \\ k_y &= |\vec{k}| \sin \theta \sin \phi \\ k_z &= |\vec{k}| \cos \theta. \end{aligned} \quad (4.12)$$

Substituting equation (4.11) into equation (4.6) gives a dispersion relation,

$$\begin{aligned} \omega_{SV}^2(k_x, k_z) = & \\ |\vec{k}|^2 V_{P_0}^2 \left[ 1 + \epsilon \sin^2 \theta - \frac{f}{2} - \frac{f}{2} \sqrt{1 + \frac{4 \sin^2 \theta}{f} (2\delta \cos^2 \theta - \epsilon \cos 2\theta) + \frac{4\epsilon^2 \sin^4 \theta}{f^2}} \right]. \end{aligned}$$

In terms of the wavenumbers  $k_x$  and  $k_z$  the exact VTI dispersion relation for SV-waves is,

$$\begin{aligned} \omega_{SV}^2(k_x, k_z) = & \\ V_{P_0}^2 \left[ k^2 \left( 1 - \frac{f}{2} \right) + \epsilon k_x^2 - \frac{f}{2} \sqrt{k^4 + \frac{4k_x^2}{f} (2\delta k_z^2 - \epsilon (k_z^2 - k_x^2)) + \frac{4\epsilon^2 k_x^4}{f^2}} \right]. \end{aligned} \quad (4.13)$$

For TTI media the axis of rotation is not aligned with the coordinate axis. Given a tilt of angle  $\beta$  from vertical, the dispersion relation for the weak linearly approximation is

$$V_P^2(\theta) = V_{P_0}^2 \left[ 1 + (2\delta - 2\epsilon) \sin^2(\theta - \beta) \cos^2(\theta - \beta) + 2\epsilon \sin^2(\theta - \beta) \right]. \quad (4.14)$$

We would like to express the dispersion relation in terms of  $\beta$ ,  $k_x$ , and  $k_z$  because the angle  $\beta$  is spatially dependent. In terms of a rotation matrix  $R(\beta)$  the dispersion relation is,

$$\omega_{R(\beta)}(\vec{k}, \vec{x}) = \omega(R(\beta)\vec{k}, \vec{x}) \quad (4.15)$$

In general, the angle  $\beta$  will be spatially dependent.

## 4.5 Wavefield propagation in anisotropic heterogeneous media

The dispersion relation  $\omega(\vec{k})$  defines a wave equation whose phase velocity is the same as the phase velocity of the elastic wave equation for any particular body wave mode. A homogeneous anisotropic wave equation with phase velocity  $\omega_{ani}(\vec{k}, \vec{x})$  is

$$\frac{\partial^2 U}{\partial t^2} = -\mathcal{F}_{\vec{k} \rightarrow \vec{x}}^{-1} \left( \omega^2(\vec{k}) \hat{U}(\vec{k}) \right). \quad (4.16)$$

This equation is hyperbolic provided  $\omega(\vec{k}) > 0$ . Equation (4.16) has an approximate solution

$$U^{n+1}(\vec{x}) = -U^{n-1}(\vec{x}) + 2\mathcal{F}_{\vec{k} \rightarrow \vec{x}}^{-1} \left[ \cos \left( \omega(\vec{k}, \vec{x}) \delta t \right) \mathcal{F}_{\vec{x} \rightarrow \vec{k}} [U^n(\vec{x})] \right]. \quad (4.17)$$

Wavefield propagation by equation (4.17) in heterogeneous anisotropic media is too expensive. As a result, the kernel of the Fourier integral operator  $\cos(\omega(\vec{k}, \vec{x}) \delta t)$  is approximated with a separable approximation. A separable approximation is of the form,

$$\cos \left( \omega(\vec{k}, \vec{x}) \delta t \right) = \sum_{i=1}^N F_i(\vec{x}) G_i(\vec{k}). \quad (4.18)$$

This allows numerical evaluation of equation (4.17) with a forward Fourier Transform and  $N$  inverse Fourier transforms. An alternative approximation of calculating is to expand the cosine in a multi-parameter power series expansion about  $\epsilon, \delta, \gamma, \theta, V_p, \beta$ , and  $V_s$ .

## 4.6 Wavefield propagation in orthorhombic media

In orthorhombic media the stiffness tensor in the Voigt notation is,

$$C = \begin{bmatrix} C_{11} & C_{12} & C_{13} & & & \\ & C_{22} & C_{23} & & & \\ & & C_{33} & & & \\ & & & C_{44} & & \\ & & & & C_{55} & \\ & & & & & C_{66} \end{bmatrix}, \quad (4.19)$$

here  $C$  depends on 9 independent quantities. Additionally if the anisotropic directions change, there are 3 orientation angles. To approximate P-wave media, some of the 9 quantizes may be unimportant. Similar to VTI we adopt the weak elastic approximation notation Tsvankin (2001). the P-wave vertical velocity:

$$V_{P0} = \sqrt{c_{33}/\rho} \quad (4.20)$$

The vertical S-wave velocities corresponding to polarization in the  $x_1$ , and  $x_2$ ,

$$V_{SO} = \sqrt{c_{55}/\rho}, V_{s1} = \sqrt{c_{66}/\rho} \quad (4.21)$$

In the  $x_1 - x_3$  plane the anisotropy is described in the same way as VTI media can be described. The parameter

$$\epsilon_2 = \frac{C_{11} - C_{33}}{2C_{33}}, \quad (4.22)$$

represents the relative difference in the vertical ( $x_3$  direction) P-wave velocity to the P-wave velocity in the  $x_1$  direction. The parameter

$$\delta_1 = \frac{(C_{23} + C_{44})^2 - (C_{33} - C_{44})^2}{2C_{33}(C_{33} - C_{44})}, \quad (4.23)$$

$$\epsilon_1 = \frac{C_{22} - C_{33}}{2C_{33}}, \quad (4.24)$$

$$\delta_2 = \frac{(C_{13} + C_{55})^2 - (C_{33} - C_{55})^2}{2C_{33}(C_{33} - C_{55})}, \quad (4.25)$$

$$\epsilon_2 = \frac{C_{11} - C_{33}}{2C_{33}}, \quad (4.26)$$

$$\delta_3 = \frac{(C_{13} + C_{66})^2 - (C_{11} - C_{66})^2}{2C_{11}(C_{11} - C_{66})}, \quad (4.27)$$

$$\gamma_1 = \frac{C_{66} - C_{55}}{2C_{55}}, \quad (4.28)$$

$$\gamma_2 = \frac{C_{66} - C_{44}}{2C_{44}}. \quad (4.29)$$

The weak anisotropic parameters are an intuitive way to parameterize the dispersion relations for the body wave modes. Thomsen's weak anisotropic parameters also provide a convenient set of parameters about which to linearize the dispersion relation.

## 4.7 Numerical examples

Impulse responses in homogeneous TTI media are calculated to demonstrate wavefield propagation with equation (4.17). Although both P and SV wave modes are propagated separately both are displayed over top of each other for convenience. Figure 4.1 is the image of a variety of impulses propagated with pseudo-acoustic wave equations. In the top left of Figure 4.1 is a pure SV impulse response using the exact dispersion relation. In the top right of Figure 4.1 is an image of two overlaid impulse responses using the exact P-wave and the exact S-wave dispersion relations. In the bottom left part of Figure 4.1 is the impulse responses from a linear P-wave dispersion relation and a quadratic linearization of the S-wave dispersion relation. a simple linearization is not sufficiently accurate for S waves. In the bottom right of the figure is the difference between the P-wave and S-wave impulse responses described above.

Figure 4.2 is the exact same as Figure 4.1 except the value of  $\delta$  is  $-0.2$  instead of being  $0.1$ . For the choice of anisotropic parameters in Figure 4.2 there is a triplication of the SV wavefronts.

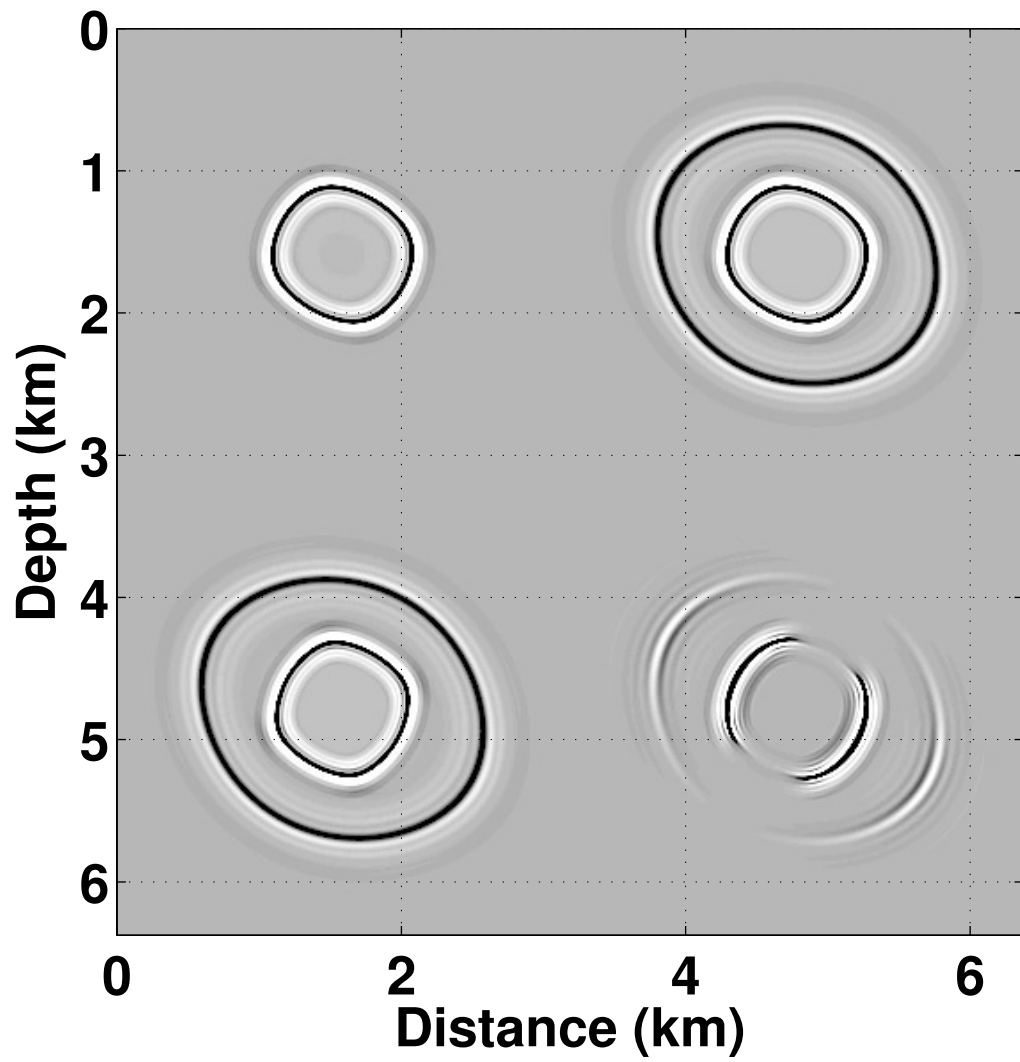


Figure 4.1: Comparison of SV and P forward modelling impulse response for wavefield propagation  $V_p = 2965$ ,  $V_s = 1485$ ,  $\epsilon = 0.196$ ,  $\delta = 0.1$ , and the tilt angle  $\beta = 30^\circ$ . The propagation of P and SV waves are done separately.

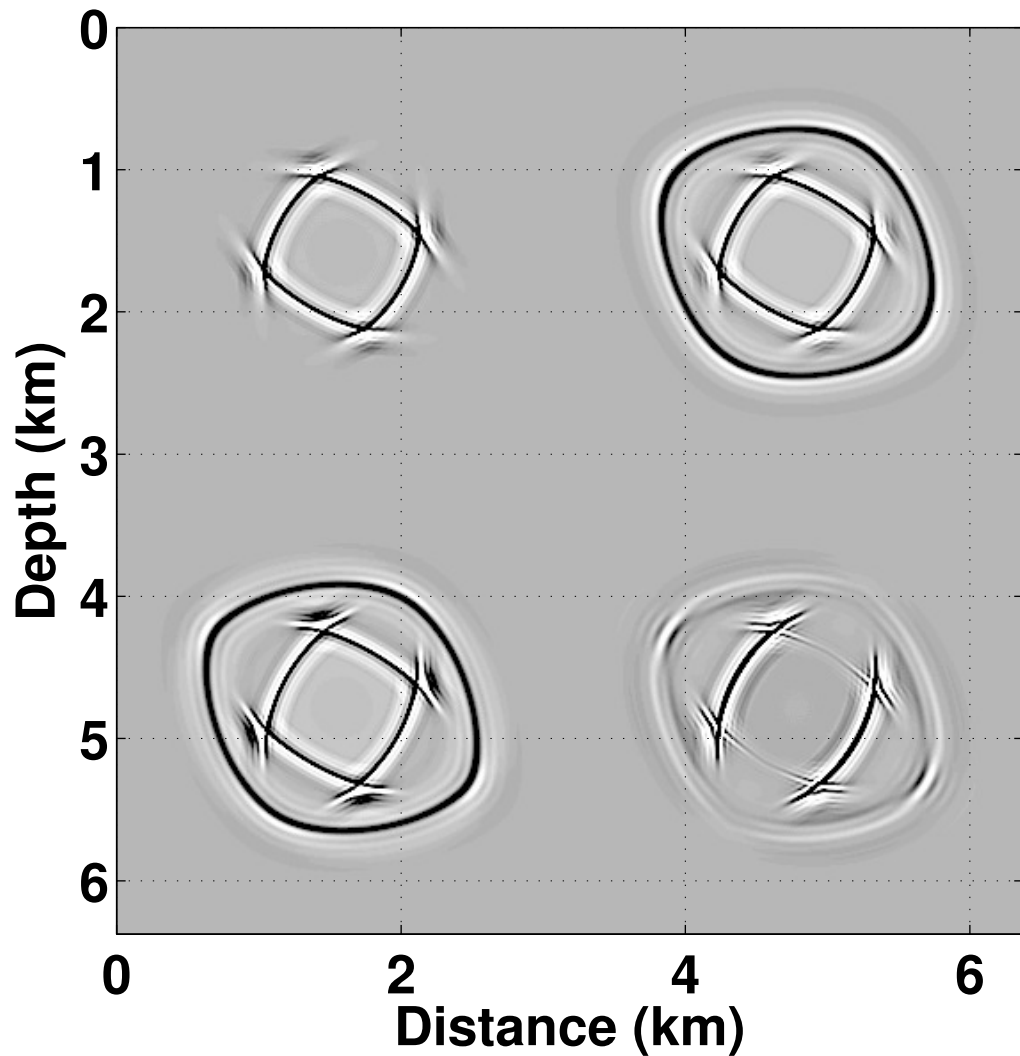


Figure 4.2: SV and P wave impulse responses with Thomsen's anisotropic specified as  $V_p = 2965$ ,  $V_s = 1485$ ,  $\epsilon = 0.196$ ,  $\delta = -.2$ , and the tilt angle  $\beta = 30^\circ$ .

## 4.8 Conclusion

The dispersion relation was used to derive pseudo-acoustic wave equations for P-waves and S-waves. We presented a method of solving pseudo-acoustic wave equations using an exact solution for constant velocity, which has significant computational advantage over solving the elastic wave equation. It is preferred to propagate with a pseudo-differential equation than with a coupled system of linear PDEs because they do not suffer from S-wave artifacts and instability issues.

# Chapter 5

## Reverse time migration: imaging conditions, aliasing, and artifacts

### 5.1 Introduction

RTM is a powerful migration algorithm that honors multipathing through a complicated velocity model. RTM has the ability to images multiples and duplex waves and can preserves travel times and amplitudes through highly complex velotiy models. RTM is computationally slow compared Kirchhoff migration and depth continuation algorithms. In RTM, the crosscorrelation of the forward propagated shot field and the back-propagated receiver field produces a migrated shot record. Mutliples, diving waves, and surface waves crosscorrelate to produce false reflections and noise which reduce the quality of the migrated image. In this chapter, we compare common methods of implementing the imaging condition and reducing imaging condition artifacts and develop an aliasing condition so that the migrated image is not aliased.

McMechan (1983) describes a poststack RTM algorithm called "boundary value migration". Poststack RTM uses the NMO corrected stacked recorded seismic data as a time-dependent boundary condition at the surface of the model and propagates with a two-way wave equation. Poststack RTM back-propagates the stacked NMO corrected data in time into the subsurface with half the modelling velocity. The recorded wavefield is back-propagated to time  $t = 0$ , the imaging time. Independently, Whitmore (1983) and Baysal et al. (1983) developed the same method, called backward time propagation and RTM, respectively. The acoustic wave equation is symmetric about a reversal of the time coordinate. As a result, when the recorded wavefield is used as a time dependent boundary condition or as a forcing term at the receiver locations, the back scatter wavefield is back propagated through the earth model by solving the wave equation.

In prestack RTM (Chang and McMechan, 1987), a reflection event occurs when shot and reliever field both have energy at the space spatial location and at the same propagation time. This imaging condition is essentially the same as that originally proposed by Claerbout (1971). In prestack RTM, a shot field is forward propagated by solving the acoustic wave equation, and the receiver field is similarly back propagated. RTM resolves complex targets with multi-path energy where conventional migration

algorithms fail (Whitmore and Lines, 1986).

## 5.2 Born forward modelling and its inverse

Let  $G_0(\vec{x}, \vec{x}_s, t)$  be the causal Green's function for the acoustic wave equation,

$$\left[ \frac{\partial^2}{\partial t^2} - c_0(\vec{x})^2 \Delta \right] G_0(\vec{x}, \vec{x}_s, t) = \delta(\vec{x} - \vec{x}_s), \quad (5.1)$$

with a background velocity  $c_0$  and where  $\Delta = \partial_{xx} + \partial_{yy} + \partial_{zz}$ .

The Born scattering approximation can be used to create a synthetic seismic shot record or as a bases for a linearized inversion. For seismic data recorded at point  $\vec{x}_r$  for a shot at location at  $\vec{x}_s$  with a velocity  $c(\vec{x})$ , a background velocity  $c_0$  and a velocity perturbation  $\delta c(\vec{x}) = c(\vec{x}) - c_0(\vec{x})$ , the weak scattering approximation (Schuster, 2002) in the frequency domain is

$$D(\vec{x}_r, \vec{x}_s, \omega) = \int G_0(\vec{x}_r, \vec{x}, \omega) G_0(\vec{x}, \vec{x}_s, \omega) m(\vec{x}) d\vec{x}, \quad (5.2)$$

where  $m(\vec{x}) = 2\delta c/c_0^3$  is the scattering potential. Let  $G_0^*$  be the solution to the adjoint of equation (5.1). An approximate inverse of equation (5.2) can be formed by applying the adjoint of the forward modelling operator,

$$m(\vec{x}) \approx \omega^2 \int G_0^*(\vec{x}, \vec{x}_s, \omega) G_0^*(\vec{x}_r, \vec{x}, \omega) D(\vec{x}_r, \omega) d\vec{x}_r. \quad (5.3)$$

The Green's function  $G_0^*(\vec{x}, \vec{x}_s, \omega)$  is called the forward propagated shot field. A band-limited version of  $G_0^*$  can be calculated by FD approximation of equation (5.1) with the delta function multiplied with a wavelet  $W(\omega)$ . The Green's function applied to the recorded data  $G_0^*(\vec{x}_r, \vec{x}, \omega) D(\vec{x}_r, \omega)$  is called the back propagated receiver field. In the time domain the receiver field is,

$$\begin{aligned} R_{\vec{x}_s}(t, \vec{x}) &= G_0(\vec{x}_r, \vec{x}, t) \otimes_t D(\vec{x}_r, t) \\ &= \int_0^{T_{max}} G_0(\vec{x}_r, \vec{x}, \tau) D(\vec{x}_r, t + \tau) d\tau, \end{aligned}$$

where  $T_{max}$  is the length of the seismic record and  $\otimes_t$  is cross-correlation in the time variable. Integrating the recorded wavefield  $D(\vec{x}_r, t + \tau)$  with Green's function  $G_0(\vec{x}_r, \vec{x}, \tau)$  can be accomplished by solving the wavefield equation using the trace as a time shifted source,

$$\left[ \frac{\partial^2}{\partial t^2} - c_0(\vec{x})^2 \Delta \right] R(\vec{x}, t) = D(\vec{x}, t_{max} - t). \quad (5.4)$$

For converted waves from a P-wave source the analogous forward born modelling that is kinematically correct is

$$D^{PS}(\vec{x}_r, \vec{x}_s, \omega) = \int G_0^P(\vec{x}_r, \vec{x}, \omega) G_0^S(\vec{x}, \vec{x}_s, \omega) m^{PS}(\vec{x}) d\vec{x}, \quad (5.5)$$

here  $m^{PS}$  is the scatter potential for  $PS$  conversion. The forward Born approximation for elastic waves (Snieder, 2002) will have much better dynamic amplitudes. Applying the adjoint to the recorded converted wavefield gives an approximate inverse,

$$m^{PS}(\vec{x}) \approx \omega^2 \int G_0^{P*}(\vec{x}, \vec{x}_s, \omega) G_0^{S*}(\vec{x}_r, \vec{x}, \omega) D^{PS}(\vec{x}_r, \omega) d\vec{x}_r. \quad (5.6)$$

### 5.3 Imaging conditions for RTM

The back-propagated wavefield is multiplied with the forward modeled shot in the reverse computational order. As a result either the shot field or the receiver field much stored in memory or recomputed. In order to reduce memory requirements and I/O costs, (Symes, 2007) stores a few snapshots of the shot field called checkpoints which are used to recompute the shot wavefield in the same order as the receiver field is computed. RTM consists of the following steps:

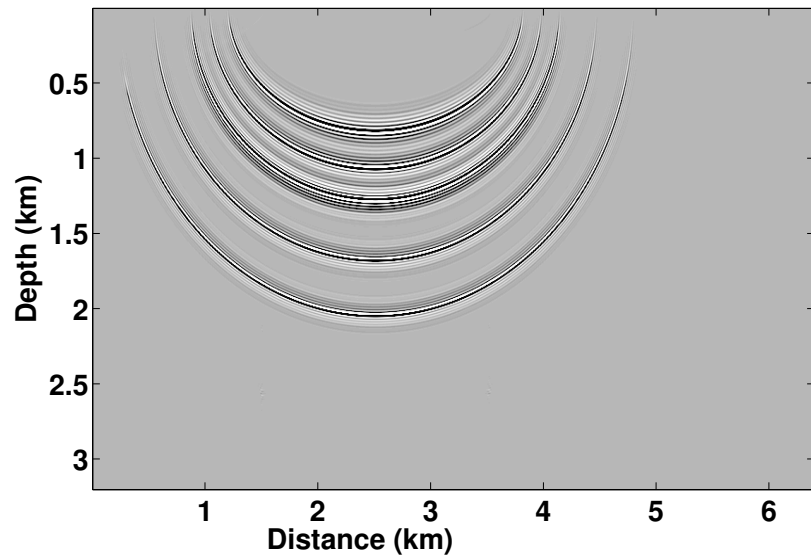
- Forward propagate the shot field in time by either finite-differencing the wave equation, a pseudospectral method, or a method like that of this paper (Chen, 2007; Carcione et al., 2002).
- While forward propagating the shot field, store checkpoints (Symes, 2007).
- Back propagate the recorded receiver field and back propagate the shot field from the stored checkpoints.
- Apply an imaging condition at each time step of the back propagation.

Let the recorded seismic data be  $D(t, \vec{x}_{transvers})$  where  $t = 0$  is the start of the shot record and  $\vec{x}_{transverse}$  are the coordinates of the recording surface. For a flat straight 2-D seismic line  $\vec{x}_{transvers} = x$ . Let  $S(t, \vec{x})$  be the forward propagated shot field in the earth or the computational model where  $t = 0$  is the start of propagation. Let  $R(t, \vec{x})$  be the back propagated receiver field for a seismic data set recorded to time  $t = T$  where  $R(0, \vec{x})$  is the end of backpropagation and  $R(T, \vec{x})$  is the start of back propagation. To use the record seismic data as a time dependant condition for flat recording surface the following the condition is imposed

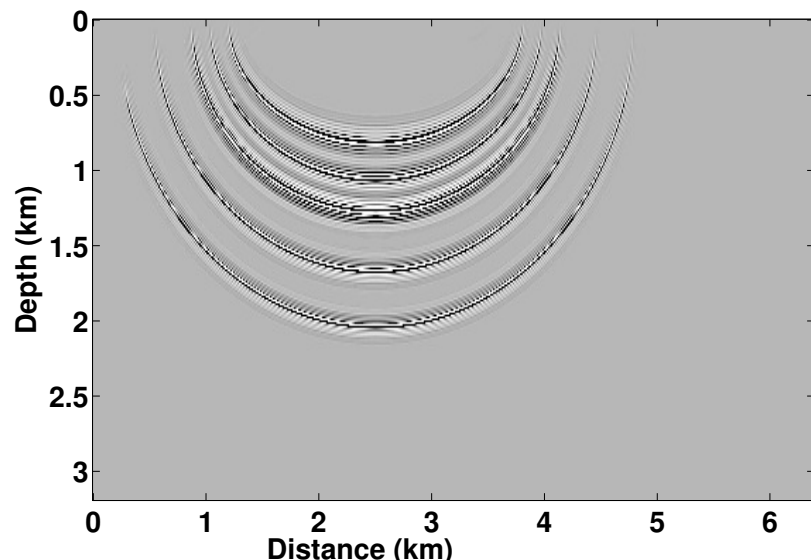
$$R(t, \vec{x}_{transvers}, 0) = D(t, \vec{x}_{transvers}). \quad (5.7)$$

If the recording surface is defined by the condition  $\vec{x}_{recording} = surface(\vec{x}_{transvers})$  then we impose the condition

$$R(t, surface(\vec{x}_{transvers})) = D(t, \vec{x}_{transvers}). \quad (5.8)$$



(a)



(b)

Figure 5.1: (a) Impulse migration response for a single far offset trace resampled prior to crosscorrelation to half the Nyquist sampling rate. (b) The migration impulse response with no resampling.

Alternatively the back propagated receiver field can be initiated with a forcing term,

$$R(t - \delta t, \text{surface}(\vec{x}_{\text{transvers}})) = R(t, \text{surface}(\vec{x}_{\text{transvers}})) + D(t, \vec{x}_{\text{transvers}}), \quad (5.9)$$

in between each propagation step.

Claerbout (1971) imaging principle defines a reflector to exist where the receiver field  $R(t, \vec{x})$  coexists with the shot field  $S(t, \vec{x})$ . The imaging condition is a comparison of the shot field and receiver field at the same propagation time which is a zero-lag crosscorrelation in time. The crosscorrelation imaging condition,

$$I(\vec{x}) = \int_0^T S(t, \vec{x}) R(t, \vec{x}) dt, \quad (5.10)$$

is stable but it is not a reflectivity because it is not the ratio of the up-going and down-going wavefields. The deconvolution imaging condition is the ratio of the two fields,

$$I(\vec{x}) = \int_0^T \frac{S(t, \vec{x})}{R(t, \vec{x})} dt. \quad (5.11)$$

The deconvolution imaging condition is unstable when division by zero occurs. The average of the down-going wavefield is added to the denominator to form a stabilized deconvolution imaging condition,

$$I(\vec{x}) = \int_0^T \frac{S(t, \vec{x}) R(t, \vec{x})}{R^2(t, \vec{x}) + \epsilon^2} dt, \quad (5.12)$$

where

$$\epsilon^2 = \alpha \int_0^T R(t, \vec{x}) dt$$

for some arbitrary constant  $\alpha$  which is determined by experimentation.

The imaging condition in RTM produces a lot of migration artifacts which blur the reflectivity image. Diving waves, head waves, or backscattered waves crosscorrelate in the imaging condition to produce migration artifacts. Many migrations artifacts are low frequency because they occur when two waves travel in the same direction in the shot and receiver fields. As a result, high pass filter significantly improves the image. The migration artifacts are worse near high velocity contrasts.

To reduce migration artifacts a number of techniques have been used. A non-reflecting wave equation prevents migration artifacts caused by multiples from being created. However, non-reflecting wave equations adversely affects amplitudes of reflection events, and multiples and duplex waves cannot be imaged.

Yoon et al. (2004) detects the direction of propagation of the waves with the method of Poynting vectors. The shot field and receiver field only allows reflection contribution if directional vectors are within certain angle. However, the direction detection method is noisy and since there are multiple overlapping events it is not always possible to detect the directions of all the waves.

### 5.3.1 Laplacian filtering

A popular method of removing migration artifacts is to apply a Laplacian filter (Youn and Zhou, 2001) or a vertical derivative to the stacked image. This has the effect of distorting the amplitudes by amplifying the high frequency noise and by filtering out the low-frequency signal. The Laplacian acts a taper on angle domain gathers without the need to explicitly calculate the angle gathers \*\*\*reference.

$$k_x^2 + k_y^2 + k_z^2 = \frac{4\omega^2 \cos^2 \theta}{v^2} \quad (5.13)$$

This technique is equivalent to tapering the angle domain

### 5.3.2 Directional wavefield decomposition

Liu et al. (2011) decomposes the shot and receiver shot fields into different propagation directions and only those directions that are opposite contribute to the image. However, in 3D fully decomposition of the wavefield into 8 directions is expensive, while a partial decomposition will result in missing structures.

Reverse-time migration (RTM) is a powerful migration method provided that an accurate velocity model can be constructed. In any discrete operation on a sampled field we need to consider aliasing before, during, and after that operation. Reverse-time migration takes a sampled seismic experiment and creates an image of the subsurface. In reverse-time migration the sampled wavefield and the forward modelled shot field are propagated as a solution to the wave equation. This often requires re-sampling the data to a regular sampled and finer grid for wavefield propagation. Additionally, aliasing can occur when cross-correlating the two wavefields to form an image.

## 5.4 Aliasing in the imaging condition

Aliasing occurs in prestack Kirchhoff migration when data in a shot record is swept from steep angles into the correct position. Steeply dipping events are often aliased in seismic data. Interpolating between traces reduces the trace spacing allowing migration operator to image steeply dipping events. Applying anti-aliasing filters (Gray, 1992; Biondi, 2001; Zhang et al., 2003) during migration eliminates steeply dip events. Aliasing can occur in two places for prestack wavefield continuation migrations. The downward propagated record wavefield and the forward modelled shot field must be adequately sampled for the propagation algorithm. To avoid aliasing during the cross-correlation imaging condition the shot and receiver fields are sampled at half the Nyquist sampling (Zhang et al., 2003).

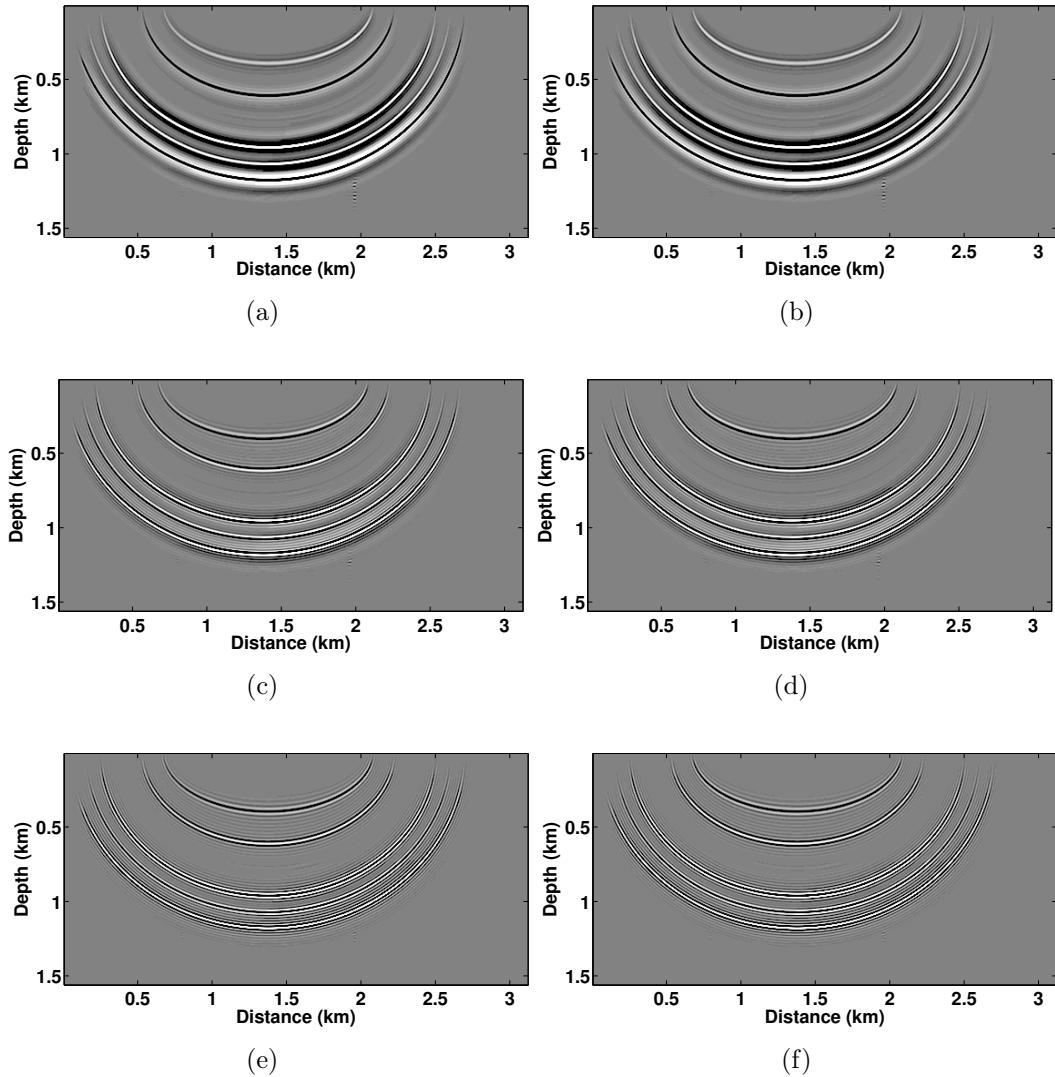


Figure 5.2: Impulse response in a constant velocity medium for an offset trace with the Laplacian filtering applied. The trace was created by convolving a trace containing 5 nonzero elements with a zero phase Ormsby wavelet. (a) Shot illumination condition with input trace integrated twice. (b) Crosscorrelation imaging condition with the input trace integrated twice. (c) Shot illumination condition with input trace integrated once. (d) Crosscorrelation imaging condition with the input trace integrated once. (e) Shot illumination condition with the input trace not integrated. (f) Crosscorrelation imaging condition with the input trace not integrated.

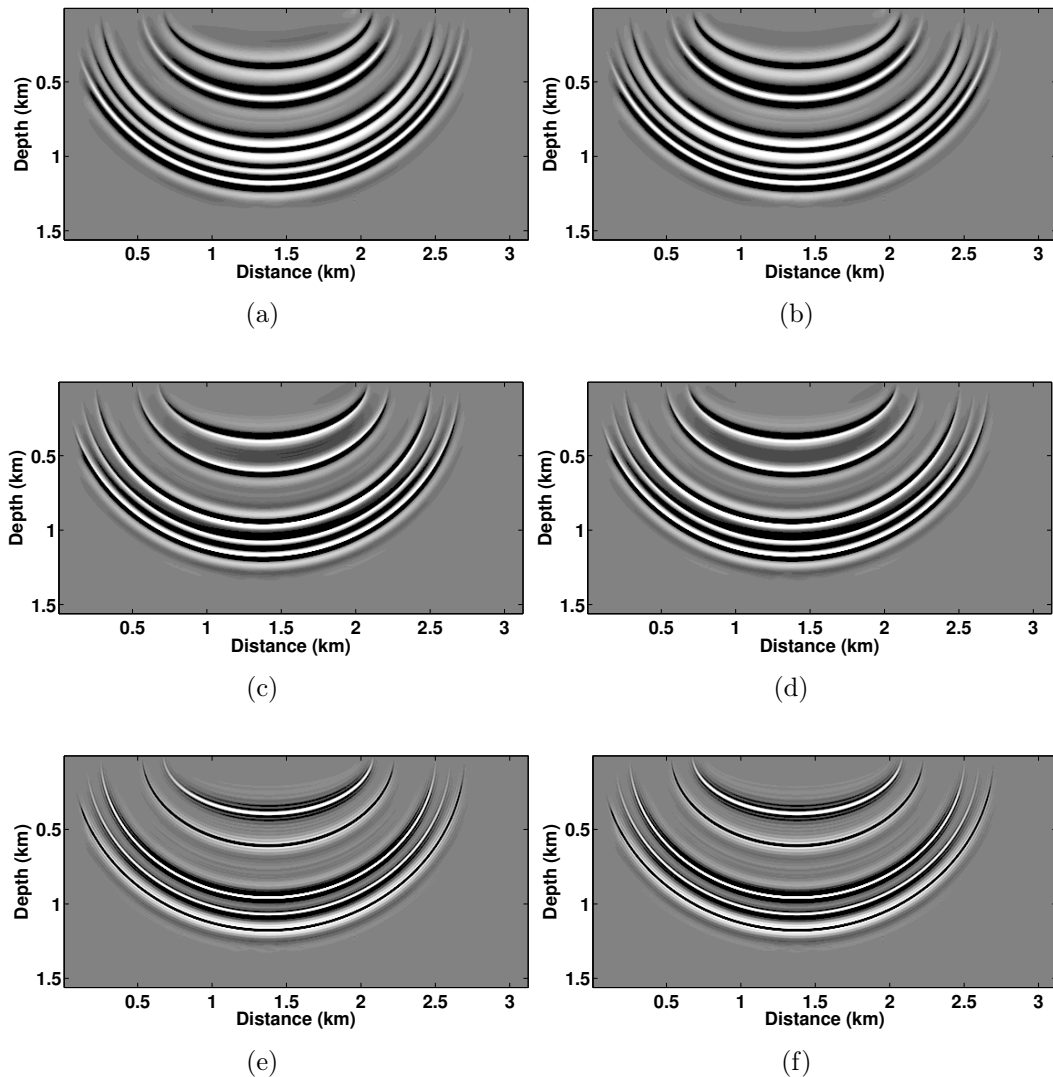


Figure 5.3: The same parameters used in Figure 5.2 except no Laplacian filter was applied to the migrated impulse responses.

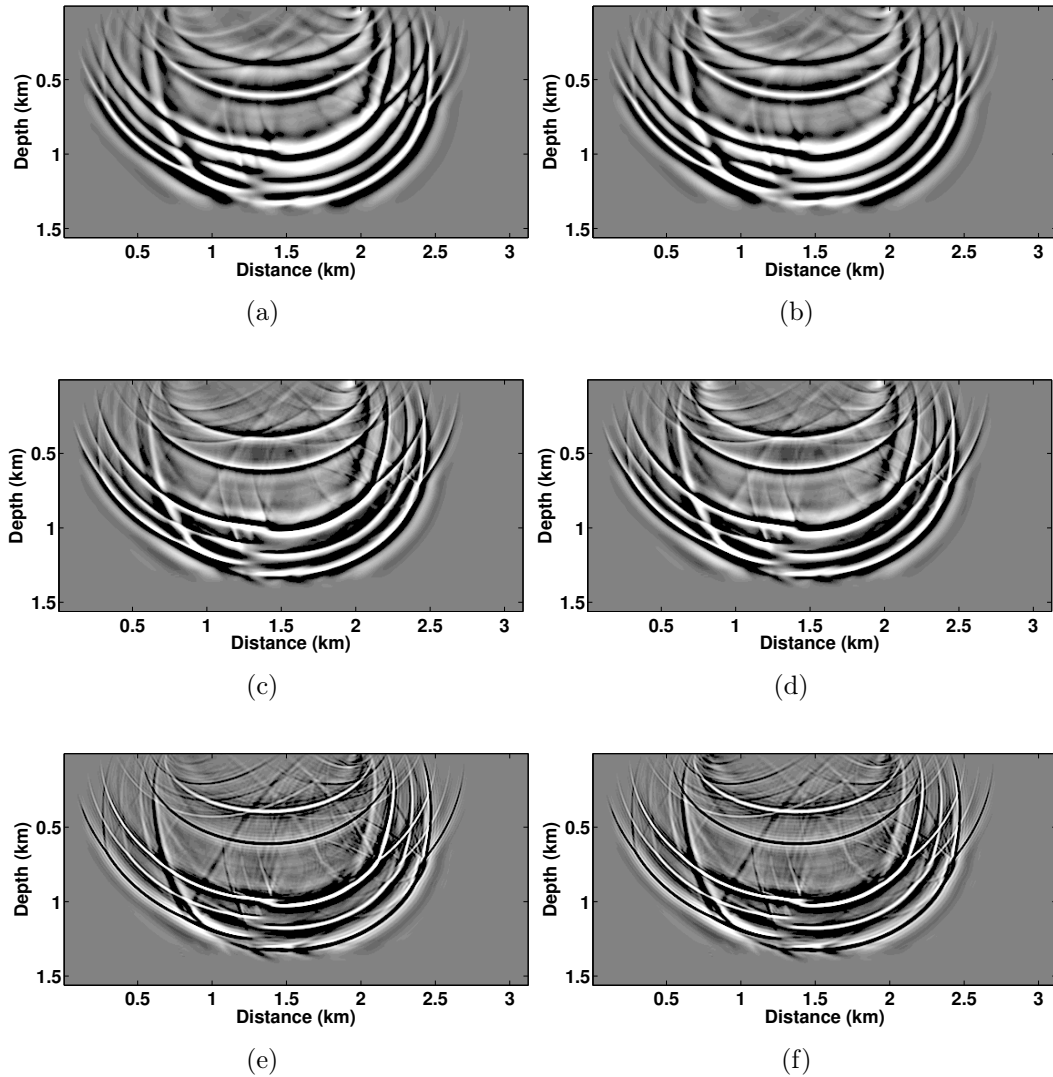


Figure 5.4: The same impulse responses with the parameters used in Figure 5.2 except no Laplacian filter was applied to the migrated impulse responses and the velocities from the Hess data was used which is Figure 5.8.

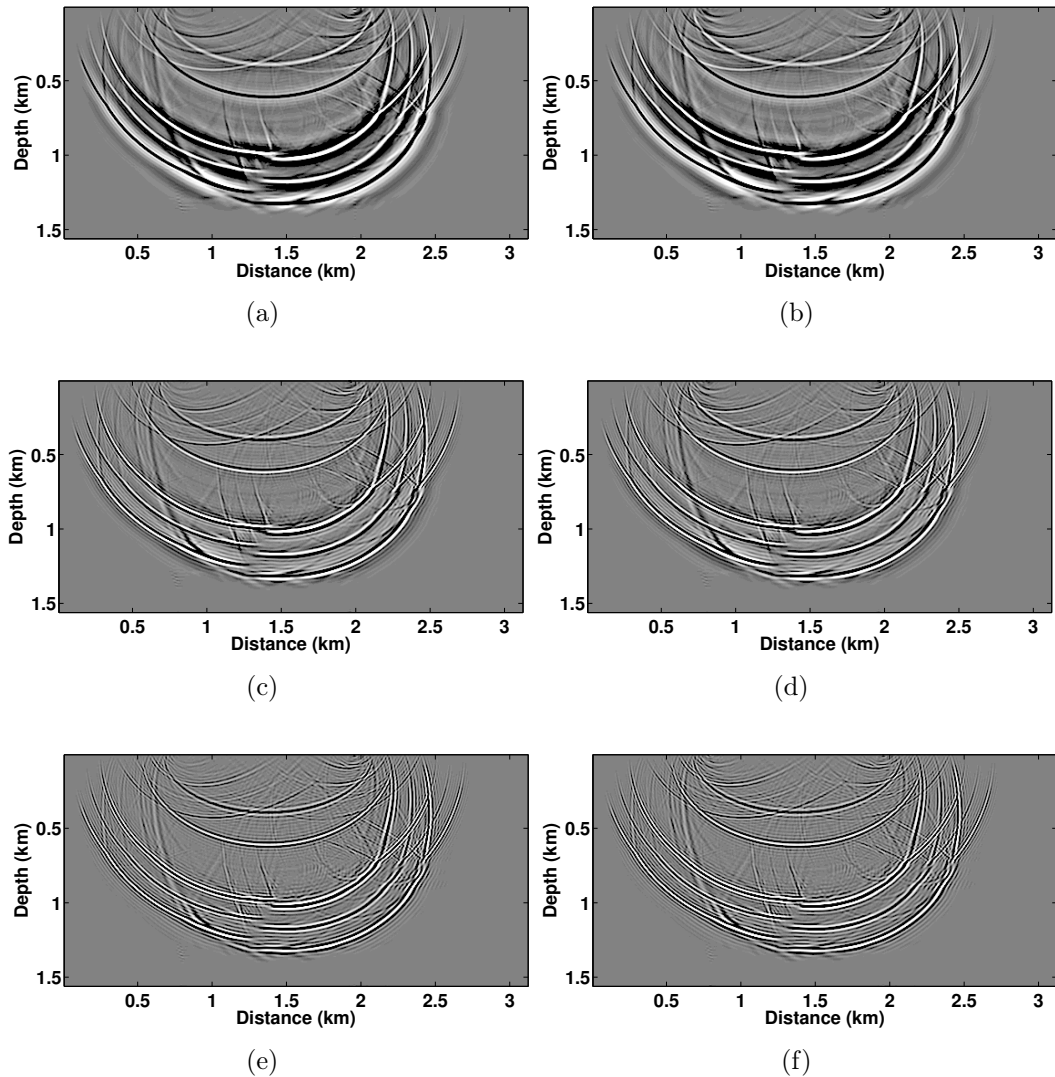


Figure 5.5: The same impulse response parameters used in Figure 5.2 except with the Hess vertical velocity in Figure 5.8 was used in the migration and the trace was taken from the Hess VTI dataset.

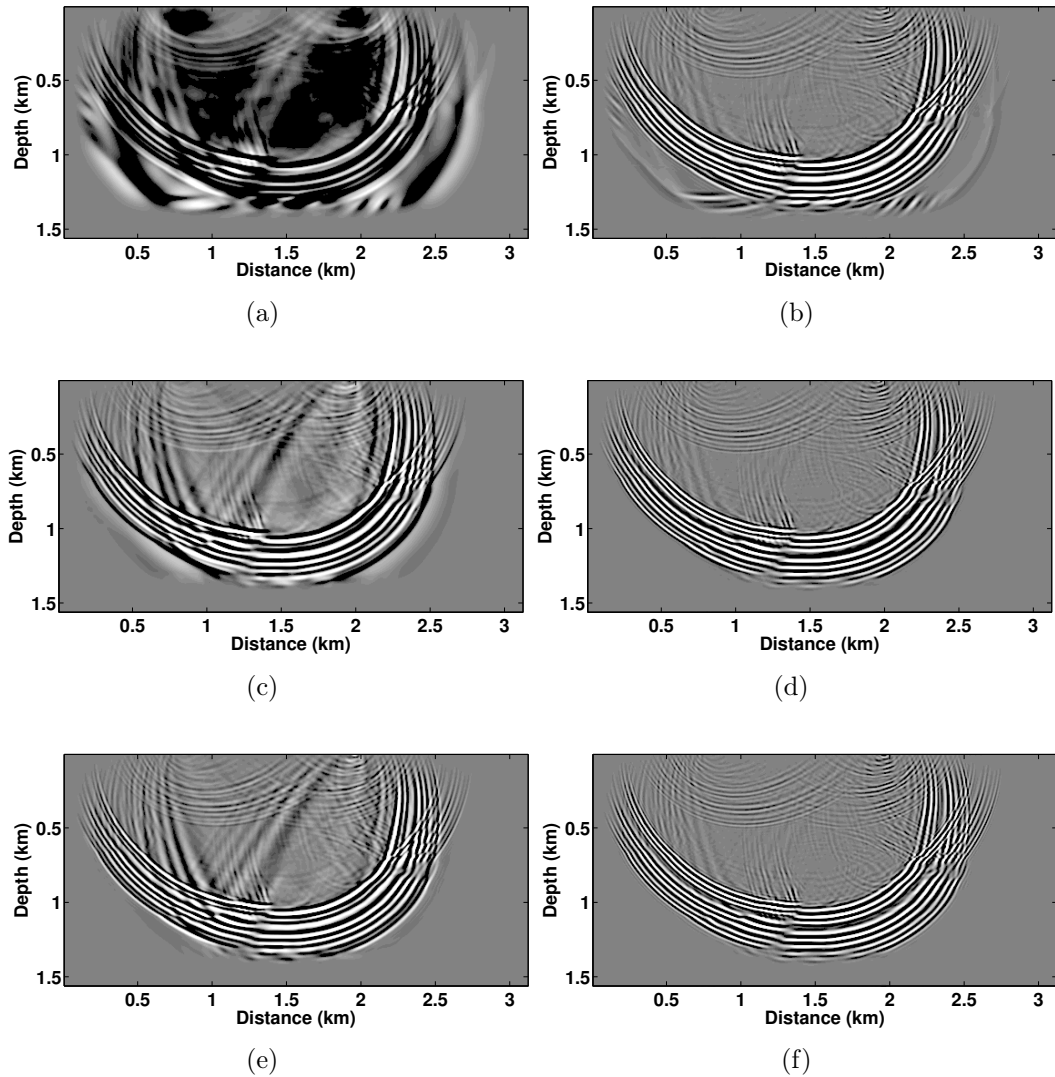


Figure 5.6: The migration impulse responses for an offset trace with the Hess velocity field used for the migration velocities and with a trace from the Hess VTI dataset. (a) The input trace was integrated twice. (b) The input trace was integrated twice, and the Laplacian filter was applied to the migration response. (c) The input trace was integrated once. (d) The input trace was integrated once, and the Laplacian filter was applied to the migration response. (e) The input trace was not integrated. (f) The input trace was not integrated, and the Laplacian filter was applied to the migration response.

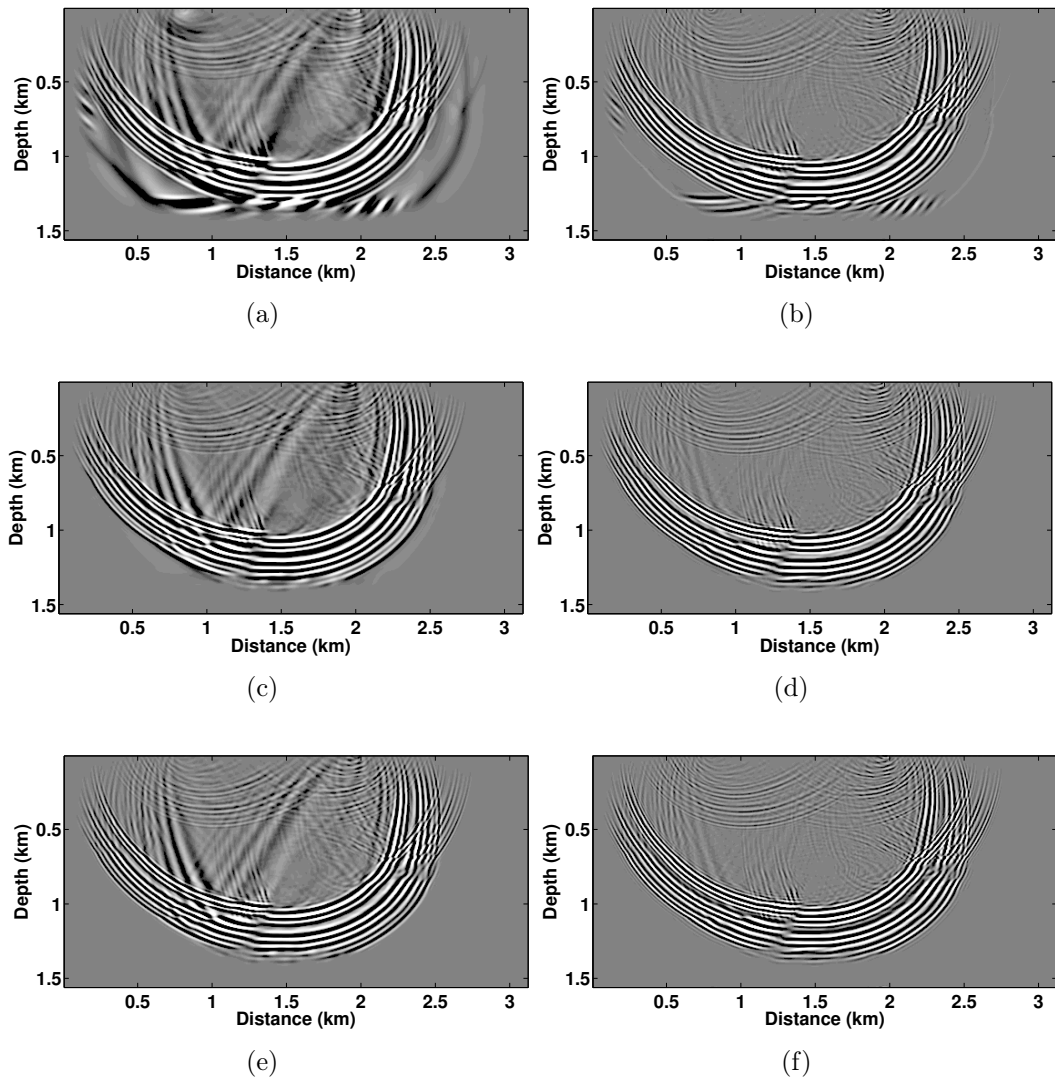


Figure 5.7: The same migration responses as in Figure 5.6 except the source wavelet was not integrated.

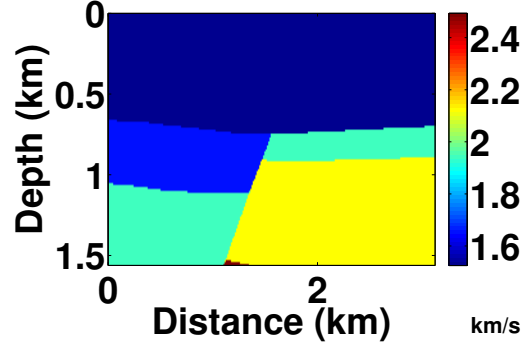


Figure 5.8: vpp

#### 5.4.1 Migration aliasing

In the cross-correlation imaging condition the back propagated receiver field  $R(t, \vec{x})$  is cross-correlated at zero lag with the forward propagated shot field  $S(t, \vec{x})$ . The simplest imaging condition is

$$I(\vec{x}) = \int_0^T S(t, \vec{x}) R(t, \vec{x}) dt, \quad (5.14)$$

for a shot record of length  $T$ . By Parsavel's theorem, the imaging condition in the time domain is equivalent to the imaging condition in the frequency domain used by wavefield continuation migrations,

$$I(\vec{x}) = \int_0^{\omega_{max}} S(\omega, \vec{x}) R(\omega, \vec{x}) d\omega. \quad (5.15)$$

The receiver and shot field spatial sampling is  $\delta x$ . The Nyquist frequency for any component of the wavenumber is  $|k_{x_i}| = \pi/2\delta x$ . The largest wavenumber of the crosscorrelated fields will be double the maximum in either shot or the receiver field Zhang et al. (2003). Alternatively, by equation (5.14) in the wavenumber domain is

$$I(\vec{k}) = \int_0^T S(t, \vec{k}) * R(t, \vec{k}) dt, \quad (5.16)$$

where  $*$  denotes convolution in the wavenumbers. Let the maximum frequency be  $f_{max}$  and the minimum velocity be  $c_{min}$  then the maximum wavenumber is  $k_{max} = 2f_{max}/c_{min}$ .

Since  $R(t, \vec{k})$  and  $S(t, \vec{k})$  are multiplied in the wavenumber domain, the maximum frequency in the image I will be doubled that in  $R$  or  $S$ . Therefore, to avoid aliasing  $R(t, \vec{k})$  and  $S(t, \vec{k})$  are sampled at half the Nyquist frequency sampling rate.

## 5.5 Discussion

We now look at a few migration impulse responses to better understand migration aliasing. In the first example a constant  $2000m/s$  velocity was used. The migration trace is a far offset trace with 5 Ormsby wavelets with a maximum frequency of  $60Hz$  and the grid spacing is  $12m$ . Figure 5.1(a) is the impulse response of a single trace to reverse-time migration with the shot and receiver field resampled to half of the Nyquist. Figure 5.1(b) is the same impulse response however there was no resampling done and the migrated image has aliasing.

## 5.6 Conclusions

We presented an aliasing condition for the imaging condition in reverse-time migration. If the shot field and back-propagated receiver field has spatial frequencies up to the Nyquist then it is necessary to resample these fields to half the Nyquist prior to the application of the imaging condition.

# Chapter 6

## Converted waves

The PP image migrated with a RTM with a good velocity estimate is often an excellent structural image of the earth. Well logging and AVO analysis can provide rock properties to supplement the structural image. However, AVO analysis is ill posed to determine rock properties like lithology, porosity, fluid content, permeability, and fracture characteristics from P-wave seismic data and well logging data alone. Converted wave data can be used to constrain the rock properties and improve hydrocarbon detection using AVO and AVAZ (Goodway et al., 2010) and joint full wave inversion (Kamath and Tsvankin, 2013). In rare circumstances imaging beneath a gas cloud the PS image is better than the PP image.

Multi-component seismic data is a record of the three components of displacement. On land, it is called 3C data. In an OBC or OBN survey the pressure field is also recorded and it is referred to as 4C data. The speed of propagation in anisotropic media is sensitive to the direction of propagation. The S-wave components typically are more sensitive to anisotropy than the P-wave component. The S-wave component also exhibits behavior that the P-wave does not. In an anisotropic media, S-wave splitting causes the S-wave component to break into two modes with distinct velocity and polarization. S-wave splitting analysis is an important diagnostic tool for determining anisotropic parameters \*\*\*reference.

Converted waves (C-waves) are P-waves that converted to S-wave on reflection or transmission, or vice versa. The migrated image of a P-wave converted into a S-wave is called the PS-image, and a migrated reflectivity image of an S-wave converted into a P-wave is the SP-image. Converted waves are imaged through elastic RTM or through wavefield separation at the surface treating converted waves by acoustical wave propagation approximations.

### 6.1 Elastic reverse-time migration

Elastic RTM back-propagates the multi-component seismic wavefield and forward propagates the shot field with the elastic wave equation. Although computationally expensive, the elastic wave equation accurately models all the wave mode conversions and amplitudes and kinematics correctly provide an accurate model of the elastic parameters can be determined.

As in acoustic RTM, the recorded wavefield  $\mathbf{R}(t, \vec{x})$  is back-propagated and the source  $\mathbf{S}(t, \vec{x})$  wavefield is forward propagated. A simple zero-lag crosscorrelation vector imaging condition condition is,

$$I(\vec{x}) = \int \mathbf{S}(t, \vec{x}) \cdot \mathbf{R}(t, \vec{x}) dt \quad (6.1)$$

Since both wavefields contain P-waves and S-waves, the image will contain PP, PS, SP, and SS reflections. Since all of these images will be slightly mis-positioned due p-wave velocity and S-wave velocity errors, the image will be difficult to interpret. Therefore, it is necessary to decompose the wavefields into P-wave and S-wave components at each time step. hen generate images for the different types of refections. For isotropic media this can be done by Helmholtz decomposition by the application of the curl and divergence operator to the wavefields. In anisotropic elastic media, wavefield separation is more difficult. A simple curl and divergence does not separate the wavefields completely \*\*\*referece.

## 6.2 Shear wave splitting

## 6.3 Geophone orientation

## 6.4 Wavefield separation at the surface

Back propagation into an Isotropic layer

- slant stacking
- up/down separation
- Yan and Sava (2009)
- hydrophone

## 6.5 Conversion point determination

- Determined by ray tracing
- asymptotic conversion Point.
- Most exact formulas
- CIG methods

## 6.6 Reciprocity for converted waves

Reciprocity for the acoustic wave equation means that if geophone and source are interchanged the same trace is be recorded. In practice this is approximately true

because of nonlinear effects near the shot location and the fact the geophones are recorded on the surface and shots are often located below the watertable at 5-25m below the surface. The reciprocity relation for elastic wave equation Arntsen and Carcione (2000) is more complicated because it depends on the type of source and orientation of source or geophone.

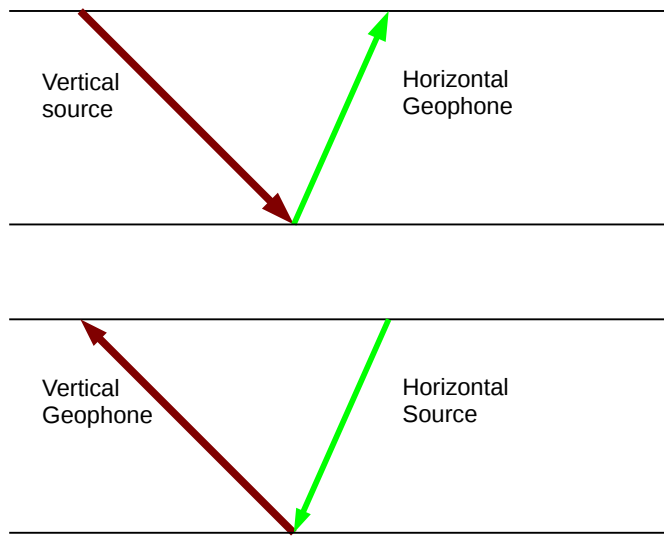


Figure 6.1: A statement of reciprocity.

Seismic data recorded with OBC geometry typically undersamples the wavefield for shot-profile migration. It is therefore desirable to use the principle of reciprocity for the elastic wave equation. This treats common receiver or node gathers as if there were from a horizontal shear shot located at the bottom of the ocean at the location of the node.

Figure 6.2 is the image of a shot gather and a node gather for a 2D synthetics dataset generated by CGGVeritas. The node spacing 100m and the shot spacing is 12.5m. As a result, the shot gather is aliased.

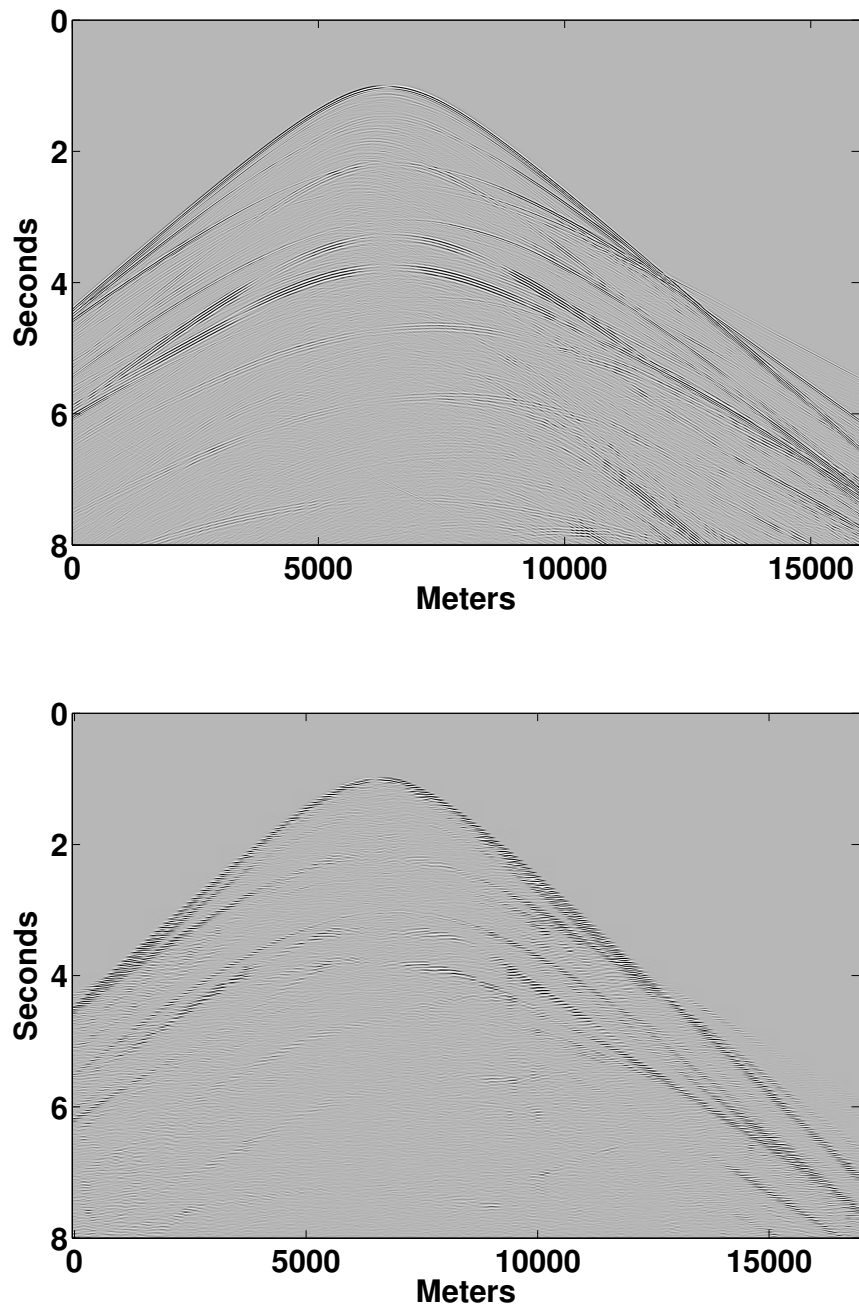


Figure 6.2: Top: A node gather for the OBC CCGVeritas dataset for the vertical geophone. Bottom: A shot gather for the CGGVeritas dataset for the vertical geophone.

## 6.7 Converted wave imaging

# Chapter 7

## Migration results

### 7.1 Migration of the Marmousi data set

The Marmousi dataset (Versteeg, 1994) is a modelled seismic data set used to benchmark migration and velocity building algorithms. Although it does not showcase the strengths of RTM, e.g. the imaging of overturned reflectors, it does show that PSTS RTM can image seismic data in a complex medium where multipathing is present. To benchmark PSTS RTM we compare it to a second-order time and fourth-order space finite-difference RTM and a higher-order pseudospectral method. The PSTS method uses equation (3.39) with two reference velocities. Figure 7.1 is a comparison of forward modelling using the PSTS algorithm and a second-order finite-difference algorithm. The accuracy when using four reference velocities is better than using two reference velocities. The numerical noise is greater in the finite-difference solution and there are subtle differences in dispersive errors along the wavefronts.

Figures 7.2 and 7.3 are the PSTS prestack depth migration results and Figure 7.4 and 7.5 are the finite-difference results. Figure 7.6 is the result using higher-order pseudospectral method. The PSTS and pseudospectral RTM are calculated using a coarser spatial grid and a larger time step than the finite-difference method. Finer sampling improves crosscorrelation imaging condition. To prevent spatial aliasing the shot field and receiver field are resampled to a smaller grid spacing before applying the imaging condition. Table 7.1 is the computation times, the grid spacing size, and the time step size.

Figure 7.7 is the vertical P-wave reflectivity for a VTI model made by Hess. The Hess synthetic seismic dataset was generated using a pseudo-acoustic wave equation with a VTI velocity model. The reflection energy in Figure 7.8 compares to the P-wave reflectivity. There is a significant amount of noise caused by migration artifacts.

The FRP ramp model is migrated to demonstrate imaging through a medium with anisotropic overburden. The ramp model has three layers. The top layer is a homogeneous TTI medium while the lower layers are isotropic. Figure 7.9 is the vertical velocity. Figure 7.10 is a migrated image of the vertical component. No attempt was made to separate the P-wave energy from the S-wave energy on the vertical component and the S-data is visible on the PP section. The ramp is correctly located.

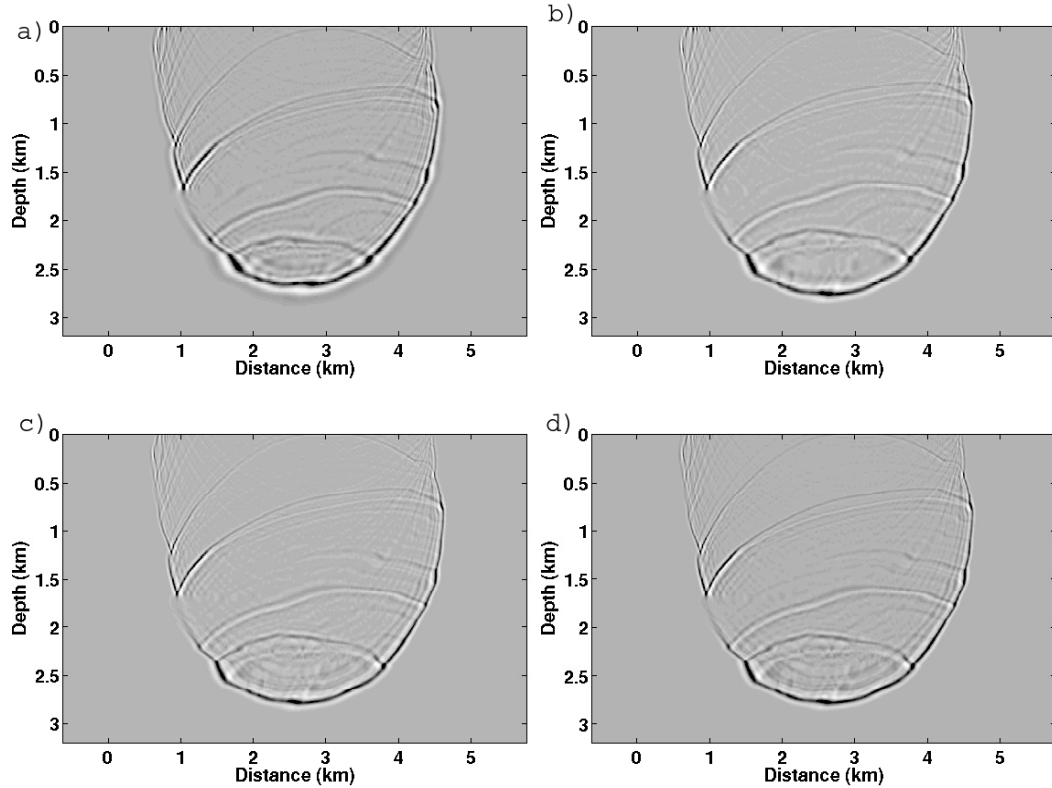


Figure 7.1: (a) A snapshot during forward propagation with the Marmousi velocity model using equation (3.37) with a minimum phase wavelet injected at the surface using 2 reference velocities with a time step of  $1.5ms$ , and a grid-spacing of  $12.5m$ . (b) The same snapshot as (a) but with 4 reference velocities. (c) A snapshot using second-order time and fourth-order space FD solver with a time step of  $0.295ms$  and grid spacing of  $5m$ . (d) Similar to (c) but with a time step of  $0.195ms$  and grid spacing of  $5m$ .

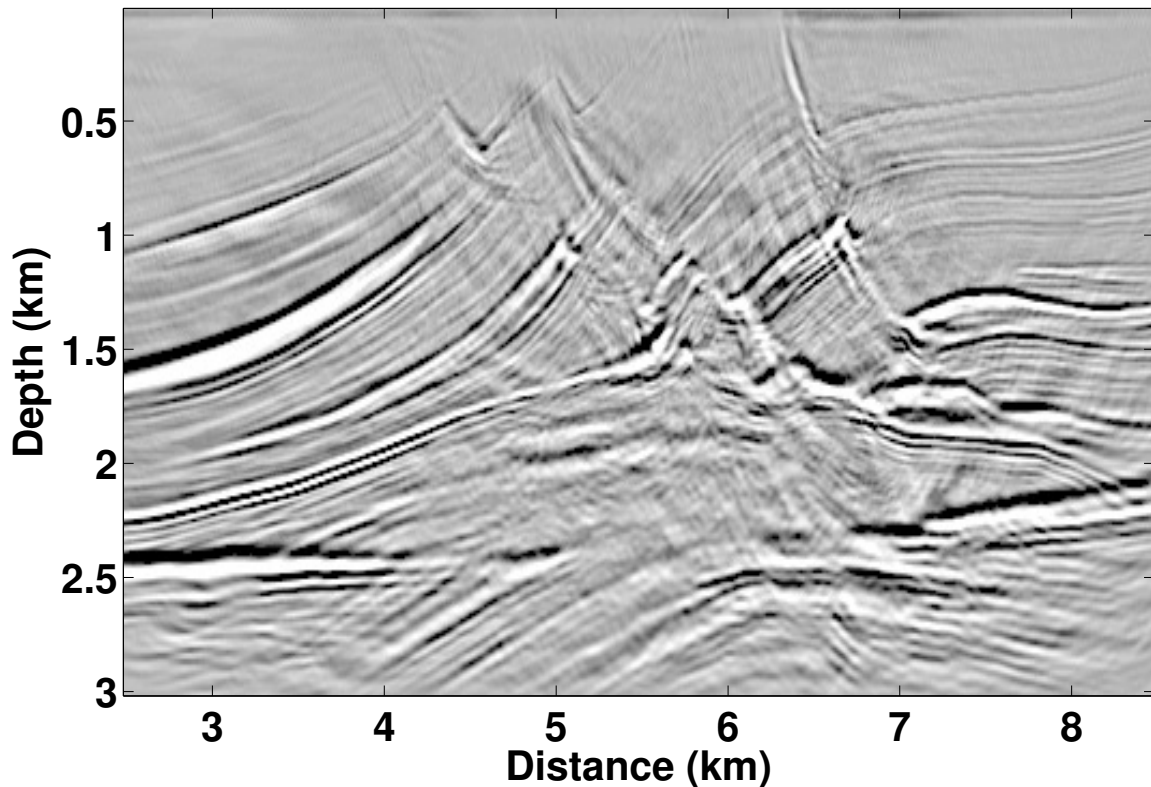


Figure 7.2: An image of the Marmousi data set using PSTS RTM with 4 reference velocities. The image is the stack of 240 migrated shot records. The time step was 0.0015ms and the grid spacing was 12.5m. The grid spacing for the crosscorrelation is 3.13m.

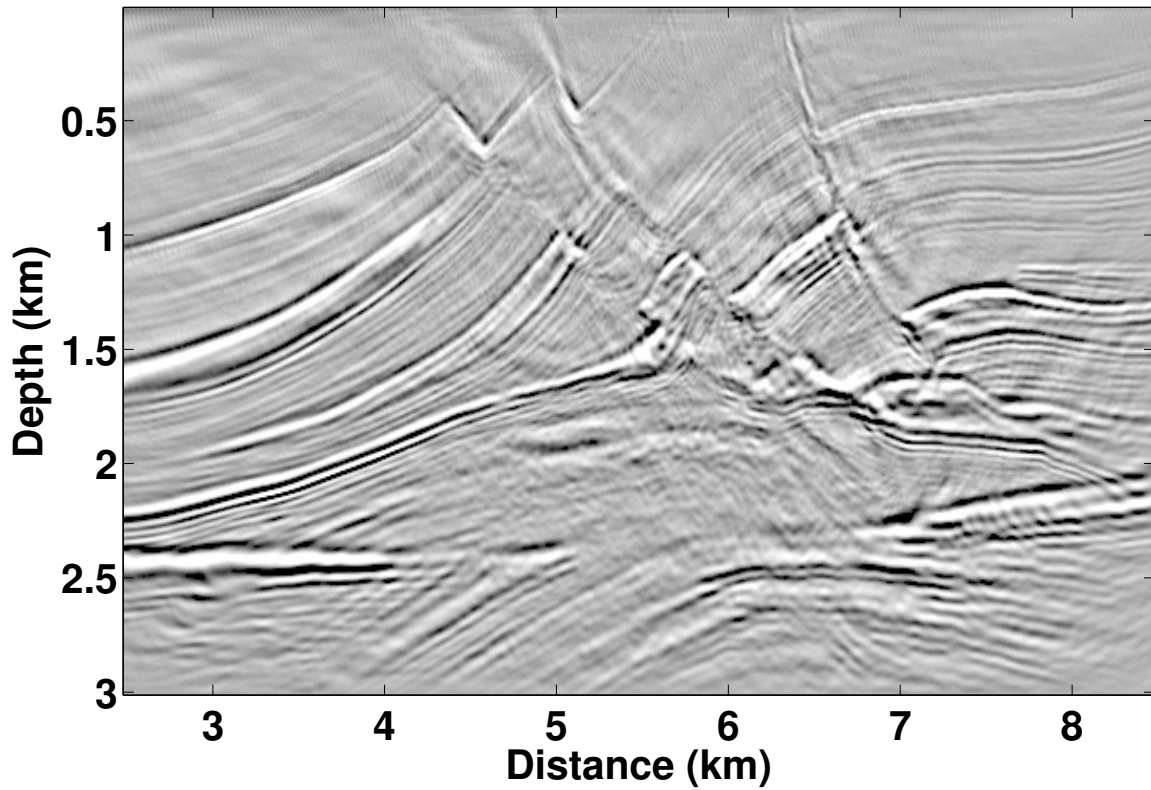


Figure 7.3: An image the Marmousi data set using PSTM RTM with 4 reference velocities. The time step was 0.0015ms and the grid spacing was 8.3m. The imaging condition grid sampling is 4.15m.

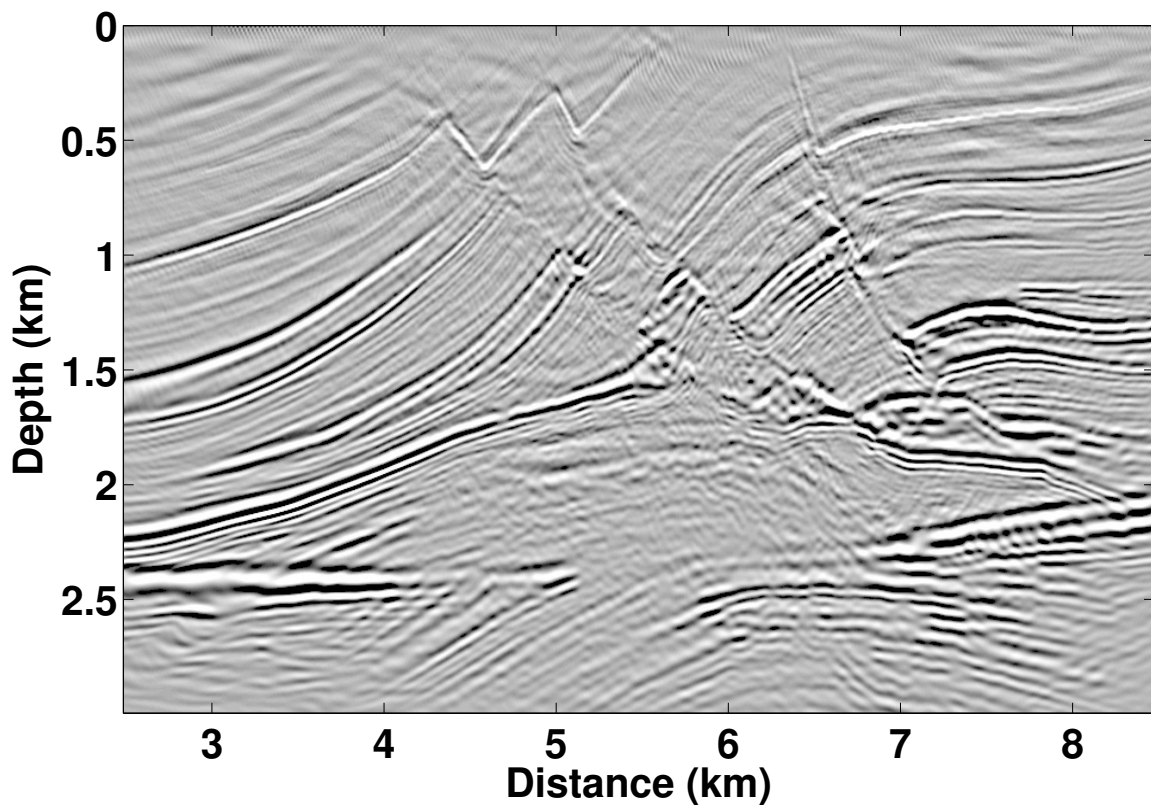


Figure 7.4: A RTM of the Marmousi data set using a second-order time and fourth-order space explicit FD solver. The time step was .46ms and the grid spacing was 5m.

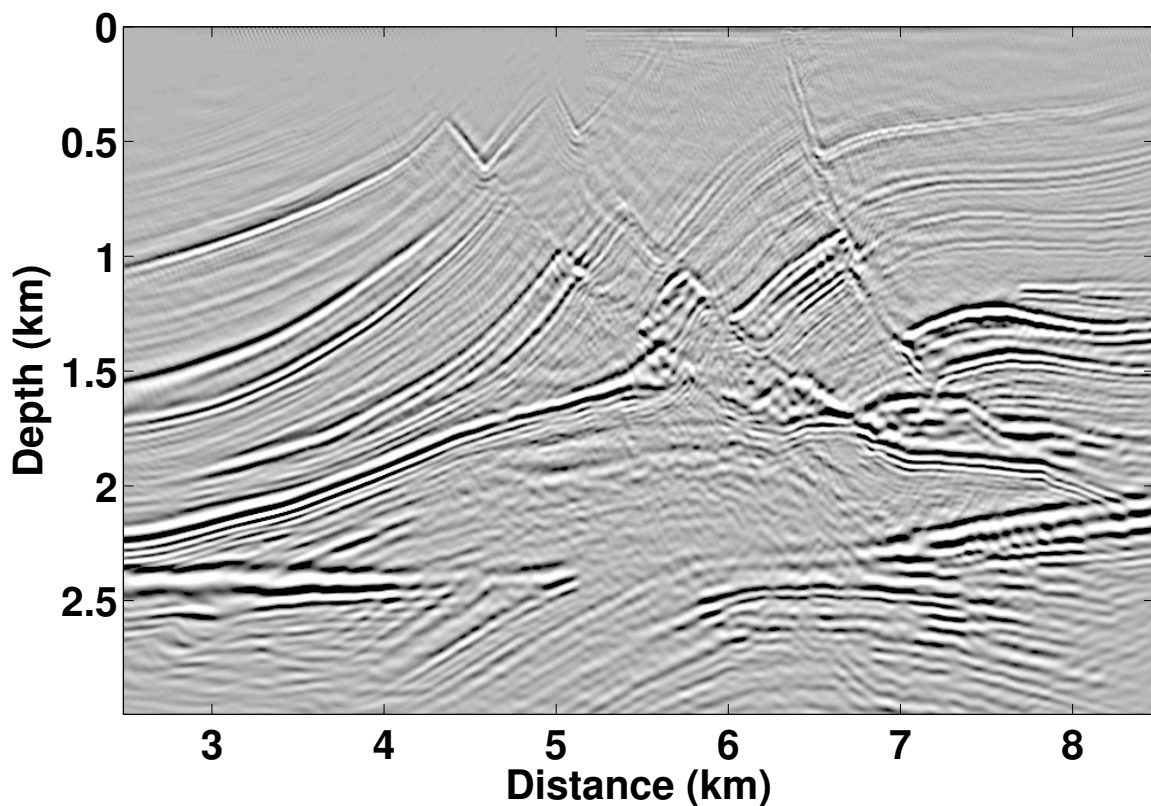


Figure 7.5: Similar to Figure 7.4 except the time step was halved and therefore the computational time doubled.

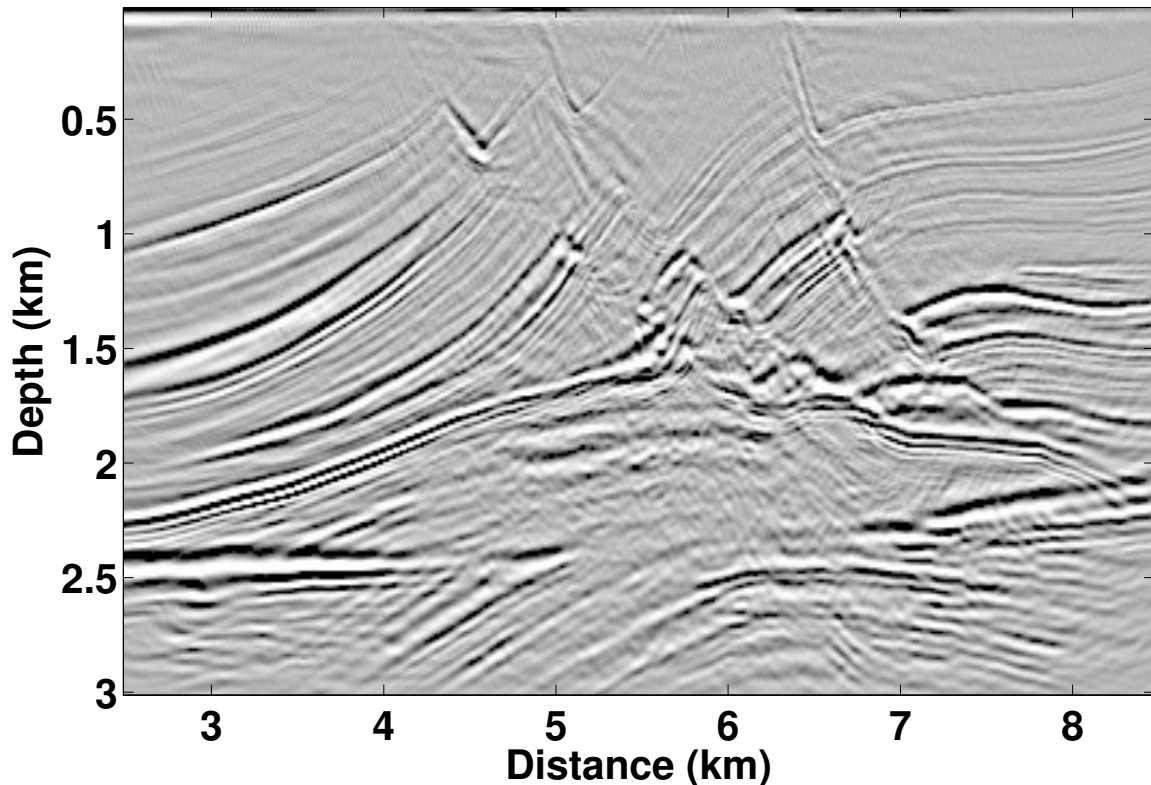


Figure 7.6: A fourth-order in time Lax-Wendroff pseudospectral RTM of the Marousi dataset. The size of the grid is 12.5m and the size of the time step is 1.5ms. The crosscorrelation grid spacing is 6.25m.

| Figure | Time<br>(s) | Time step<br>(ms) | Grid<br>Spacing (m) | Imaging Condition<br>Grid Spacing (m) |
|--------|-------------|-------------------|---------------------|---------------------------------------|
| 7.1(a) | 21          | 1.5               | 5                   |                                       |
| 7.1(b) | 42          | 1.5               | 5                   |                                       |
| 7.1(c) | 1282        | 0.295             | 12.5                |                                       |
| 7.1(d) | 866         | 0.197             | 12.5                |                                       |
| 7.2    | 946         | 1.5               | 12.5                | 3.13                                  |
| 7.3    | 1530        | 0.98              | 8.33                | 4.16                                  |
| 7.4    | 1530        | 0.46              | 5                   | 5                                     |
| 7.5    | 2930        | 0.23              | 5                   | 5                                     |
| 7.6    | 399         | 1.5               | 12.5                | 6.25                                  |

Table 7.1: Computation time, time step size, and grid-sizes used to calculate the figures in this chapter.

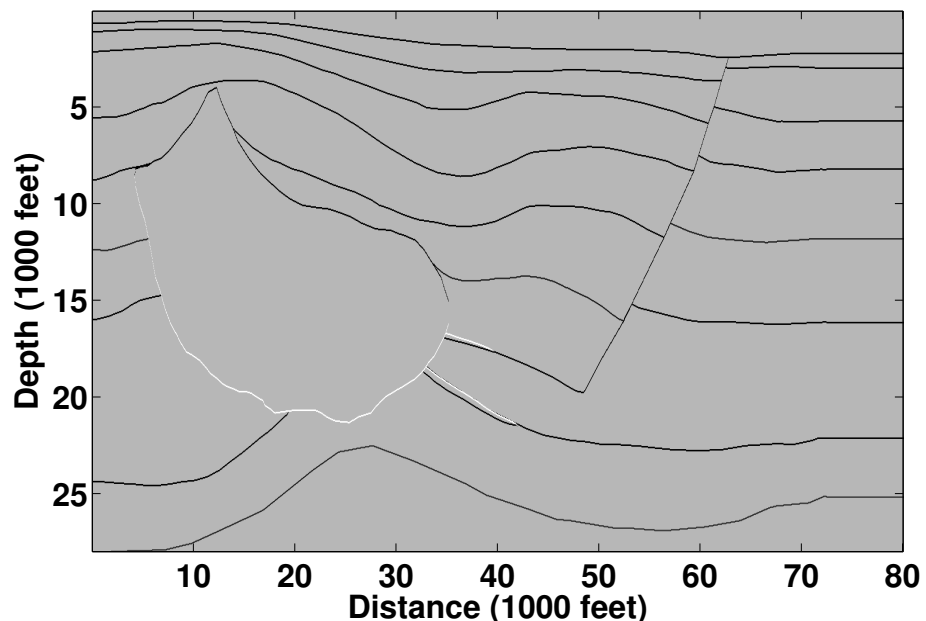


Figure 7.7: PP reflectivity for the HESS velocity model.

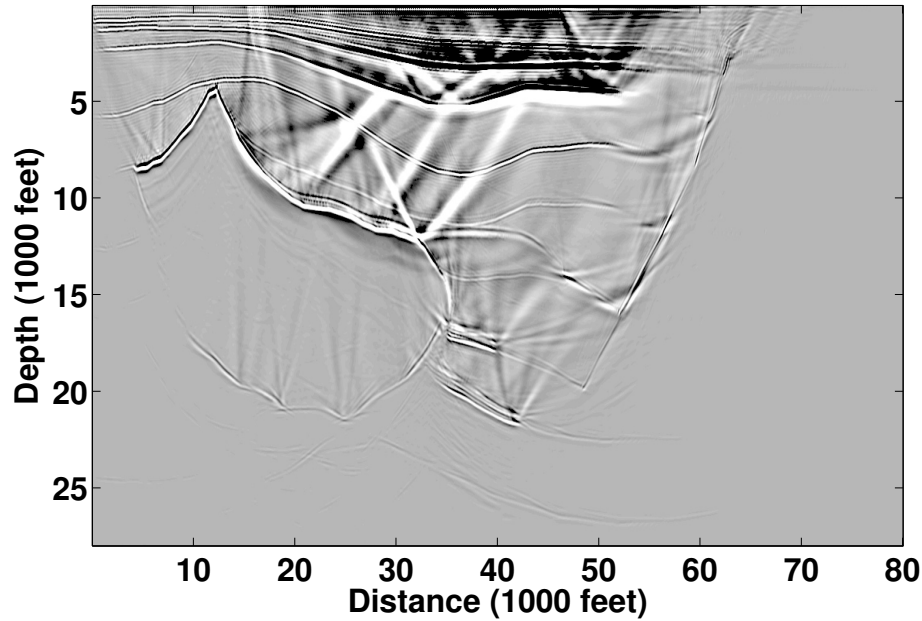


Figure 7.8: A migrated image of the Hess VTI data set using a VTI RTM.

A simple ray tracing model of a flat reflector with OBC geometry was created to test converted wave RTM imaging. Figure 7.11 (a) displays the ray path of the node gather. The node is located at depth of 1000m, and the shots are located along the sea surface at a depth of 10m. Figure 7.11 (b) is a node gather made with ray tracing. In a true converted wave experiment the zero offset trace would be zero. Figure 7.11 (c) is the migrated image of the PP data for a single shot record. It is correctly imaged. Figure 7.11 (d) is the migrated image using RTM of the converted wave PS data. The converted wave image is higher frequency than the P-wave image because the shear-wave velocity is half the P-wave velocity.

An elastic 2D OBC synthetic data set was obtain from CGGVeritas. This data set is used to benchmark a PP OBC RTM.

7.12

7.13

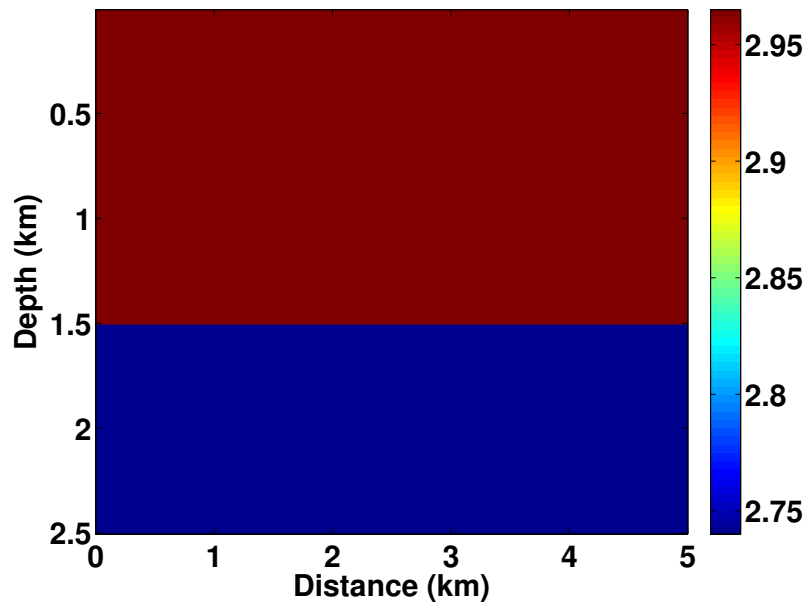


Figure 7.9: Vertical P-wave velocity of the FRP ramp model. The ramp has been flooded with the velocity above it. The overburden has a value of  $V_p = \epsilon = 0.196$ ,  $\delta = 0$ , and tilt angle of  $\beta = 45^\circ$ . The lower velocity layer is isotropic.

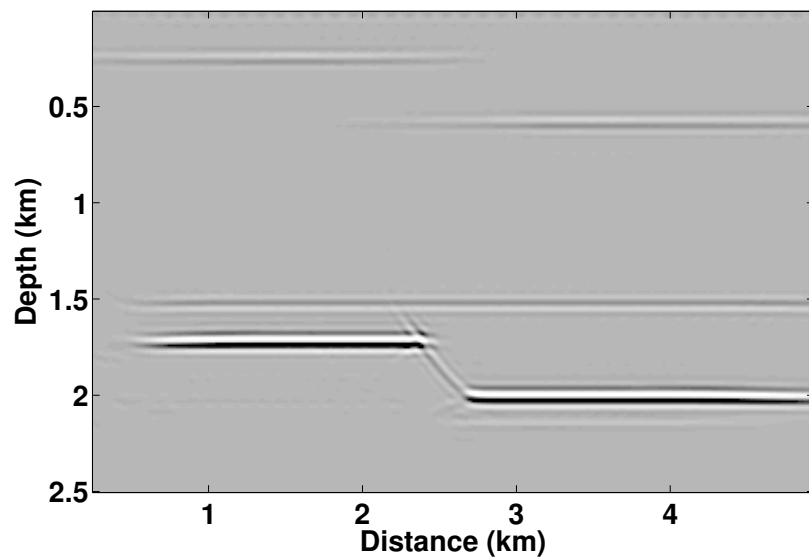


Figure 7.10: A migrated image of the PP data for the FRP ramp model which has TTI overburden.

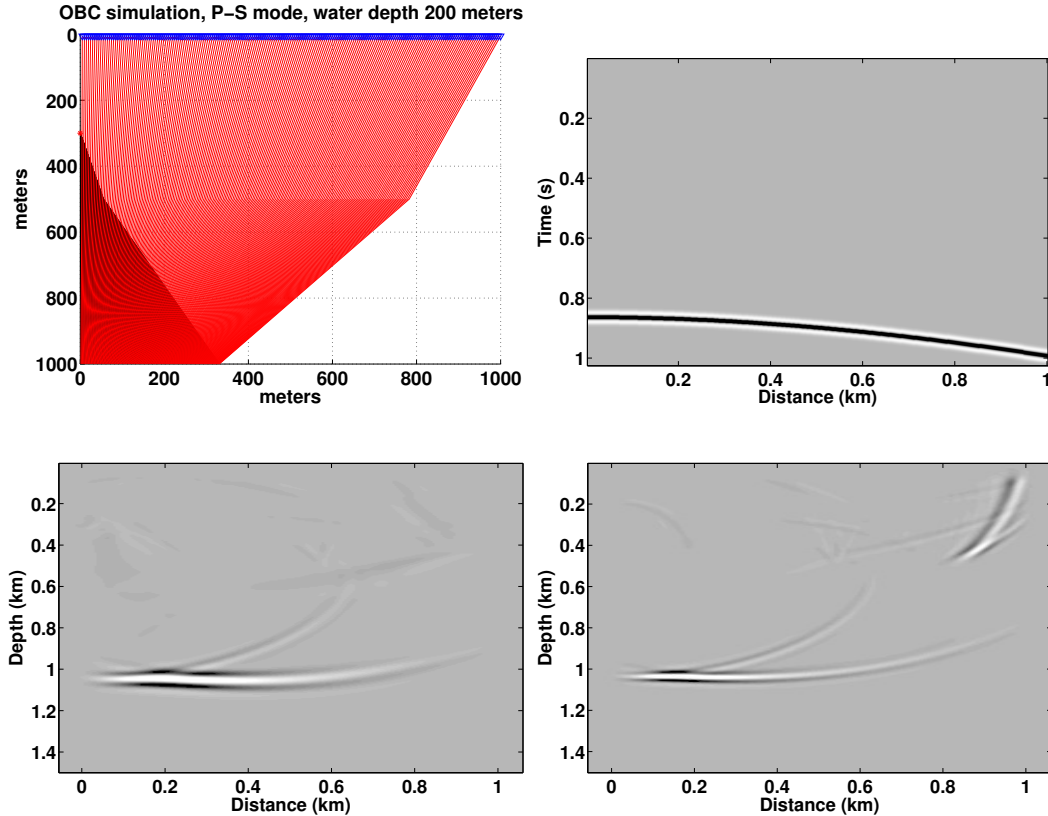


Figure 7.11: OBC PP and PS imaging of synthetic data set made with ray tracing. The amplitudes are constant on the reflection. (a) An ocean bottom cable geometry (OBC) with an S-wave source. This is kinematically equivalent to a node gather. (b) PS synthetic data, made with constant amplitude. (c) PP image of a migrated shot made with travel times only. (d) PS image of a migrated shot made with travel times only.

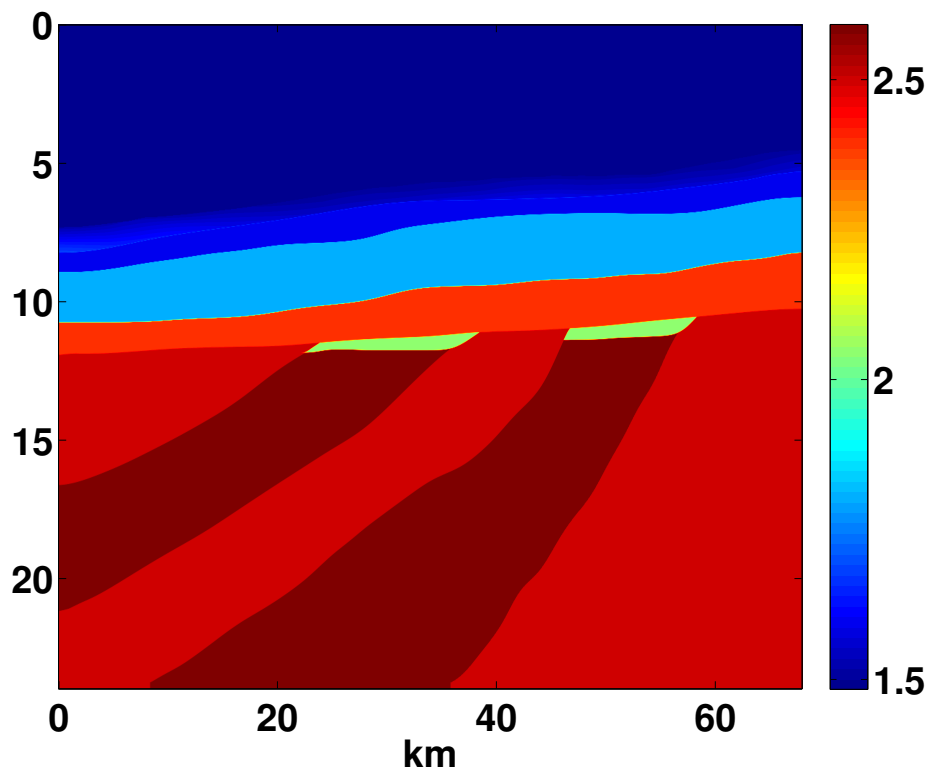


Figure 7.12: The P-wave velocity of an OBC dataset provide by CCGVeritas. The units of the velocity are in  $m/s$ .

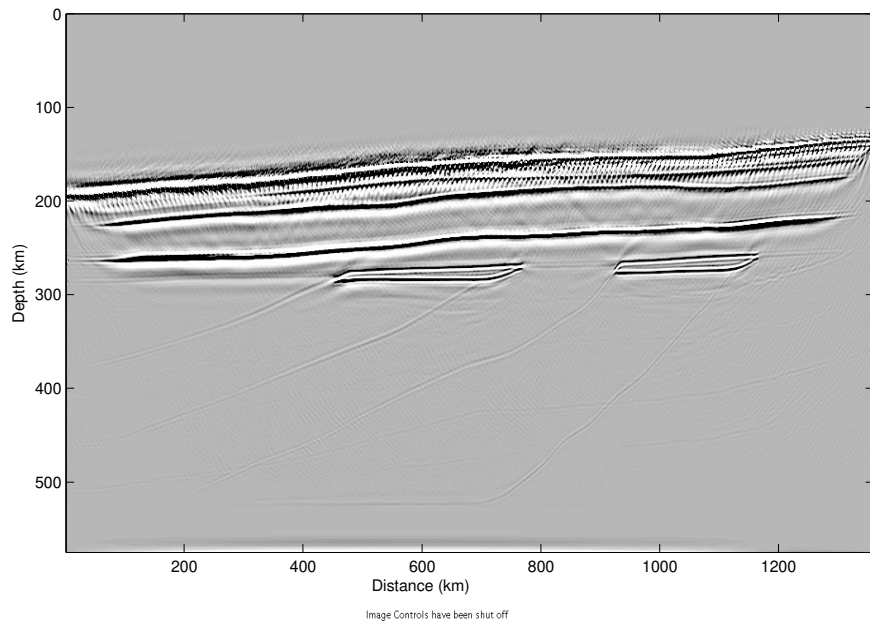


Figure 7.13: A migrated image of an ocean bottom cable (OBC) dataset obtained from CGGVeritas. The velocity model is isotropic. The node spacing on the seabed surface is 100m and the shot spacing is 12.5m. The dataset was generated with an elastic wave equation.

# Bibliography

- Aki, K., and P. Richards, 2002, Quantitative seismology: University Science Books.
- Alkhalifah, T., 2000, An acoustic wave equation for anisotropic media: *Geophysics*, **65**.
- Arntsen, B., and J. Carcione, 2000, A new insight into the reciprocity principle: *GEOPHYSICS*, **65**, 1604–1612.
- Audebert, F., D. Nichols, T. Rekdal, B. Biondi, D. Lumley, and H. Urdaneta, 1997, Imaging complex geologic structure with single arrival Kirchhoff prestack depth migration: *Geophysics*, **62**, 1533–1543.
- Auld, B., 1973, Acoustic fields and waves in solids: Wiley, New York.
- Backus, G. E., 1962, Long-wave elastic anisotropy produced by horizontal layering: *J. Geophys. Res.*, **67**.
- Bagaini, C., E. Bonomi, and E. Pieroni, 1995, Data parallel implementation of 3-D PSPI: 65nd Ann. Internat.Mtg., Soc. Expl. Geophys., Expanded Abstracts,, 188-191.
- Bakulin, A., V. Grechka, and I. Tsvankin, 2000, Estimation of fracture parameters from reflection seismic data-part I: HTI model due to a single fracture set: *Geophysics*, **65**.
- Baysal, E., D. D. Kosloff, and J. W. C. Sherwood, 1983, Reverse time migration: *Geophysics*, **48**.
- Billette, F., and S. Brandsberg-Dahl, 2005, The 2004 BP velocity benchmark: 67th annual international meeting: EAGE Technical Program Expanded Abstracts, **67**.
- Biondi, B., 2001, Kirchhoff imaging beyond aliasing: *Geophysics*, **66**.  
———, 2006, 3D seismic imaging: Society of Exploration.
- Bleistein, N., J. Cohen, and J. Stockwell, 2000, Mathematics of multidimensional seismic imaging migration and inversion: Springer.
- Boyd, J. P., 1989, Chebyshev and Fourier Spectral Methods: Springer-Verlag.
- Candès, E., L. Demanet, and L. Ying, 2007, Fast computation of Fourier integral operators: *SIAM J. Sci. Comput.*, **29**, 2464–2493.
- Carcione, J. J. M., 2007, Wave fields in real media: Wave propagation in anisotropic, anelastic, porous and electromagnetic media: Elsevier Science.

- Carcione, J. M., G. C. Herman, and A. P. E. ten Kroode, 2002, Seismic modeling: *Geophysics*, **67**, 1304–1325.
- Cary, P., and C. Zhang, 2010, Technical considerations for converted wave prestack time migration: SEG Technical Program Expanded Abstracts 2010, **327**, 1656–1660.
- Cerjan, C., D. Kosloff, R. Kosloff, and M. Reshef, 1985, A nonreflecting boundary condition for discrete acoustic and elastic wave equations: *Geophysics*, **50**, 705–708.
- Chang, W.-F., and G. A. McMechan, 1986, Reverse-time migration of offset vertical seismic profiling data using the excitation-time imaging condition: *Geophysics*, **51**, 67–84.
- , 1987, Elastic reverse-time migration: *Geophysics*, **52**, 1365–1375.
- Chattopadhyay, S., and G. A. McMechan, 2008, Imaging conditions for prestack reverse-time migration: *Geophysics*, **73**, S81–S89.
- Chen, J.-B., 2007, High-order time discretizations in seismic modeling: *Geophysics*, **72**, SM115–SM122.
- Claerbout, J. F., 1971, Toward a unified theory of reflector mapping: *Geophysics*, **36**, 467–481.
- Clayton, R., and B. Engquist, 1977, Absorbing boundary conditions for acoustic and elastic wave equation: *Bull., Seis. Am.*, **67**.
- Cohen, G. C., 2001, Higher-order numerical methods for transient wave equations: Springer Verlag.
- Crampin, S., 1981, A review of wave motion in anisotropic and cracked elastic-media: *Wave Motion*, **3**.
- , 1985, Evaluation of anisotropy by shear-wave splitting: *Geophysics*, **50**, 142–152.
- Dablain, M. A., 1986, The application of high-order differencing to the scalar wave equation: *Geophysics*, **51**, 54–66.
- de Hoop, M. V., J. H. L. Rousseau, and R.-S. Wu, 2000, Generalization of the phase-screen approximation for the scattering of acoustic waves: *Wave Motion*, **31**, 43–70.
- Etgen, J., S. Gray, and Y. Zhang, 2009, An overview of depth imaging in exploration geophysics: *GEOPHYSICS*, **74**, WCA5–WCA17.
- Etgen, J. T., and S. Brandsberg-Dahl, 2009, The pseudo-analytical method: Application of pseudo-laplacians to acoustic and acoustic anisotropic wave propagation: SEG Technical Program Expanded Abstracts, **28**, 2552–2556.
- Etgen, J. T., and J. Dellinger, 1989, Accurate wave-equation modeling: SEG Technical Program Expanded Abstracts, **8**.
- Fletcher, R. P., X. Du, and P. J. Fowler, 2009, Reverse time migration in tilted transversely isotropic (TTI) media: *Geophysics*, **74**.
- Fletcher, R. P., P. J. Fowler, P. Kitchenside, and U. Albertin, 2006, Suppressing

- unwanted internal reflections in prestack reverse-time migration: *Geophysics*, **71**, E79–E82.
- Fliedner, M., and D. Bevc, 2008, Automated velocity model building with wavepath tomography: *GEOPHYSICS*, **73**, VE195–VE204.
- Fowler, P., 2003, Practical VTI approximations: a systematic anatomy: *Journal of Applied Geophysics*, **54**.
- Furumura, T., B. L. N. Kennett, and H. Takenaka, 1998, Parallel 3-D pseudospectral simulation of seismic wave propagation: *Geophysics*, **63**, 279–288.
- Gabor, D., 1946, Theory of communication: *Journal of the Institute of Electrical Engineers*, **93**, 429–457.
- Gazdag, J., 1978, Wave equation migration with the phase-shift method: *Geophysics*, **43**, 1342–1351.
- Gazdag, J., and P. Sguazzero, 1984, Migration of seismic data by phase shift plus interpolation: *Geophysics*, **49**, 124–131.
- Goodway, B., M. Perez, J. Varsek, and C. Abaco, 2010, Seismic petrophysics and isotropic-anisotropic avo methods for unconventional gas exploration: *The Leading Edge*, **29**, 1500–1508.
- Gray, S., 2005, Gaussian beam migration of common-shot records: *Geophysics*, **70**, S71–S77.
- Gray, S. H., 1992, Frequency-selective design of the Kirchhoff migration operator: *Geophysical Prospecting*, **40**.
- Gray, S. H., J. Etgen, J. Dellinger, and D. Whitmore, 2001, Seismic migration problems and solutions: *Geophysics*, **66**, 1640.
- Grechka, V., A. Bakulin, and I. Tsvankin, 2003, Seismic characterization of vertical fractures described as general linear-slip interfaces: *Geophysical Prospecting*, **51**.
- Grechka, V., L. Zhang, and J. W. Rector III, 2004, Shear waves in acoustic anisotropic media: *Geophysics*, **69**, 576–582.
- Grossman, J., G. Margrave, and M. P. Lamoureux, 2002, Constructing adaptive, nonuniform Gabor frames from partitions of unity: CREWES Research Report 14.
- Guitton, A., B. Kaelin, and B. Biondi, 2007, Least-squares attenuation of reverse-time-migration artifacts: *Geophysics*, **72**, S19–S23.
- Hagedoorn, J. G., 1954, A process of seismic refection interpretation: *Geophysical Prospecting*, **2**.
- Hill, N., 1990, Gaussian beam migration: *Geophysics*, **55**, 1416–1428.
- , 2001, Prestack gaussian-beam depth migration: *Geophysics*, **66**, 1240–1250.
- Jones, I. F., M. C. Goodwin, I. D. Berranger, H. Zhou, and P. A. Farmer, 2007, Application of anisotropic 3D reverse time migration to complex north sea imaging: SEG Technical Program Expanded Abstracts, **26**, 2140–2144.
- Kamath, N., and I. Tsvankin, 2013, Full-waveform inversion of multicomponent data for horizontally layered vti media: *GEOPHYSICS*, **78**, WC113–WC121.

- Liu, F., G. Zhang, S. A. Morton, and J. P. Leveille, 2011, An effective imaging condition for reverse-time migration using wavefield decomposition: *Geophysics*, **76**, S29–S39.
- Ma, Y., and G. F. Margrave, 2008, Seismic depth imaging with the Gabor transform: *Geophysics*, **73**, S91–S97.
- Margrave, G., and M. Lamoureux, 2002, Gabor deconvolution: CSEG annual mtg., Expanded Abstract.
- Margrave, G. F., 1998, Theory of nonstationary linear filtering in the Fourier domain with application to time-variant filtering: *Geophysics*, **63**, 244–259.
- Margrave, G. F., and R. J. Ferguson, 1999, Wavefield extrapolation by nonstationary phase shift: *Geophysics*, **64**, 1067–1078.
- Margrave, G. F., P. C. Gibson, J. P. Grossman, D. C. Henley, V. Iliescu, and M. P. Lamoureux, 2005, The Gabor transform, pseudodifferential operators, and seismic deconvolution: *Integr. Comput.-Aided Eng.*, **12**, 43–55.
- McMechan, G. A., 1983, Migration by extrapolation of time-dependent boundary values: *Geophysical Prospecting*, **31**, 413–420.
- Mulder, W. A., and R.-E. Plessix, 2004, A comparison between one-way and two-way wave-equation migration: *Geophysics*, **69**, 1491–1504.
- Ng, M., 2007, Using time-shift imaging condition for seismic migration interpolation: SEG Technical Program Expanded Abstracts, **26**.
- Pedersen, O., B. Ursin, and H. Helgesen, 2010, One-way wave-equation migration of compressional and converted waves in a vti medium: *GEOPHYSICS*, **75**, S237–S248.
- Rietveld, W., and A. Berkhouit, 1994, Prestack depth migration by means of controlled illumination: *GEOPHYSICS*, **59**, 801–809.
- Sava, P., and S. Fomel, 2005, Riemannian wavefield extrapolation: *GEOPHYSICS*, **70**, T45–T56.
- Schneider, W., 1978, Integral formulation for migration in two and three dimensions: *Geophysics*, **43**, 49–76.
- Schuster, G. T., 2002, Reverse-time migration = generalized diffraction stack migration: SEG Technical Program Expanded Abstracts, **21**.
- Shearer, P. M., 2009, Introduction to seismology: Cambridge University Press.
- Shragge, J., 2008, Riemannian wavefield extrapolation: Nonorthogonal coordinate systems: *GEOPHYSICS*, **73**, T11–T21.
- Snieder, R., 2002, General theory of elastic wave scattering in scattering and inverse scattering in pure and applied science: Academic Press.
- Sommerfeld, A., 1964, Lectures on theoretical physics: Thermodynamics and statistical mechanics: Academic Press.
- Song, X., and S. Fomel, 2010, Fourier finite-difference wave propagation: SEG Technical Program Expanded Abstracts, **29**, 3204–3209.

- Soubaras, R., and Y. Zhang, 2008, Two-step explicit marching method for reverse time migration: SEG Technical Program Expanded Abstracts, **27**, 2272–2276.
- Stein, E., 1993, Harmonic analysis : real-variable methods, orthogonality, and oscillatory integrals: Princeton University Press.
- Stoffa, P. L., J. T. Fokkema, R. M. de Luna Freire, and W. P. Kessinger, 1990, Split-step Fourier migration: *Geophysics*, **55**.
- Stolt, R. H., 1978, Migration by Fourier transform: *Geophysics*, **43**, 23–48.
- Symes, W. W., 2007, Reverse time migration with optimal checkpointing: *Geophysics*, **72**, SM213–SM221.
- Tal-Ezer, H., 1986, Spectral methods in time for hyperbolic equations: *SIAM J. Numer. Anal.*, **23**, 11–26.
- Thomsen, L., 1986, Weak elastic anisotropy: *Geophysics*, **51**, 1954–1966.
- Tsvankin, I., 2001, Seismic signatures and analysis of reflection data in anisotropic media: Elsevier.
- Versteeg, R., 1994, The Marmousi experience; velocity model determination on a synthetic complex data set: *The Leading Edge*, **13**, 927–936.
- Wards, B. D., G. F. Margrave, and M. P. Lamoureux, 2007, High-fidelity time-stepping for reverse-time migration: CREWES Research Report.
- , 2008, Phase-shift time-stepping for reverse-time migration: the marmousi data experience: CREWES Research Report.
- Whitmore, N. D., 1983, Iterative depth migration by backward time propagation: SEG Technical Program Expanded Abstracts, **2**, 382–385.
- , 1995, An imaging hierarchy for common angle plane-wave seismograms: PhD thesis, he University of Tulsa.
- Whitmore, N. D., and L. R. Lines, 1986, Vertical seismic profiling depth migration of a salt dome flank: *Geophysics*, **51**, 1087–1109.
- Woodward, M., D. Nichols, O. Zdraveva, P. Whitfield, and T. Johns, 2008, A decade of tomography: *GEOPHYSICS*, **73**, VE5–VE11.
- Wu, R.-S., and L.-J. Huang, 1992, Scattered field calculation in heterogeneous media using a phase-screen propagator: SEG Technical Program Expanded Abstracts, **11**, 1289–1292.
- Yan, J., and P. Sava, 2009, 3D elastic wave mode separation for tti media: SEG Technical Program Expanded Abstracts, **28**, 4294–4298.
- Yan, L., L. R. Lines, and D. C. Lawton, 2004, Influence of seismic anisotropy on prestack depth migration: *The Leading Edge*, **23**, 30–36.
- Yilmaz, O., 2001, Seismic data analysis: Processing, inversion, and interpretation of seismic data: SEG.
- Yoon, K., K. J. Marfurt, and W. Starr, 2004, Challenges in reverse-time migration: SEG Technical Program Expanded Abstracts, **23**, 1057–1060.
- Youn, O., and H. Zhou, 2001, Depth imaging with multiples: *GEOPHYSICS*, **66**,

- 246–255.
- Zhang, Y., J. C. Sun, and S. H. Gray, 2003, Aliasing in wavefield extrapolation prestack migration: *Geophysics*, **68**,

# Appendix A

## Mathematics and background theory

### A.1 Fourier theory

The following conventions are used for the forward and inverse Fourier transform of the function  $\varphi : \mathbb{R}^3 \rightarrow \mathbb{C}$ ,

$$\hat{\varphi}(\vec{k}) = \mathcal{F}_{\vec{x} \rightarrow \vec{k}}(\varphi) = \int_{\mathbb{R}^3} e^{2\pi i \vec{x} \cdot \vec{k}} \varphi(\vec{x}) dx dy dz, \quad (\text{A.1})$$

and

$$\varphi(\vec{x}) = \mathcal{F}_{\vec{k} \rightarrow \vec{x}}^{-1}(\hat{\varphi}) = \int_{\mathbb{R}^3} e^{-2\pi i \vec{x} \cdot \vec{k}} \hat{\varphi}(\vec{k}) dk_x dk_y dk_z, \quad (\text{A.2})$$

where  $\mathbb{R}$  is the real line,  $i = \sqrt{-1}$ ,  $\vec{x} = (x, y, z) \in \mathbb{R}^3$ ,  $\vec{k} = (k_x, k_y, k_z) \in \mathbb{R}^3$  is the Fourier domain coordinate conjugate to  $\vec{x}$ , and the hat denotes a Fourier transformed function of the spatial coordinates. The symbols  $\mathcal{F}_{\vec{x} \rightarrow \vec{k}}$ , and  $\mathcal{F}_{\vec{k} \rightarrow \vec{x}}^{-1}$  are used to denote the forward and inverse Fourier transforms as abstract operators, respectively. Later, the symbols  $\mathcal{F}_{\vec{x} \rightarrow \vec{k}}$ , and  $\mathcal{F}_{\vec{k} \rightarrow \vec{x}}^{-1}$  are also used to denote the Fourier-like integrals or as precisely defined in the mathematical literature Fourier integral operator (FIO) when  $\varphi$  or  $\hat{\varphi}$  depend on both  $\vec{k}$  and  $\vec{x}$  explicitly. In this case, a single FFT cannot be used to calculate the Fourier transform.

For the Fourier transform with respect to time the opposite sign convention to the spacial Fourier transform is used,

$$\hat{\varphi}(\omega) = \int_{\mathbb{R}} e^{-2\pi i t \omega} \varphi(t) dt, \quad (\text{A.3})$$

$$\varphi(t) = \int_{\mathbb{R}} e^{2\pi i t \omega} \hat{\varphi}(\omega) d\omega. \quad (\text{A.4})$$

### A.2 The Gabor transform and adaptive partitions of unity

The Fourier transform is used in signal processing of seismic data as a method of filtering and as a part of migration (e.g. Gazdag (1978); Stolt (1978)). However, seismic signals and operators change character over space and time requiring a time-variant and space-variant filtering (Margrave, 1998). For wavefield continuation migrations,

the Fourier transform methods are less efficient when the velocity model is more complex. As an alternative to the Fourier transform or as a generalization of it, the Gabor transform is used to deal with the non-stationary character of seismic signals. It was first proposed by Gabor (1946) as the windowing of a signal with a space shifted Gaussian function, followed by a Fourier transform, and then repeated for many window positions. The Gabor transform is used in seismic imaging to implement non-stationary filters. For example, Margrave et al. (2005) proposed Gabor deconvolution, which corrects the data for anelastic attenuation, while Ma and Margrave (2008), and Grossman et al. (2002) have proposed highly accurate Gabor depth imaging algorithms.

To solve the wave equation in a variable velocity medium, we approximate the velocity function using a partition of unity (POU). A POU is a suite of window functions  $\{\Omega_j(\vec{x}) : \mathbb{R}^2 \rightarrow [0, 1], j \in [1, J]\}$  satisfying

$$1 = \sum_{j=1}^J \Omega_j(\vec{x}), \quad (\text{A.5})$$

where each  $\Omega_j(\vec{x})$  is a discontinuous function bounded between 0 and 1.

Additionally, we impose the condition,

$$\sum_{j=1}^J v_j^2 \Omega_j(\vec{x}) = v^2(\vec{x}), \quad (\text{A.6})$$

which forces the windowing and interpolation to better approximate the cosine operator. The POU can be used to define a Gabor analysis and synthesis window pair. Let  $g_j(\vec{x}) = \Omega_j^p(\vec{x})$  and  $\gamma_j(\vec{x}) = \Omega_j^{1-p}(\vec{x})$  for any  $p \in [0, 1]$ . The functions  $g_j$  are called analysis windows, while the functions  $\gamma_j$  are called synthesis windows. When  $p = 0$  or 1 the analysis windows, or synthesis windows are unity, respectively. The forward Gabor transform is defined by

$$V_g \psi_j(\vec{k}) = \mathcal{F}_{\vec{x} \rightarrow \vec{k}}[g_j(\vec{x}) \psi(\vec{x})]. \quad (\text{A.7})$$

An inverse to the Gabor transform operating on the Gabor spectra  $W(\vec{k}, j)$  is,

$$V_\gamma^{-1} W(\vec{k}, j) = \sum_j \gamma_j(\vec{x}) \mathcal{F}_{\vec{k} \rightarrow \vec{x}}^{-1}[W(\vec{k}, j)], \quad (\text{A.8})$$

as,

$$\begin{aligned}
V_\gamma^{-1} V_g \psi_j(\vec{x}) &= \sum_j \gamma_j(\vec{x}) \mathcal{F}_{\vec{k} \rightarrow \vec{x}}^{-1} [V_g \psi_j(\vec{x})] \\
&= \sum_j \gamma_j(\vec{x}) \mathcal{F}_{\vec{k} \rightarrow \vec{x}}^{-1} \mathcal{F}_{\vec{x} \rightarrow \vec{k}} [g_j(\vec{x}) \psi(\vec{x})] \\
&= \sum_j \gamma_j(\vec{x}) g_j(\vec{x}) \psi(\vec{x}) \\
&= \sum_j \Omega_j(\vec{x}) \psi(\vec{x}) \\
&= \psi(\vec{x}). \tag{A.9}
\end{aligned}$$

In general, the inverse of the Gabor transform is not unique, but the above definition is easy to compute and enjoys good numerical properties. For wavefield propagation the cases  $p = 0, 1$  are usually preferred. This is because the cases  $p \in (0, 1)$  take twice as long to compute as well they don't allow for the energy to shift between windows.

### A.3 Gabor analysis

A Gabor multiplier is the Gabor transform equivalent of a Fourier multiplier or filter. Gabor multipliers allows a different filter to be used for different time windows of the data. The Gabor spectrum is multiplied by a time-frequency or space-wavenumber filter called the Gabor Multiplier. The inverse of the new spectrum is the non-stationary filtered signal. Specifically, a Gabor multiplier, is the triple  $(g, \gamma, M)$  where for a function  $\psi : \mathbb{R}^2 \rightarrow \mathbb{R}$  suitably defined,

$$M_{g,\gamma}\psi = V_\gamma^{-1} M V_g \psi. \tag{A.10}$$

In general, the action of the Gabor multiplier depends on the windowing functions.

### A.4 Thomsen's parameters

The strength of the anisotropic coefficients and how they deviate from the isotropic approximation is hidden in the  $C_{ij}$  variables. In addition, the components of the stiffness tensor for VTI media are cumbersome and difficult to work with. Thomsen (1986) parameters have a physical meaning and are easier to work with. The vertical P-wave velocity is,

$$V_{Po} = \sqrt{\frac{C_{33}}{\rho}}. \tag{A.11}$$

The vertical S-wave velocity is,

$$V_{SO} = \sqrt{\frac{C_{55}}{\rho}}. \quad (\text{A.12})$$

The anisotropy parameters are,

$$\epsilon = \frac{C_{11} - C_{33}}{2C_{33}}, \quad (\text{A.13})$$

$$\delta = \frac{(C_{13} - C_{55})^2 - (C_{33} - C_{55})^2}{2C_{33}(C_{33} - C_{55})}, \quad (\text{A.14})$$

$$\gamma = \frac{C_{66} - C_{55}}{2C_{55}}. \quad (\text{A.15})$$

The dimensionless parameters  $\epsilon$ ,  $\delta$ , and  $\gamma$  are zero for an isotropic media. The parameter  $\epsilon$  represents the fractional difference between Horizontal and vertical P-wave velocity. The parameter  $\delta$  characterizes the small-offset  $P$ -wave reflection moveout in a homogeneous VTI media above a horizontal reflector. The parameter  $\gamma$  determines the small offset S-wave moveout.

## A.5 An evolutionary solution to the acoustic wave equation

Rather than solving a partial differential equation (PDE) directly by a pseudo-spectral method or FD method, Tal-Ezer (1986) suggest first rewriting the PDE as a first order system and then approximated the analytical solution. Transforming the acoustic wave equation into a system of first order linear PDEs gives,

$$\frac{\partial}{\partial t} \begin{bmatrix} U \\ V \end{bmatrix} = \begin{bmatrix} 0 & 1 \\ v^2(x, z) \left( \frac{\partial^2}{\partial x^2} + \frac{\partial^2}{\partial z^2} \right) & 0 \end{bmatrix} \begin{bmatrix} U \\ V \end{bmatrix}, \quad (\text{A.16})$$

subject to the initial condition,

$$\begin{bmatrix} U(0, \vec{x}) \\ V(0, \vec{x}) \end{bmatrix} = \begin{bmatrix} f(\vec{x}) \\ g(\vec{x}) \end{bmatrix}. \quad (\text{A.17})$$

The abstract solution can be written as the exponential of the linear operator,

$$\mathcal{L} = \begin{bmatrix} 0 & 1 \\ v^2(x, z) \left( \frac{\partial^2}{\partial x^2} + \frac{\partial^2}{\partial z^2} \right) & 0 \end{bmatrix}, \quad (\text{A.18})$$

so that,

$$\begin{bmatrix} U(t, \vec{x}) \\ V(t, \vec{x}) \end{bmatrix} = \exp(\mathcal{L}t) \begin{bmatrix} U(0, \vec{x}) \\ V(0, \vec{x}) \end{bmatrix}, \quad (\text{A.19})$$

where the exponential operator is,

$$\exp(\mathcal{L}t) = \sum_{n=0}^{\infty} \frac{t^n \mathcal{L}^n}{n!}. \quad (\text{A.20})$$

Tal-Ezer (1986) approximates the exponential operator by an expansion in terms of modified Chebychev polynomials and Bessel functions.

It is possible to reformulate (Etgen and Dellinger, 1989) equation (A.19) in terms of a cosine of the operator  $\mathcal{L}$ . Then,

$$U(t + \Delta t) = -U(t - \Delta t) + \cos(\mathcal{L}\Delta t)U(t), \quad (\text{A.21})$$

where

$$\cos(\mathcal{L}\Delta t) = \sum_{n=0}^{\infty} (-1)^n \frac{(\Delta t)^{2n} \mathcal{L}^{2n}}{(2n)!}. \quad (\text{A.22})$$

For constant velocity equations (A.21) and (3.33) are the same.

Let  $F(t, \vec{x})$  be the shot field used to start propagation. The system wave equation with an inhomogeneous source function is,

$$\frac{\partial}{\partial t} \begin{bmatrix} U \\ V \end{bmatrix} = \mathcal{L} \begin{bmatrix} U \\ V \end{bmatrix} + \begin{bmatrix} F \\ \frac{\partial F}{\partial t} \end{bmatrix}. \quad (\text{A.23})$$

The solution in terms of the exponential of the evolutionary operator  $\exp(\delta t \mathcal{L})$  for a time step  $\delta t$  is,

$$\begin{bmatrix} U(\delta t + t, \vec{x}) \\ V(\delta t + t, \vec{x}) \end{bmatrix} = \exp(\mathcal{L}\delta t) \begin{bmatrix} U(t, \vec{x}) \\ V(t, \vec{x}) \end{bmatrix} + \int_0^{\delta t} \exp(\mathcal{L}(\delta t - \tau)) \begin{bmatrix} F(\tau + t, x) \\ G(t + \tau, x) \end{bmatrix} d\tau. \quad (\text{A.24})$$

The inhomogeneous forcing functions  $F$  and  $G = \partial F / \partial t$  are sampled at  $\delta t$ , equation (A.24) is approximated by,

$$\begin{bmatrix} U(\delta t + t, \vec{x}) \\ V(\delta t + t, \vec{x}) \end{bmatrix} = \exp(\mathcal{L}\delta t) \begin{bmatrix} U(t, \vec{x}) \\ V(t, \vec{x}) \end{bmatrix} + \begin{bmatrix} F(t, x) \\ G(t, x) \end{bmatrix}. \quad (\text{A.25})$$

For constant velocity, in the spatial Fourier domain the exponential of the operator is defined by equation (3.51). By adding  $U(-\delta t, \vec{k})$  to  $U(\delta t, \vec{k})$ , the inhomogeneous cosine stepper is,

$$\hat{U}(t + \delta t, \vec{k}) = 2 \cos(2\pi\omega\delta t) \hat{U}(t, \vec{k}) - \hat{U}(t - \delta t, \vec{k}) + 2\hat{F}(t, \vec{k}). \quad (\text{A.26})$$